AMMONIA-WATER DESORPTION IN FLOODED COLUMNS

A Thesis
Presented to
The Academic Faculty

By

James Hollis Golden

In Partial Fulfillment
Of the Requirements for the Degree
Master of Science in Mechanical Engineering

Georgia Institute of Technology

August, 2012

AMMONIA-WATER DESORPTION IN FLOODED COLUMNS

Approved by:

Dr. Srinivas Garimella, Advisor
G. W. Woodruff School of Mechanical Engineering
Georgia Institute of Technology

Dr. S. Mostafa Ghiaasiaan
G. W. Woodruff School of Mechanical Engineering
Georgia Institute of Technology

Dr. Sheldon M. Jeter
G. W. Woodruff School of Mechanical Engineering
Georgia Institute of Technology

Date Approved:
28 June 2012

ACKNOWLEDGEMENTS

I would like to thank all of the members of the Sustainable Thermal Systems Laboratory at the Georgia Institute of Technology, particularly Chris Keinath, Jared Delahanty and Matthew Determan, for their thoughtful advice, sound guidance and willingness to help. I would especially like to thank my advisor, Dr. Garimella for providing this research opportunity and for his guidance through this work. I would also like to thank my parents, and my brother, Daniel Golden, for their continued support and encouragement.

TABLE OF CONTENTS

LIST OF TABLES

LIST OF FIGURES

NOMENCLATURE

Symbols

A	Area (m^2)
A_o	Specified Correlation Constant
B_o	Specified Correlation Constant
C	Specified Correlation Constant
C	Molar Concentration
COP	Coefficient of Performance
Cp	Specific Heat (kJ $kg^{-1}K^{-1}$)
C_d	Drag Coefficient
D	Diameter (mm)
D	Mass Diffusivity (m^2 s^{-1})
D_h	Hydraulic Diameter (mm)
F_D	Correction Factor
g	Gravitational Acceleration Constant (m s^{-2})
h	Heat Transfer Coefficient (W $m^{-2}K^{-1}$)
h	Enthalpy (kJ kg^{-1})
k	Thermal Conductivity (W $m^{-1}K^{-1}$)
L	Length (m)
LMTD	Log Meat Temperature Difference (°C, K)
M	Molar Mass (kg mol^{-1})
$\dot{m}$	Mass Flow Rate (kg s^{-1})

N	Number of Segments, Cycles, Columns, or Channels
n	Number of Temperature Levels
$\dot{n}$	Mass Flux (kg $s^{-1}m^{-2}$)
P	Pressure (kPa)
P_r	Reduced Pressure
q	Quality
q	Heat Rate (kW)
q"	Heat Flux (kW m^{-2})
r	Radius (m)
R	Thermal Resistance (K W^{-1})
R	Ideal Gas Constant (kJ mol^{-1} K^{-1})
R	Characteristic Length (m)
R^2	Coefficient of Determination
Re	Reynolds Number
SEER	Seasonal Energy Efficiency Ratio
Sh	Sherwood Number
T	Temperature (°C, K)
t	Thickness (mm)
U	Velocity (m s^{-1})
UA	Conductance (w K^{-1})
x	Mass Concentration
$\tilde{x}$	Molar Concentration
y	Vapor Mass Concentration

$\tilde{z}$	Condensate Concentration

Greek Letters

α	Heat Transfer Coefficient (W $m^{-2}K^{-1}$)
β	Mass Transfer Coefficient (m s^{-1})
δ	Thickness (mm)
Δ	Temperature Difference (°C, K)
η	Efficiency
μ	Viscosity (Pa s)
ρ	Density (kg m^{-3})
σ	Surface Tension (N m^{-1})
σ	Collision Diameter (Å)
Ω	Collision Integral

Subscripts

a	Ammonia
ATM	Atmospheric
Ave	Average
CF	Coupling Fluid
Cond	Condensation
Cr	Critical
F	Fin
FF	Falling Film
FG	Fluid - to - Gas, Vaporization

Id	Ideal
L	Liquid
In	Inlet
NH_3 - H_2O	Ammonia - Water
Out	Outlet
O	Reference
Sat	Saturation
T	Total Array
V	Vapor
V - S	Vapor - to - Solution
w	Water

SUMMARY

Refrigeration systems employing the NH_3-H_2O absorption cycle provide cooling using a thermal energy input. This cycle relies on the zeotropic nature of the refrigerant – absorbent pair: because of the difference in boiling temperatures between NH_3 and H_2O, they can be separated through selective boiling in the desorber. Desorbers with counter-current flow of the solution and generated vapor enable efficient heat and mass transfer between the two phases, reducing the absorbent content in the generated vapor.

Flow visualization experiments at temperatures, concentrations and pressures representative of operating conditions are necessary to understand the heat and mass transfer processes and flow regime characteristics within the component. In this study, a Flooded Column desorber, which accomplishes desorption of the refrigerant vapor through a combination of falling-film and pool boiling, was fabricated and tested. Refrigerant-rich solution enters the top of the component and fills a column, which is heated by an adjacent heated microchannel array. The vapor generated within the component is removed from the top of the component, while the dilute solution drains from the bottom.

Flow visualization experiments showed that the Flooded Column desorber operated most stably in a partially flooded condition, with a pool-boiling region below a falling-film region. It was found that the liquid column level was dependent on operating conditions, and that the pool-boiling region exhibits aggressive mixing between the vapor and solution phases.

Heat transfer coefficients were calculated from the data for the pool-boiling region, and were compared with the predictions of several mixture pool-boiling correlations from the literature. The correlations from the literature were in general unable to predict the data from this

study adequately. It was found that the Flooded Column desorber yielded higher heat transfer coefficients within the pool-boiling region than those predicted by these correlations. Therefore, modifications to existing mixture boiling correlations are suggested based on the findings of this study. The resulting modified correlation predicts 33 of the 35 data points from this study within ±40%, with an average absolute error of 19%.

CHAPTER 1: INTRODUCTION

This chapter provides the background and rationale for research on thermally activated cooling systems based on the increasing electrical demands of space-conditioning systems. The basic absorption system is introduced and compared to the ubiquitous vapor–compression cycle. Advances in absorption system implementation are considered, and the scope of the present work is defined.

1.1 Motivation

Conventional space-conditioning systems demand a large fraction of the national power supply. The U.S. Energy Information Administration (EIA) reports that 13% of the electricity generated in the United States is used for refrigeration and air conditioning across all sectors (Rattner and Garimella, 2011). The EIA also reports that 16% of the electricity consumed by the average U.S. household in 2001 was for air conditioning. Moreover, for consumers in living warmer states such as Georgia, more than 30% of the power bill is to pay for air-conditioning (U.S. Energy Information Administration, 2001, 2005).

The electrical demand of space-conditioning systems is quite significant, and has been dramatically increasing throughout the last decade. Figure 1.1 presents the total electrical demand of residential air conditioning between 1978 and 2005 (U.S. Energy Information Administration, 2000, 2001, 2005). Across the nation, the total electrical consumption by residential air conditioning systems doubled between 1987 and 2005.

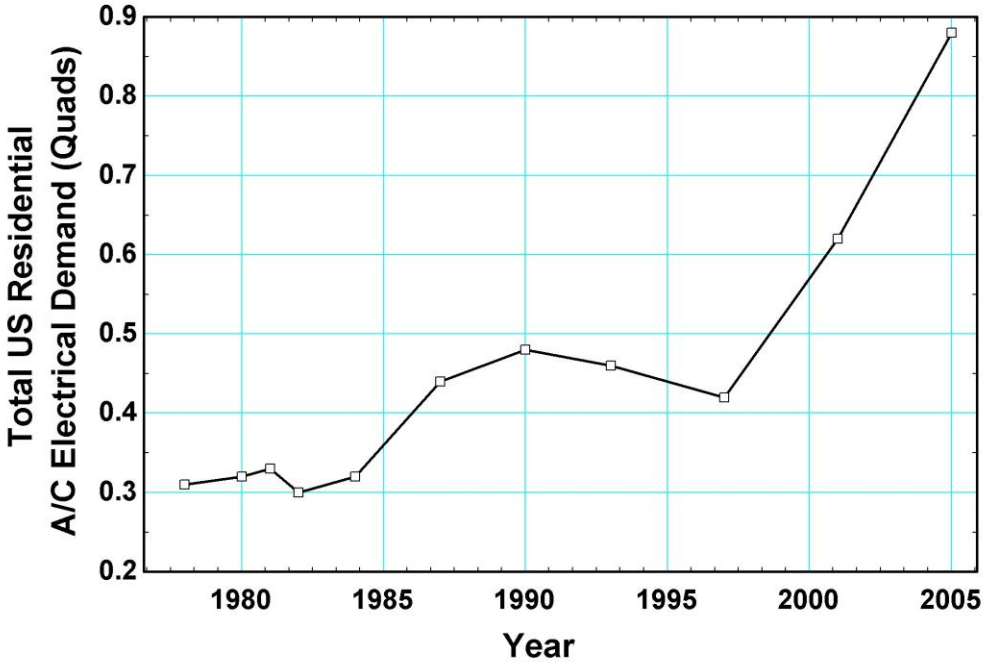

Figure 1.1: Nationwide Residential A/C Electrical Consumption, 1978 - 2005 (U.S. Energy Information Administration, 2000, 2001, 2005)

Increased electrical demand stems, in part, from dramatic changes in both the number of air-conditioning systems nationwide, and their frequency of operation. The EIA reports that the number of households with central air-conditioning systems has nearly tripled from 17.6 million to 47.8 million between 1978 and 2005. Moreover, the percentage of households that report using their A/C "all summer long" has doubled from 1981 to 2005, from 33% to 61% (U.S. Energy Information Administration, 2000, 2005). Not only has residential air conditioning become ubiquitous, but also the operation of many systems that facilitate the modern way of life, such as electronic control systems and data centers, rely on space conditioning. In a time with increased focus on energy consumption and efficiency, the electrical demand of air-conditioning systems is significant, and the steep upward trend of consumption is not likely to slow.

While the level of consumption has increased significantly over the past three decades, technological refinements have moderated the growth in demand. New homes are constructed with better insulation and windows to reduce the load on the space-conditioning system. More significantly, the efficiency of air-conditioning systems has dramatically increased over the last three decades. One measure of efficiency is the Seasonal Energy Efficiency Ratio (SEER), which is defined as the seasonal average of the ratio of the cooling output in BTU and the total electric energy input in Watt-hours. Figure 1.2 presents a plot of the average SEER of central air conditioning units sold between 1978 and 1997 (U.S. Energy Information Administration, 2000).

As of 2006, all newly installed air-conditioning systems are required by law to exceed 13 SEER, nearly double the efficiency of the average unit installed in 1978 (U.S. Energy Information Administration, 2002).

Even with higher efficiency vapor compression systems, any system requiring electrical

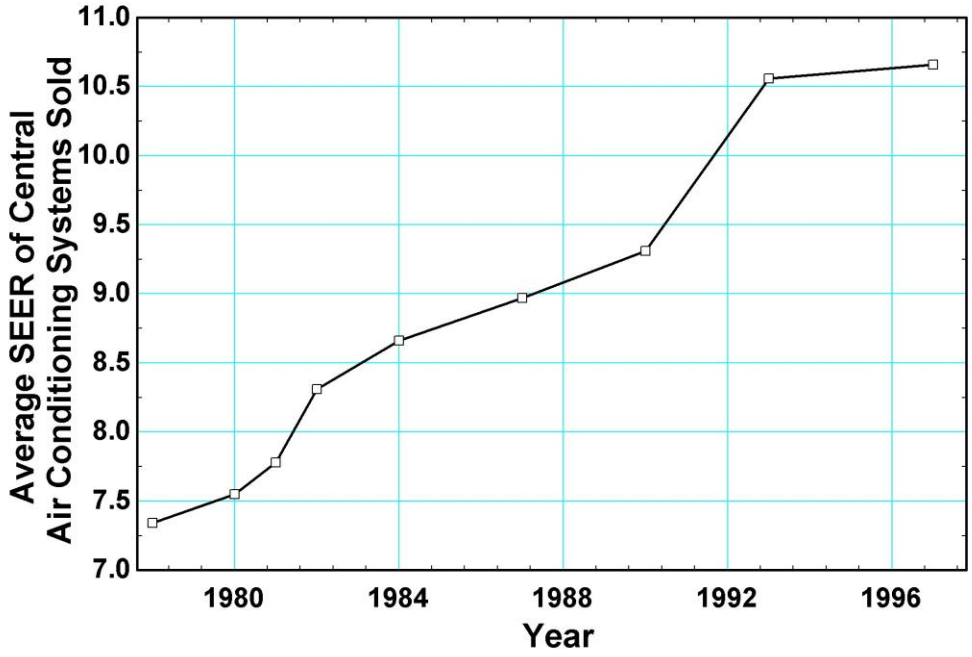

Figure 1.2: Average SEER of Installed Central Air-Conditioning Units, 1978 - 1997 (U.S. Energy Information Administration, 2000)

power will propagate the inefficiencies inherent to that energy path. Fossil fuel and nuclear–powered electrical generation plants operate by converting a thermal energy stream into electricity, which must be transmitted from this plant to the end use location. The EIA estimates that across the US in 2009, 38.89 Quads of thermal energy were used in all electrical plants to generate and transmit 14.28 Quads of electrical power, a conversion efficiency of 37% (U.S. Energy Information Administration, 2010). The direct use of thermal energy to drive the space-conditioning system does not incur this entire conversion penalty, and offers versatility in source and end-use options.

As the demand for air conditioning and the cost of electricity continue to increase, and the energy efficiency of standard vapor-compression cycles plateaus, and considering the inefficiency inherent in the production and transmission of electricity, cooling systems that are not driven by electrical input, such as those employing the absorption cycle, should be considered as one of the possible options for space-conditioning.

1.2 Vapor-Compression Cycle

Conventional space-conditioning systems typically employ the vapor-compression cycle to provide cooling and heating. The cycle, illustrated schematically in Figure 1.3, uses a refrigerant to remove heat from a low temperature source and reject it to a high temperature sink, and is primarily driven by an electrical input.

A mostly liquid refrigerant at low pressures, at Statepoint 1 in Figure 1.3, receives heat from the heat source as it changes phases in the evaporator. Past the evaporator at Statepoint 2, an electrically-powered compressor raises the pressure of the refrigerant vapor, thereby increasing its saturation temperature to Statepoint 3. The high pressure refrigerant vapor is now

at a higher temperature than the heat sink; the refrigerant condenses as it rejects heat to the sink in the condenser. Past the condenser at Statepoint 4, the refrigerant flows through an expansion device, returning the refrigerant to the low pressure of the evaporator at Statepoint 1.

The vapor-compression cycle is ubiquitous and well understood, but it relies on an electricity intensive compressor to accomplish the cooling effect. Additionally, vapor-compression applications typically employ synthetic refrigerants with Global Warming Potential.

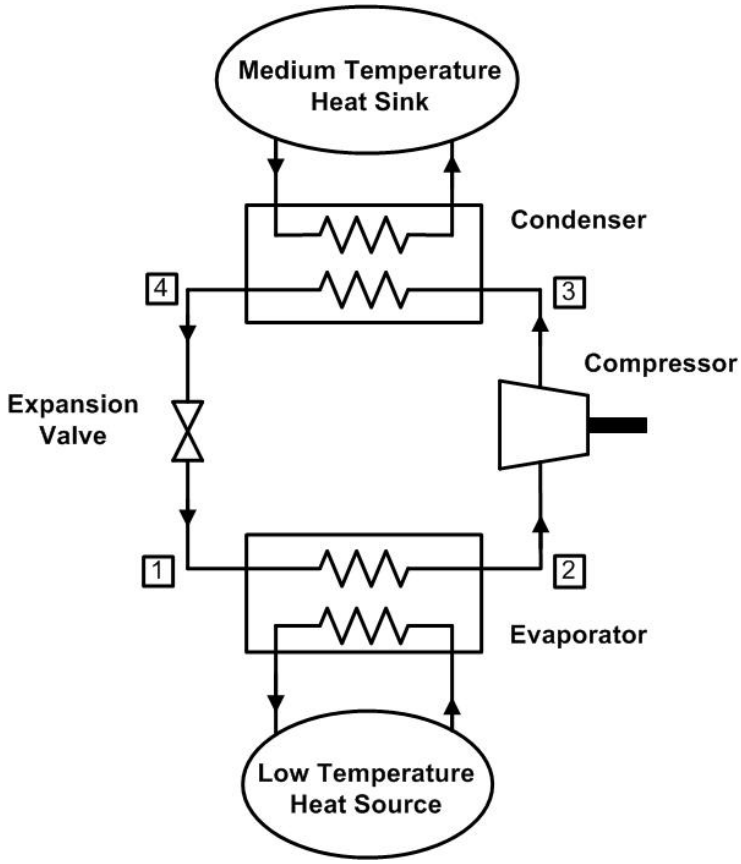

Figure 1.3: Vapor-Compression Cycle

1.3 Absorption Cycle

Unlike the vapor-compression cycle, the absorption cycle can be employed to produce cooling directly from a heat stream. Figure 1.4 presents a schematic of a basic absorption cycle.

As in the vapor-compression cycle, an evaporator and condenser are used to transfer heat into and away from the cycle, respectively. These two heat exchangers, which operate at different pressures, are again separated by an expansion device. Unlike the vapor-compression cycle, the absorption cycle uses a number of components, collectively called a thermal compressor, to raise the pressure of the refrigerant, instead of a mechanical compressor. From Statepoint 1 in Figure 1.4, low pressure refrigerant vapor from the evaporator enters the first component of this thermal compressor, the absorber. In this component, the refrigerant vapor is absorbed into solution with an absorbent from Statepoint 10, generating the concentrated solution at Statepoint 2. The absorption process is exothermic and the absorber is cooled by thermal coupling to a heat sink. From Statepoint 2 at the absorber, the concentrated solution is pumped to the high-side condenser pressure at Statepoint 3 before flowing through the

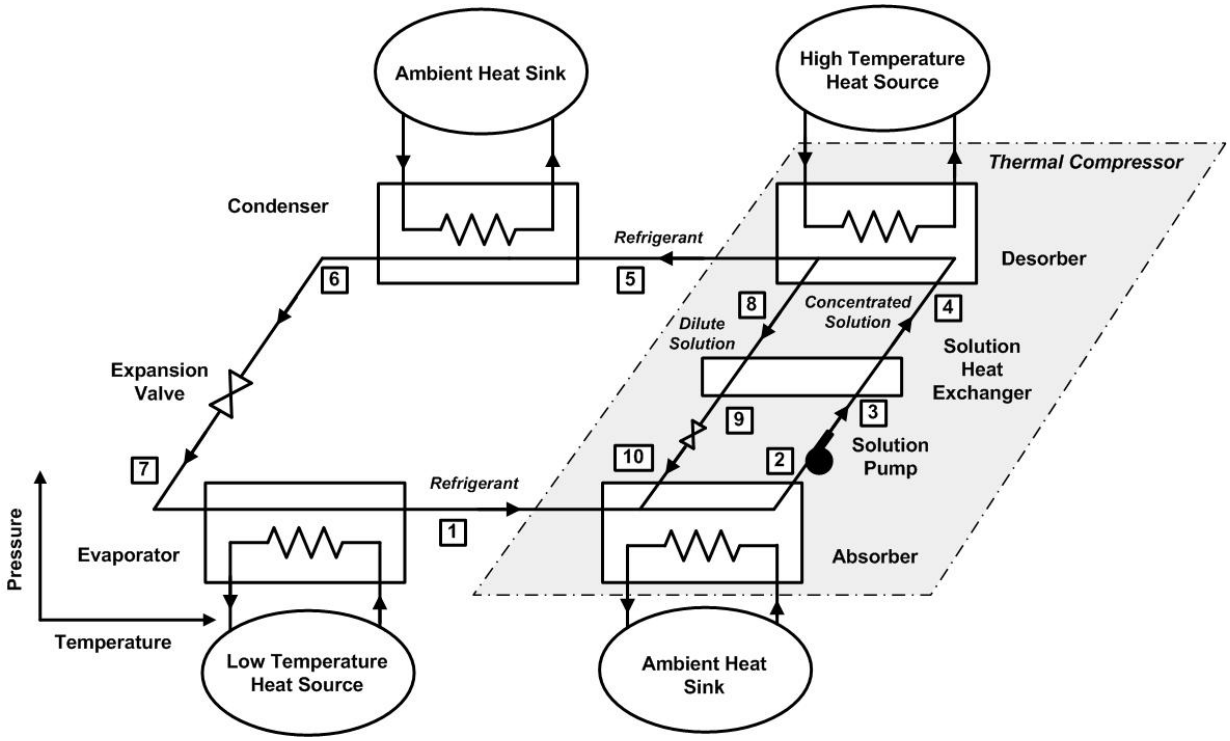

Figure 1.4: Basic Absorption Cycle

recuperative solution heat exchanger. The high pressure concentrated solution at Statepoint 4 enters the desorber, where heat input is supplied, selectively boiling the refrigerant out of the solution. A high purity refrigerant vapor stream, Statepoint 5 and a dilute solution stream, Statepoint 8, leave the desorber. The refrigerant vapor at Statepoint 5 flows through the condenser to Statepoint 6, while the dilute solution flows through the solution heat exchanger and an expansion device to Statepoint 10 before entering the absorber. Because the dilute solution exiting the desorber at Statepoint 8 is much hotter than the concentrated solution entering it at Statepoint 3, a recuperative solution heat exchanger is included in the basic cycle between the absorber and desorber.

The primary energy input into the absorption cycle is the high temperature source stream in the desorber. An electric pump is used to pressurize the concentrated solution from the absorber, but the work required to pressurize the liquid solution is insignificant compared to the energy required to raise the pressure of the refrigerant vapor in a vapor-compression cycle. The cycle is extremely versatile because a wide variety of heat sources, such as solar thermal energy or waste heat can be used to drive the process. Alternatively, an absorption system could be powered by directly burning natural gas or another fuel. An absorption system is well suited to a residential application; if properly configured, while the heat removed from the environment at the evaporator provides the desired cooling, the heat rejected by the system at the absorber and condenser can provide space heating in the winter, and can also be configured to provide another necessary residential energy need, water heating. Finally, the absorption cycle is advantageous because it typically employs natural refrigerants with no global warming potential. The most commonly used refrigerant-absorbent pairs are ammonia-water and water-lithium bromide.

Absorption cycles have been investigated and implemented for the past 150 years, with increasingly complex systems being developed to achieve higher coefficients of performance. For example, cascaded, multiple–effect cycles have been investigated to increase efficiency; however, these refinements are accompanied by increased system complexity and first cost. Absorption systems are currently limited to low-efficiency niche applications such as hotel room units and recreational vehicle refrigeration, and very large lithium bromide-water chillers at airports, hospitals and other large campuses (Adcock, 1995). The development of a marketable residential-scale absorption system requires the development of compact, highly efficient heat and mass transfer devices.

1.4 Miniaturized Thermally Activated Cooling Systems

Microscale monolithic absorption systems have recently been reported by Determan and Garimella (2012.) These heat pumps consist of highly efficient and compact microchannel heat exchangers, all packaged into monolithic units that comprise the entire thermally activated cooling system. These monolithic heat pumps consist of a bonded array of alternating shims with etched microchannel features. When stacked and bonded, these shims form fluid passages with hydraulic diameters on the order of 300 μm. Because the convective heat transfer coefficient in laminar flow is inversely proportional to hydraulic diameter, these small fluid passages promote extremely high rates of heat and mass transfer. Additionally, these microchannel components can be configured in counterflow orientation, further increasing the heat transfer performance for a given surface area. Moreover, the low pressure drop in parallel flow through the microchannel arrays ensures minimal required pumping power, while the small volume of the components requires minimal fluid inventory (Nagavarapu and Garimella, 2011).

Figure 1.5, from (Nagavarapu and Garimella, 2011) shows a shim assembly representative of this heat exchanger design. Microchannel heat exchangers can be fabricated for most of the components in an absorption system. Clockwise from the top, Figure 1.6 shows the shim designs for the condenser, refrigerant heat exchanger, evaporator, absorber, solution heat exchanger and desorber of a prototype miniaturized absorption system.

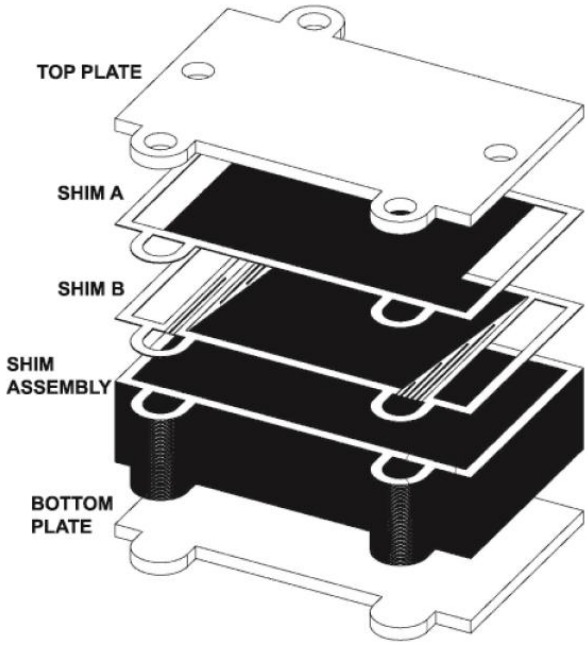

Figure 1.5: Etched-Shim Microchannel Heat and Mass Exchanger (Nagavarapu and Garimella, 2011)

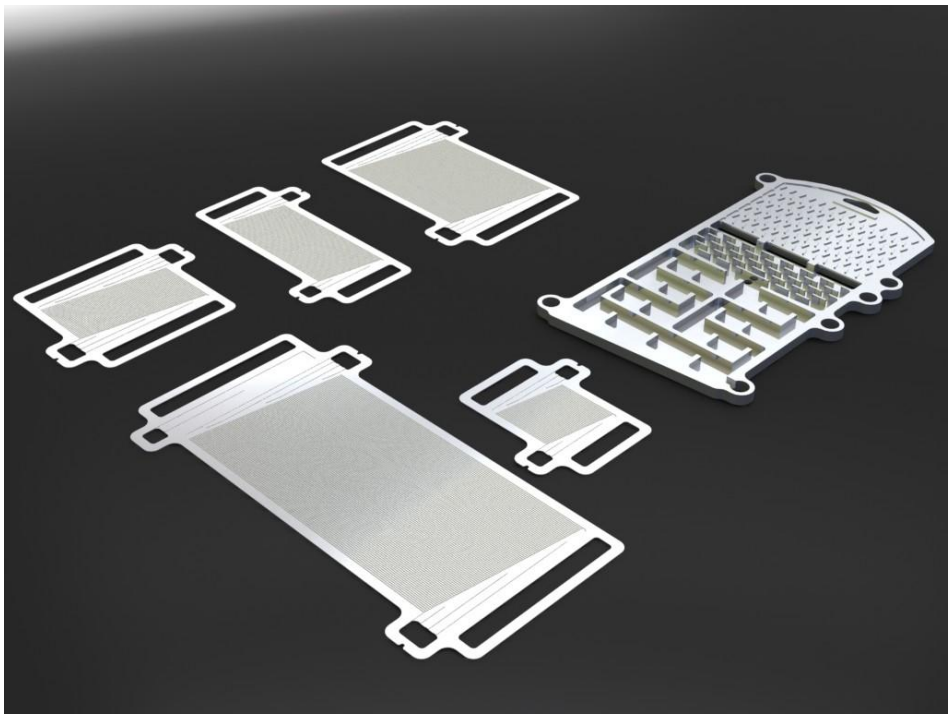

Figure 1.6: Representative Schematic of Etched-Shim Heat Exchangers for an Absorption System (Image Courtesy of Jared Delahanty)

1.5 Desorber Design and Operation

While many of the components of a miniaturized absorption system can be readily designed and fabricated using this etched-shim technology, the absorber and desorber present specific challenges. These components are central to the operation of the absorption cycle, and require simultaneous heat and mass transfer in a binary zeotropic mixture. Previous investigations have focused on the absorption process and the design and evaluation of absorbers (Meacham and Garimella, 2004); the present work is focused on a component-level study of the desorber. Figure 1.7 presents a conceptual schematic of a desorber, analyzer and rectifier, the set of components that produce nearly pure refrigerant from the refrigerant-absorbent solution.

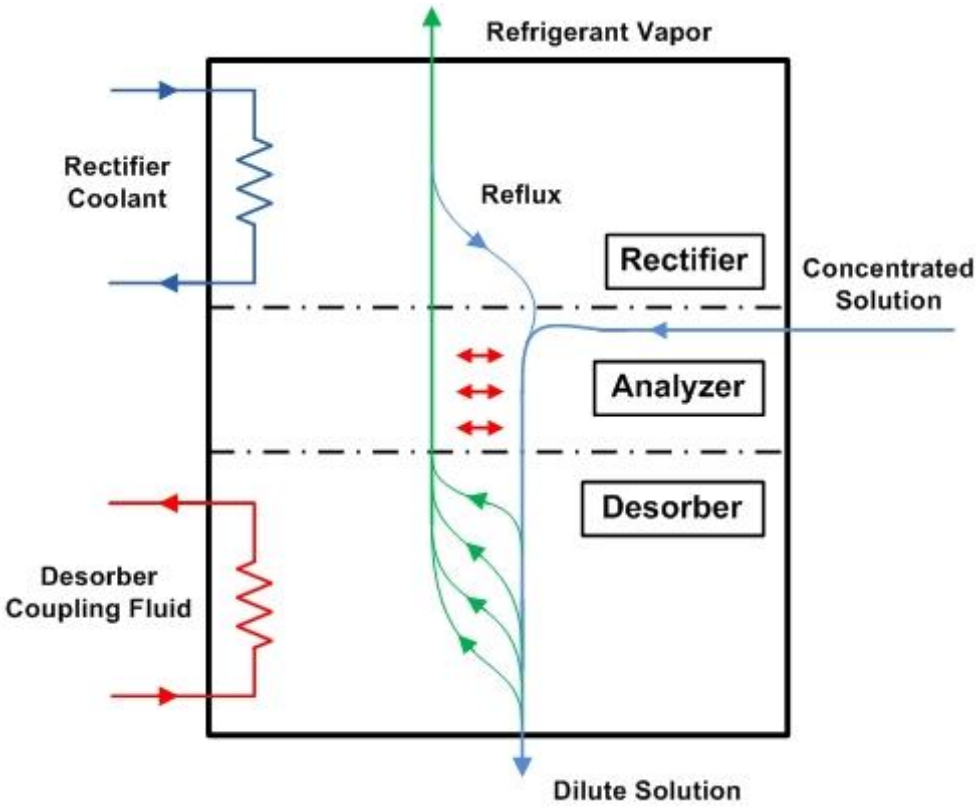

Figure 1.7: Desorber-Analyzer-Rectifier Schematic

The absorption cycle relies on the zeotropic nature of the refrigerant-absorbent pair. Because the refrigerant has a lower saturation temperature than the absorbent, it preferentially boils out of the solution when heat is applied in the desorber. While the difference in saturation temperature is critical to the operation of the thermal compressor, it also could lead to performance degradation in the condenser and evaporator if not managed correctly. Any volatile absorbent evaporated with the refrigerant in the desorber will cause a temperature glide in the evaporator, increasing the temperature at which cooling can be achieved, thereby adversely affecting performance. To minimize temperature glide, the absorbent content of the refrigerant stream leaving the desorber must be minimized. In most designs, the vapor stream from the desorber is cooled in a rectifier, preferentially condensing the absorbent and purifying the refrigerant vapor. To allow the vapor and solution to exchange species, an adiabatic section

known as an analyzer is often included between the desorber and rectifier sections. These components are illustrated schematically in Figure 1.7.

For simplicity in design and operation, the desorber used in the monolithic system developed by Determan and Garimella (2012) employed a co-current configuration for solution and generated vapor flow. While the co-flow design is easy to implement, its desorption performance is less efficient than a counter-flow design where the vapor and solution streams flow in opposite directions. This is because in a co-current configuration, the generated vapor exits at a high temperature in equilibrium with the exiting dilute solution, and therefore with a large water fraction. The high exit temperature implies that a large fraction of the input heat load was used inefficiently to heat a vapor stream that must be subsequently cooled in the downstream component. It also implies that the exiting vapor, upon purification in the rectifier, will yield a much smaller flow rate of higher purity refrigerant.

While the counter-flow orientation offers superior desorption, its operation is limited by a fluid transport phenomenon known as the counter current flow limitation, or flooding. Consider a vapor rising next to a downward flowing liquid stream in a closed channel. If the vapor velocity is high enough, a portion of the liquid flow will be entrained with the rising vapor. If the vapor flow rate is beyond a certain threshold, no liquid will be able to flow down the channel, resulting in flooding and even flow reversal. Flooding is dependent on the vapor and liquid flow rates and fluid properties, and the channel hydraulic diameter. Care must be taken when designing counter-flow heat and mass exchangers to prevent the onset of flooding.

1.6 Counterflow Desorber Design Concepts

Flooding prevention is one of several considerations for successful desorber design. Five other principal design metrics were formulated, including the heat transfer area per unit volume,

manufacturing risk and expense, design and modeling uncertainty, and any potential system-level implications of the desorber design. Several conceptual counterflow desorber designs were formulated, both by considering the miniaturization of systems typically used in the distillation industry and by adapting other previously developed miniaturized desorber designs. When evaluated and ranked based on these design criteria, three designs stood out for further investigation.

The Vertical Column design, shown in Figure 1.8, employs falling-film heat transfer. The concentrated solution enters at the top of the desorber, near the center of the component, which includes both desorption and rectification sections. Coupling fluid microchannels in adjacent shims heat the desorber section, generating vapor that flows counter to the falling solution film.

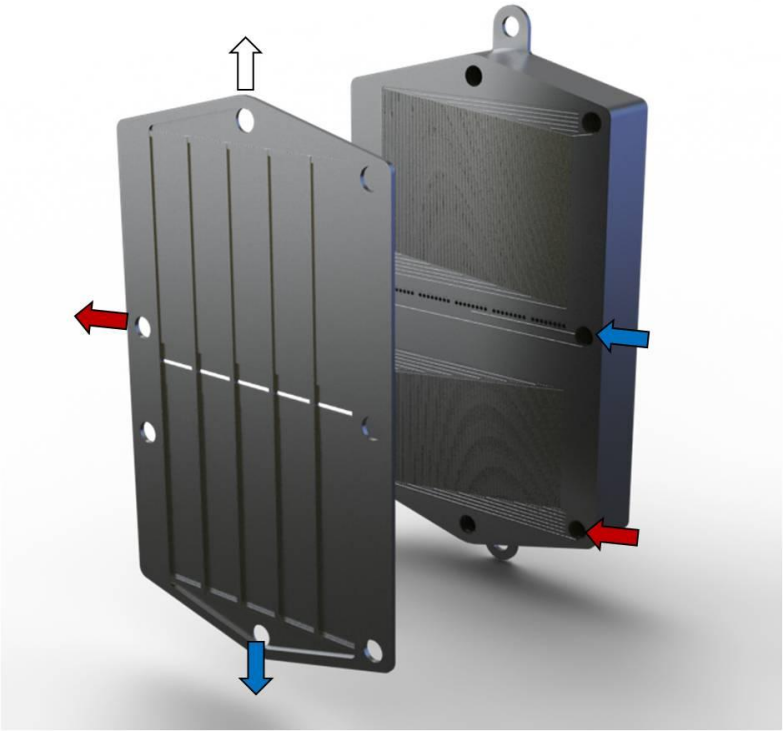

Figure 1.8: Vertical Column Desorber–Rectifier (Image Courtesy of Jared Delahanty)

In the rectifier section, additional coupling fluid channels are used to cool the rising vapor, decreasing its absorbent content. This design carries moderate manufacturing and flooding risk.

The Staggered Tray desorber design, shown in Figure 1.9, employs both the falling-film and pool-boiling heat transfer modes. Concentrated solution enters the top of the desorber and fills numerous trays across the width of the component. As the uppermost trays flood, solution falls down the walls to trays below. Again, coupling fluid channels in adjacent shims heat the desorber, producing vapor that flows upward, counter to the falling solution. Flooding potential is minimized by judiciously spacing each layer of trays, increasing the hydraulic diameter of the vapor passages. The design is marked by limited manufacturing risk and modeling uncertainty, and moderate heat transfer area per unit volume.

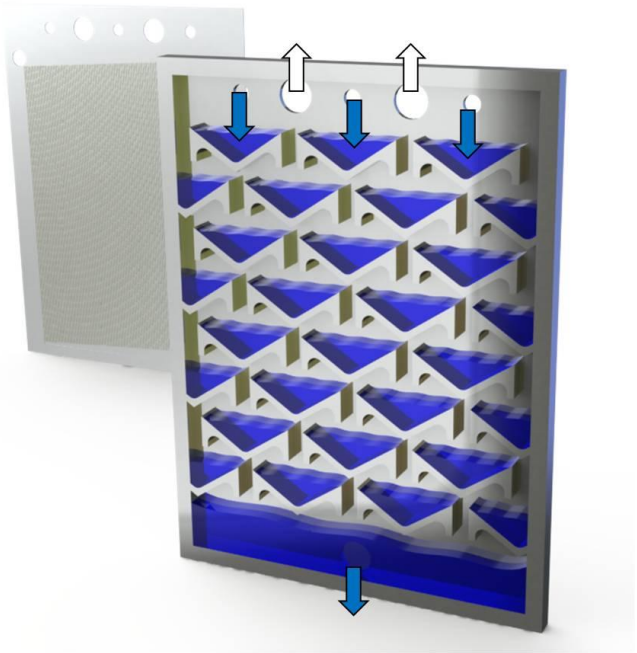

Figure 1.9: Staggered Tray Desorber (Image Courtesy of Jared Delahanty)

The Flooded Column desorber, presented in Figure 1.10, is the final design considered. Concentrated solution enters the top of the component, filling the column nearly completely. Again, coupling fluid channels in shims at the front and back of the column heat the component. The Flooded Column desorber primarily employs pool boiling, and provides a large area for heat transfer between the rising vapor and falling solution. This interaction between the vapor and solution allows the vapor stream to cool as it rises, increasing its purity. Because the desorber is intended to operate in a fully flooded condition, the liability of counter-current flow limitation is removed. This design has minimal risks in design, modeling and fabrication.

Figure 1.10: Flooded Column Desorber (Image Courtesy of Jared Delahanty)

Each of the desorber designs was evaluated based on the six design metrics; for each metric, each design was ranked as positive, negative or neutral. This comparative analysis is documented in Table 1.1. Based on this analysis, the Flooded Column desorber was identified as the most promising design for this preliminary investigation, and was selected for modeling and prototype development.

Table 1.1: Desorber Design Concept Evaluation Matrix

Concept	Area/ Volume	Flooding Performance	Manufacturing Risk	Design/Modeling Uncertainty	Packaging Efficiency	Cycle Implications	Total
Flooded Column	+	+	+	+	+	+	6
Staggered Tray		+	+	+	+		4
Vertical Column	+			+	+		3

1.7 Scope of the Research and Thesis Outline

The objective of the present study is the design, simulation and experimental validation of a counterflow desorber for a miniaturized thermally-activated ammonia-water heat pump.

The performance of this component is simulated by considering the corresponding heat and mass transfer processes, using a simulation model developed in the *Engineering Equation Solver* software (Klein, 2011) platform. Based on this computational model, a prototype Flooded Column desorber is designed and fabricated for experimental investigation. Flow visualization and heat transfer experiments were conducted to validate the computational model, and to determine the viability of this desorber design.

The remainder of the Thesis is outlined as follows:

Chapter 2 provides a review of the literature pertaining to ammonia–water absorption cycle developments, in particular, those related to desorber design.

Chapter 3 documents the Heat and Mass Transfer model developed to characterize the Flooded Column desorber.

Chapter 4 describes the experimental apparatus and procedures used in the flow visualization and heat transfer investigations.

Chapter 5 provides a discussion of the results from the flow visualization and heat transfer experiments.

Chapter 6 summarizes the performance of the Flooded Column desorber design and offers recommendations for further refinements and investigations.

CHAPTER 2: LITERATURE REVIEW

2.1 Absorption Systems: Overview

Absorption systems were some of the first refrigeration systems developed, and stemmed from the earliest investigations of artificial cooling. The first demonstration of artificial cooling was published by Cullen (1756). In his experiment, a pump was used to lower the pressure of a bell-jar containing samples of diethyl ether and water. The ether boiled at this reduced pressure, taking on heat from the surroundings and freezing the water sample (Cullen, 1756). Cullen's experiments were extended by Nairne (Stephan, 1982). In Nairne's experiment, a bell-jar containing sulfuric acid and water was partially evacuated, causing the water to change phase. Nairne observed that, at the reduced pressure, the sulfuric acid absorbed the evaporating water vapor, hastening the evaporation process and the subsequent temperature drop (Shachtman, 1999). Although other investigators of the early 19th century extended Nairne's sulfuric acid–water absorption experiments, their devices were only used in the laboratory setting and did not progress beyond the experimental stage (Hempstead and Worthington, 2004).

Edmund Carre extended artificial refrigeration experiments beyond the laboratory, developing an operational sulfuric acid–water absorption machine (Granryd and Palm, 2005). While his refrigeration system was installed in many Parisian establishments for ice production, it was plagued by malfunctions and corrosion. Ferdinand Carre refined the design, replacing the sulfuric acid–water working pair with ammonia-water with great success; he patented the first successful absorption refrigeration machine (Adcock, 1995). Carre's system was popular throughout Europe and America in the late 19th century, where large scale systems were

installed in commercial settings. As residential demand grew, refrigeration systems were brought into households. Gas-fired absorption refrigeration units were displaced by electrically-driven vapor-compression systems by the 1950s. Vapor-compression systems are ubiquitous today due to their higher efficiency and lower complexity than that of absorption systems.

Absorption refrigeration systems continue to be used in several niche markets that have exploited advantages of their design. As thermally driven refrigeration systems, absorption systems are able to capitalize on the waste heat of other thermal processes; most new absorption systems are installed at large industrial or commercial campuses where waste heat is available. Because they do not rely on the loud compressors required in vapor-compression systems, absorption systems are often employed in applications where quite operation is important, such as recreational vehicles and hotel room air conditioning units (Adcock, 1995). While absorption systems have recently been viable in only niche markets, they are well suited to expand into the mainstream; as electricity cost and environmental concerns become increasingly important, absorption systems offer an energy efficient solution employing environmentally benign refrigerants. Research and refinements in system design will spur widespread adoption of absorption systems.

2.2 Multiple – Effect Cycles

Refinements to large-scale industrial absorption chillers have typically embraced increased cycle complexity to enhance system efficiency; engineers have developed multiple-effect cycles with significantly higher system COPs than the most basic cycle (Burgett *et al.*, 1999). In these advanced cycles, several absorption cycles are essentially coupled together, increasing the overall system efficiency through recuperative heat exchange; the heat rejected from the condenser and absorber of the hottest cycle is used to heat the desorber of a lower temperature system. Multiple-effect systems have the potential to extract several units of cooling from every one of heat input, but at the cost of system complexity and increased initial expense. Double-Effect cycles currently dominate the commercial scale absorption chiller market. Carrier, Trane and York all manufacture large double-effect absorption chillers – rated up to 5 MW cooling capacity. These systems achieve COPs approaching 1.2 for steam heated systems and 1.0 for gas- or oil-fired operation, compared to 0.6 – 0.7 for a commercial single-effect system (Adcock, 1995).

Double-effect systems have been successfully commercialized, but researchers have been investigating even more complicated systems for decades. Arh and Gaspersic (1989) and Ziegler *et al.* (1993) developed two procedures to estimate the performance of advanced, multi-effect absorption systems based on the superposition of simpler, fundamental cycles. Grossman and Zaltash (2001) describes a modular absorption cycle simulation tool, ABSIM, which has been used by various researchers to model advanced absorption cycles. Garimella *et al.* (1996) and Garimella *et al.* (1997) report the simulation of various generator-absorber heat exchange (GAX) and triple-effect cycles using ABSIM.

Arh and Gaspersic (1989) reported that the number of possible absorption cycle configurations follows the equation, $N = 2^n - 2n$, where N is the number of cycles, and n is the number of temperature levels. Two concepts are clear from this relationship: three distinct temperature levels are required for a single-effect cycle, and a very large number of cycles can be formulated with several distinct temperature levels. All of the potential multiple-effect cycles could be evaluated through time-intensive detailed simulation, but they propose a first-order COP approximation to quickly determine the best potential configurations. In their method, the heat loads of the various components in elementary cycles are determined through simple simulation using the specified fluid pair, at specified temperature levels. Elementary cycles are combined to assemble an advanced cycle and the COP of the multi-effect cycle is determined through the principle of superposition. In this manner, dozens of potential advanced absorption cycles can be quickly analyzed to determine the configuration with the highest COP.

Also addressing the need to quickly develop first-order approximations for the performance of advanced absorption cycles, Ziegler *et al.* (1993) developed a similar procedure to evaluate the COP of multi-effect cycles using the concept of superposition. Instead of using the heat loads of the various components of elementary cycles, like Arh and Gaspersic (1989), Ziegler *et al.* (1993) used the concept of superposition and the COPs of the fundamental cycles to evaluate multi-effect systems.

Arh and Gaspersic (1989) and Ziegler *et al.* (1993) both document the large number of potential multi-effect configurations, and conclude that system-specific detailed simulation would be very time intensive. To address this need, Grossman and Zaltash (2001) developed ABSIM, a modular absorption system simulation code. In its current form, ABSIM can be used to design and simulate an advanced absorption system using a graphical user interface with no

extensive programming required. Grossman and Zaltash (2001) highlight some of the simulations of lithium bromide – water and ammonia-water systems.

Grossman and Zaltash (2001) simulated and compared equivalent quadruple, triple and double-effect lithium bromide - water cycles. In each cycle, the uppermost desorber is externally heated, while the lower desorbers are heated from the condenser of the higher temperature cycle above. To establish a baseline for comparison, heat exchangers of the same conductance are used in every stage of each cycle. Each cycle was simulated across a range of high temperature desorber supply temperatures, but the COPs at the optimal points provide for comparison between the cycles. At optimal efficiency, the quadruple-effect system COP approaches 2.0, the triple-effect design achieves a COP of 1.75, and the COP of the double-effect cycle is 1.4. While the more complex systems achieve higher COPs, they require larger total heat exchanger area and higher supply temperatures. For the double-effect cycle, the heat supply temperature must be between 150 – 175°C, while it must be 200 – 230°C for the triple-effect, and 250 – 300°C for quadruple-effect cycle. They also document the potential to significantly increase the COP of ammonia-water systems by implementing more complex cycles employing internal heat recovery. The Generator – Absorber Heat Exchange (GAX) cycle is one such advanced cycle; heat rejected by the absorption process is internally recovered by the desorber. Grossman and Zaltash (2001) reported that at optimal conditions, the GAX cycle can achieve a COP near 1.3, compared to 0.6 for the standard single-effect system. They do not discuss the economic viability of the theoretically superior, yet increasingly complex, advanced systems considered here.

Garimella *et al.* (1996) also considered a gas-fired GAX system using a modified version of the ABSIM program. Their modification enabled simulation of the combustion gases in a burner module and included the psychrometric properties of atmospheric air; with these

modifications, a realistic system COP could be determined, including heat transfer to heat sources and sinks and combustion losses in the desorber. They used a parametric analysis to optimize the size of the components within the system to maximize the COP, while maintaining minimal heat exchanger area. Simulating the cycle across a range of ambient temperatures, Garimella *et al.* (1996) found the COP to decrease with increasing ambient temperature, from 0.97 at 18°C to 0.855 at 46°C, with a nominal COP of 0.935 at 35°C. The GAX system was also considered in the heating mode, and simulations showed a COP of 1.51 at an ambient temperature of 8°C.

The modified ABSIM code was also used to investigate a triple-effect cycle by Garimella *et al.* (1997). They considered the dual-loop triple-effect cycle, the configuration most suited to the thermo-physical property limitations of the ammonia-water working pair. This configuration uses two coupled single-effect cycles; the lower temperature desorber recovers the heat of condensation, absorption and rectification from the high temperature cycle. In their study, ammonia-water was used in the high temperature loop, while both ammonia-water and ammonia-sodium thiocyanate were studied for the low temperature loop – the salt solution eliminates the need for rectification. Heat exchanger UAs were optimized within a maximum total conductance before a parametric study was conducted over a range of ambient conditions. As anticipated, the COP decreases with increasing ambient temperature in the cooling mode and increases with the ambient temperature in the heating mode with nominal cooling and heating COPs of 0.76 at 35°C, and 1.37 at 8°C, respectively. The performance of the both ammonia-water and ammonia-sodium thiocyanate systems were equivalent, with the need for a rectifier eliminated in the latter system. However, Garimella *et al.* (1997) report that the triple-effect system simulated in this study has a lower COP than a double-effect cycle if the total heat

exchanger conductance is kept the same. This finding underscores the principal concern limiting the implementation of advanced, multi-effect systems; while they may be theoretically superior to simpler cycles, enhancements to performance do not often balance the expense of fabricating and controlling systems of increased complexity. While the direction of innovation has typically used increasing system complexity, researchers have also focused on refining the heat exchanger technology based on a better understanding of the fundamental heat and mass transfer processes.

2.3 Component Level Investigations

The efficient operation of an absorption system most significantly relies on the design and performance of the absorber and desorber. These critical components are characterized by coupled heat and mass transfer processes involving mixtures of fluids with widely disparate properties. Fernandez-Seara *et al.* (2007) report that most component-level investigations have focused on absorber design. However, while absorber design is critically important and has been extensively studied, the desorber is also a significant component; the generation of a high purity refrigerant stream is essential to the effective operation of an absorption system. The desorbers in ammonia-water absorption systems in particular must be designed to ensure a high purity refrigerant stream; because the vapor pressure of water is not insignificant compared to that of ammonia in the generation process, there will always be a small fraction of water in the generated refrigerant stream. Fernandez-Seara *et al.* (2006) report that this distillate water content effectively determines the evaporator and absorber pressure, which regulates the absorption temperature and concentrated solution concentration. The pressure in the condenser and desorber, and thus the weak solution concentration, are similarly influenced by the water content of the refrigerant stream. Furthermore, increased distillate content requires a larger

temperature glide in the evaporator to ensure complete vaporization; if this temperature glide is not achieved, water can accumulate in the evaporator, causing the operation of the system to shift from its design point.

Fernandez-Seara *et al.* (2006) conducted a computational study to quantify these adverse effects of distillate water content in the refrigerant stream. They considered a single effect ammonia-water absorption system with a distillation column with both adiabatic stripping and rectifying sections. The cycle performance was studied while varying the Murphree effectiveness of these distillation column components, thus manipulating the refrigerant purity. Their single effect cycle was modeled to operate with a COP of 0.18 with no vapor refinement – where the stripping and rectifying effectiveness are both 0 – and a COP of 0.50 with the most effective vapor refinement procedures in place. The simulations also demonstrate that the ammonia enrichment process is more important as the absorption and condensation temperatures increase, and as the vapor temperature decreases.

Recognizing that ammonia-water absorption system performance is severely inhibited if the refrigerant stream is contaminated by distillate water content, researchers have implemented various vapor refinement strategies. Most rely on the partial condensation of the vapor stream; because of its higher boiling point, absorbent vapor will preferentially condense out of the refrigerant if the vapor stream is cooled. This cooling is typically effected within a rectifier by cooling with either the concentrated solution from the absorber, or an external coupling fluid. The refrigerant vapor can also be purified by establishing vapor-liquid counterflow, whereby heat and mass transfer are enabled between the two phases in preferential directions. The concentrated solution can be used to establish this vapor-liquid interaction in an analyzer, above the desorber.

Fernandez-Seara *et al.* (2002) report the development of a combined heat and mass transfer model to analyze a packed bed rectifier. In their model, a finite-difference procedure was used to characterize the combined heat and mass transfer process; the behavior of the ammonia - water vapor mixture was considered using the binary condensation model of Colburn and Drew (1937). A parametric study was conducted to determine the geometric parameters of a distillation column optimized for specified conditions. Their study revealed the vapor mass transfer coefficient to have the most significant effect on the distillate ammonia concentration, while the influence of other transfer coefficients is negligible.

This same group incorporated this finite-difference distillation column model into a larger single-stage absorption system simulation, as reported in Sieres and Fernandez-Seara (2006). In this larger system model, helical-coil water- and solution-cooled rectifiers are included above the adiabatic distillation column. The model was used to optimize the geometric parameters of these components to maximize the system COP. The authors note that the adiabatic sections alone are not sufficient to achieve the required refrigerant concentration; the water- and solution-cooled rectifiers are necessary if high refrigerant purity is required. The cycle model demonstrated that the solution-cooled rectifier can increase the system COP by recycling heat within the system, while the water-cooled rectifier causes a slight COP reduction.

Mendes *et al.* (2007) developed a solar-powered ammonia-water absorption system employing a creative ammonia purification procedure. In their system, the rich solution is introduced to the desorber as a spray. The vapor generated within the desorber is refined as it rises through the sprayed concentrated solution, eliminating the need for a rectifier. The authors present experimental data on the performance of this vapor refinement technique. The rich solution spray generated an approximately 1% increase in vapor concentration, which was

adequate for the system conditions considered. The observed level of vapor refinement was independent of concentrated solution and vapor flow rates.

Other efforts to increase refrigerant purity in ammonia-water absorption systems have employed novel desorber designs. In an effort to reduce the overall footprint of the absorption machine, several researchers have investigated miniaturized, high flux desorbers. Determan and Garimella (2011) presented the computational and experimental results of one such investigation. A novel miniaturized desorber consisting of microchannel tube banks arranged in several transversely perpendicular rows in a lattice-like configuration (Garimella, 2004) was modeled and tested. Concentrated solution is introduced at the top of the component, and falls over the microchannel tube banks, which carry a high temperature coupling fluid. The small diameter of the coupling fluid microchannels promotes very high tube-side heat transfer coefficients and ensures a high heat transfer area-to-volume ratio, while the flow of solution from each successive tube increases rates of mass transfer by facilitating continual solution redistribution. The vapor generated from desorption flows upward due to buoyancy, in counterflow to the falling solution film. They demonstrated that the most significant heat and mass transfer resistances are on the vapor side, however, incomplete wetting of the tube banks influenced desorber performance more significantly. The same microchannel tube bank component was previously demonstrated as an absorber by Meacham and Garimella (2004); thus, the researchers demonstrated the utility of this microchannel configuration in both absorption and desorption modes.

Other researchers have also investigated compact desorber geometries for absorption systems. Taboas *et al.* (2010) experimentally characterized the flow boiling of ammonia-water in a brazed-plate heat exchanger. They report that numerous researchers have suggested compact plate heat exchangers for absorption systems, but previous investigations have focused on their

application as absorbers. Additionally, the single-phase performance of plate heat exchangers is well documented, but data pertaining to saturated boiling heat transfer are scarce. Therefore, they developed an experimental facility to characterize the flow boiling performance of a brazed-plate heat exchanger. The ammonia-water solution flowed through the central channel of the heat exchanger, and was heated by hot water flowing in two adjacent channels. The effects of mass flux, heat flux, pressure, and ammonia mass fraction were considered. Of these parameters, the mass flux was shown to most significantly influence boiling performance. These experimental results were shown to be comparable to flow boiling experiments conducted under similar conditions in vertical tubes, as reported by Khir *et al.* (2005).

This review of component level studies has demonstrated the need for further investigation in desorber design, optimization and miniaturization. In the ammonia-water absorption literature, the principles and design of absorbers have received considerably more attention. However, the purity of the refrigerant stream has been shown to significantly influence the performance of ammonia-water absorption systems. Advances in heat exchanger technology have presented opportunities to investigate smaller scale, yet higher flux, absorption system components. Further advances in the design of high-flux desorbers will require a more complete understanding of the fundamental heat transfer processes, particularly the boiling of zeotropic mixtures such as ammonia-water.

2.4 Ammonia-Water Pool Boiling

While the ammonia-water working pair has been used for decades in absorption cycles, very limited data are available on the pool boiling of this mixture. Moreover, a comparison of these data to commonly used mixture pool boiling correlations reveals wide discrepancies.

However, a thorough understanding of the boiling performance of this mixture is required for the successful design of a high heat flux desorber.

The boiling performance of zeotropic mixtures, like the ammonia-water pair, is strongly dependent on the mixture composition. Experimental results show that the boiling heat transfer coefficients of the pure components are much higher than those of the mixture; moreover, the mixture boiling coefficients are lower than the linear interpolation from the pure component coefficients. Taboas *et al.* (2007) report several explanations postulated for the inferior boiling performance of the mixture, including a local increase in the liquid temperature near the wall due to a preferential evaporation of the volatile component, a mass transfer resistance to the volatile component moving up towards the bubble interface, a higher energy requirement for generating a bubble nucleus for mixtures, a decrease in the nucleation sites, and a nonlinear variation of mixture properties with composition. When developing a boiling correlation for a zeotropic mixture, researchers typically calculate an ideal mixture boiling coefficient from those of the ideal fluids, and then reduce it with a correction factor to account for these mixture phenomena.

Inoue *et al.* (2002) measured the pool boiling heat transfer coefficients of ammonia-water mixtures over a wide range of mass fractions. In their experiments, the ammonia-water solution was heated over an electrically heated wire. They report that their data are best modeled when the correction factor attributed to Stephan and Korner (1969) is used. This correction factor accounts for both the saturation pressure and the concentration gradient between the vapor and liquid phases. They used the Nishikawa and Fujita (1977) correlation to calculate the pure substance boiling coefficients. When the coefficients of the correction factor are adjusted to the data, they claim that 93% of their data can be predicted to within 27%.

Arima *et al.* (2003), of the same research group, also conducted an experimental study on ammonia-water pool boiling. In their apparatus, a flat silver surface was used as the exposed heating element, as compared to the heated wire used by Inoue *et al.* (2002). Arima *et al.* (2003) also concluded that the Stephan and Korner (1969) correction factor and the Nishikawa and Fujita (1977) correlation for the pure components most closely predicted their data.

Taboas *et al.* (2007) collected data from the literature and compared the boiling performance of pure water and ammonia, and the ammonia-water pair. They compared data from several sources with the pure component correlations of Mostinski (1963), Stephan and Abdelsalam (1980), Cooper (1984) and Gorenflo (1997). For water, all of the correlations predict the data adequately. The results were less consistent when considering pure ammonia. The Mostinski (1963) correlation was shown to predict the data of Inoue *et al.* (2002) and Arima *et al.* (2003) with root-mean-square average error values of 21% and 18%, respectively, while the Stephan and Abdelsalam (1980) correlation predicts the data of Zheng *et al.* (1995) with a root-mean-square average error of 6.8%. When considering the ammonia-water mixture, they note that none of the existing correction factors adequately predict the compiled data, and they developed their own correlation by combining elements of the correction factors of Schlunder (1983) and Thome and Shakir (1987). When paired the correlation of Mostinski (1963) to describe the pure components, their correction factor predicts the ammonia-water data to within 40%.

The inconsistency of the data characterizing the boiling of pure ammonia is further documented by Spindler (2010), who presents a detailed review of the ammonia pool boiling data available in the English, German and Russian literature. After reviewing the data from experiments with various heater materials, pressure ranges and ammonia concentrations, he

recommends the Gorenflo (1997), Mostinski (1963) or Stephan and Preuber (1979) correlations, noting that the Gorenflo (1997) formulation slightly over-predicts the data, and that the pressure effect of the Stephan and Preuber (1979) correlation is too low.

The above discussion of the literature on pool boiling in both pure ammonia and ammonia-water mixtures shows that the results are sparse and at times inconsistent. While some correlations are offered as reliable by some authors, there is not a generally accepted correlation that provides accurate predictions. What is consistent across all of the papers surveyed is the call for additional investigation into this process. The present research effort therefore attempts to contribute to the body of work on the pool boiling of ammonia-water mixtures, and the development of high flux absorption system components.

CHAPTER 3: FLOODED COLUMN HEAT AND MASS TRANSFER MODELING

3.1 Component Overview

The principles of heat and mass transfer are employed here to model the performance of the Flooded Column desorber. The Flooded Column desorber is a simple counterflow component that employs pool boiling to generate ammonia vapor from a concentrated ammonia-water solution. Concentrated solution enters the component from the top, and flows downward through multiple solution-filled parallel columns. A high temperature coupling fluid flows upwards through plates with microchannels on the front and rear surfaces of each parallel flooded column, transferring heat to the solution. This heat addition causes the solution within the columns to undergo pool boiling, generating ammonia-rich vapor, which flows counter-current to the solution. The generated vapor is removed from the top of the component, while the dilute solution is removed from the bottom. One of the parallel columns composing the desorber is

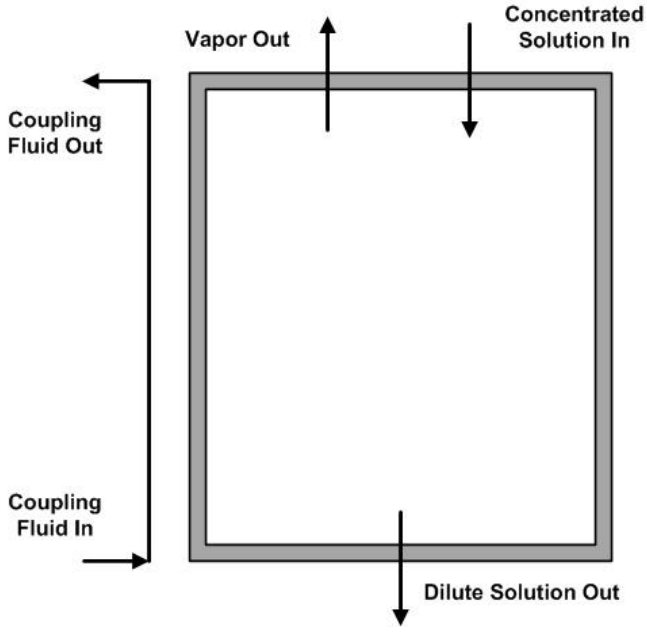

Figure 3.1: Flooded Column Desorber Schematic

The counterflow nature of the component promotes efficient heat and mass transfer between the solution and vapor streams, and the open geometry of the flooded column increases the available vapor-liquid interfacial area. Also, because the design is intended to operate under flooded conditions, counter-current flow limitations are anticipated to be less significant than in other more complicated desorber geometries that can be sensitive to flooding resulting from liquid entrainment by the vapor stream.

3.2 Modeling Overview

An ammonia-water specific pool-boiling correlation, and the Colburn and Drew (1937) method for considering binary mixture condensation are central to this modeling approach. The analysis was carried out on a segmental basis; the geometry was discretized into finite segments to account for changes in temperature, concentration and fluid properties across the desorber,

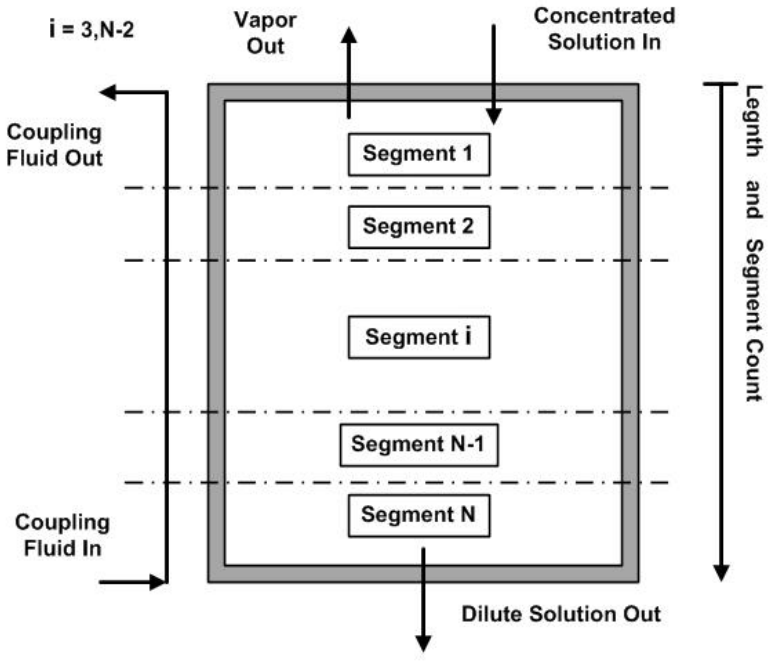

Figure 3.2: Segmented Model Schematic

whereby the outlet conditions of one segment serve as the inlet of the next. Each segment is modeled using uniform heat addition. Figure 3.2 presents a schematic of the segmented desorber. The segment count and length measurements start from the top of the component.

The heat and mass transfer model consists of several sections, to be analyzed in sequential order, with iterations as necessary:

A. Coupling Fluid and Resistance Network Analysis

To determine the wall temperature along the length of the component, thermal resistances between the coupling fluid and the wall are considered

B. Pool-Boiling Correlation

An ammonia-water specific pool-boiling correlation is employed to estimate the boiling heat transfer coefficient

C. Conservation Equations

Mass, Species and Energy conservation equations are formulated for each segment to close the model

D. Vapor-to-Solution Interface

Heat and mass transfer processes between the falling solution and rising vapor streams are considered

Table 3.1 Flooded Column Desorber Model Inputs

Thermodynamic Parameters	
Heating Input	5.443 kW
Coupling Fluid Inlet	
Temperature	180 C
Flowrate	0.084 kg/s
Concentrated Solution Inlet	
Temperature	105.7 C
Concentration	0.4767
Flowrate	0.010 kg/s
System Pressure	2094 kPa

Geometric Parameters	
Flooded Column	
Number of Columns	5
Column Width	108 mm
Microchannel Array	
Channels per Column	75
Hydraulic Diameter	0.44 mm
Channel Perimeter	1.90 mm

The operating point considered in this model is representative of the conditions expected in a 3.5 kW single-effect absorption cycle. Table 3.1 summarizes the thermodynamic and geometric parameters that are specified model inputs. During the modeling process, the desorber is discretized into 50 segments; values from the 25th segment are provided in the discussion of the governing equations.

3.3 Coupling Fluid and Resistance Network Analysis

The analysis begins by considering the coupling fluid supplied to the component. This coupling fluid flows upward through microchannel plates on the front and back of each flooded column, as shown conceptually in the rear plate in Figure 3.3.

The amount of heat supplied by the coupling fluid to any segment of the desorber is, by definition, constant for all segments and known from Equation 3.1. While the heat duty of each segment is constant, the segment lengths change to account for the varying driving temperature

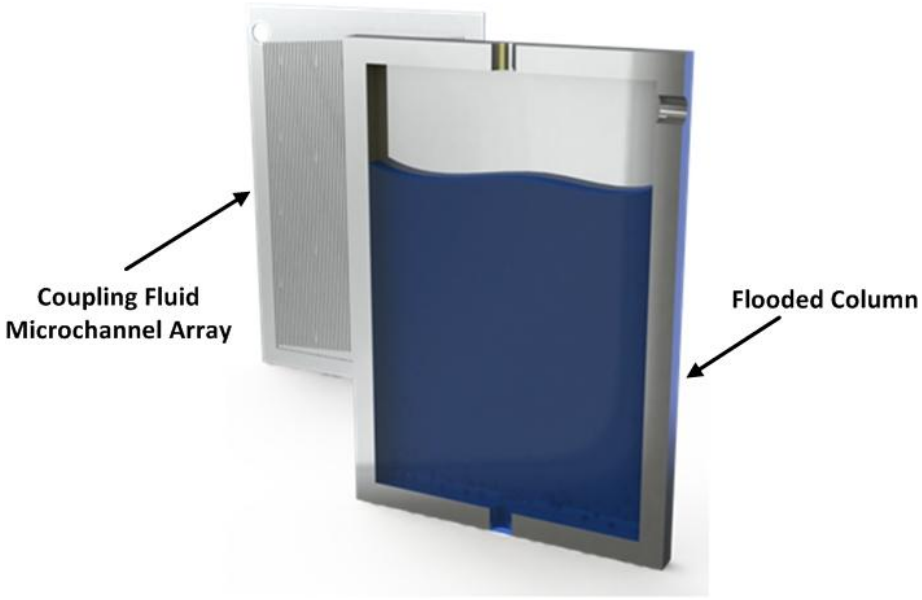

Figure 3.3: Flooded Column Desorber with Microchannel Coupling Fluid Plate (Image Courtesy of Jared Delahanty)

differences and heat transfer coefficients. The total heat applied to the desorber and the number of segments are specified parameters.

$$q_{segment} = \frac{q_{Total}}{N_{Segments}} \tag{3.1}$$

The total heating input to the desorber is 5.443 kW, and the component is divided into 50 segments, thus $q_{segment} = 0.1089$ kW.

$$q_{Segment} = \frac{5.443\ \text{kW}}{50\ \textit{Segments}}; \qquad q_{\textit{Segment}} = 0.1089\ \frac{\text{kW}}{\textit{Segment}}$$

The mass flow rate of the coupling fluid, and its temperature at the component inlet, are also specified parameters. Equation 3.2 employs these parameters to determine the outlet temperature of the coupling fluid from any segment; this outlet temperature serves as the inlet temperature for the following segment. The coupling fluid specific heat is taken from a curve fit of manufacturer-provided data for Paratherm NF.

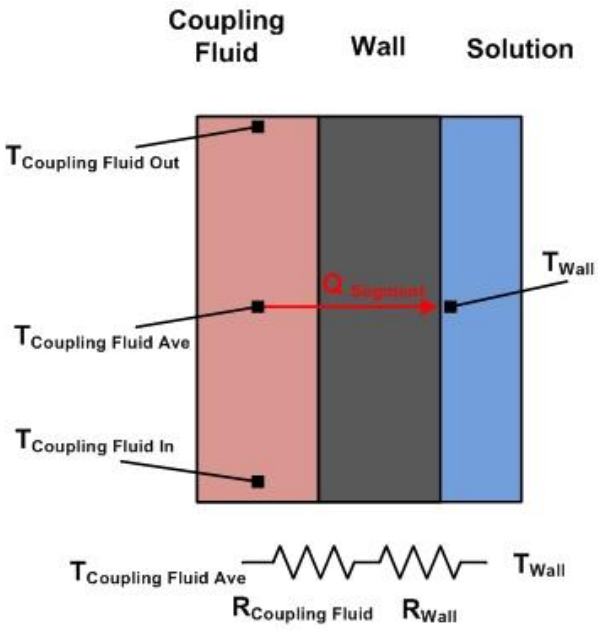

Figure 3.4: Coupling Fluid – to – Wall Resistance Network

$$q_{segment} = \dot{m}_{Coupling\ Fluid} \bullet Cp_{Coupling\ Fluid} \bullet \left(T_{Coupling\ Fluid,\ Inlet} - T_{Coupling\ Fluid,\ Outlet}\right) \quad (3.2)$$

For the middle, or 25th segment, the Paratherm specific heat is determined to be 2.605 kJ $kg^{-1}K^{-1}$, and the inlet coupling fluid temperature is 167.7˚C. With a total coupling fluid flowrate of 0.084 kg s^{-1}, the outlet coupling fluid temperature is calculated to be 167.2˚C.

$$0.1089\ \text{kW} = 0.084\ \frac{\text{kg}}{s} \bullet 2.605 \frac{kJ}{kgK} \bullet \left(167.7 - T_{CF,Out}\right); \qquad T_{CF,Out} = 167.2^{\circ}\text{C}$$

Having determined the coupling fluid temperature at the inlet and outlet of each segment, the average coupling fluid temperature in each segment easily follows. To determine the average wall temperature for each segment, a resistance network is considered between the coupling fluid and the solution side of the flooded column wall. The convection resistance between the coupling fluid and the surrounding channel, and the conduction resistance through the channel wall are considered in series. All of the heat supplied to the segment, $Q_{segment}$, is assumed to flow

across this 1-D thermal pathway. Figure 3.4 presents this geometry and resistance network schematically.

The total thermal resistance across this network is the sum of the two components, as shown in Equation 3.3. The conduction resistance across the shim wall, R_{Wall}, is determined from the wall thickness, surface area and conductivity, as shown in Equation 3.4. Equation 3.5 shows that $A_{Boiling}$ for a given segment is the product of twice the column width and segment length and the number of columns, noting that the coupling fluid channels heat both the front and back of each column.

$$R_{CF\text{-}to\text{-}Wall} = R_{CF} + R_{Wall} \tag{3.3}$$

$$R_{Wall} = \frac{\delta_{wall}}{\left(A_{boiling} k_{wall}\right)} \tag{3.4}$$

$$A_{boiling} = \left(\text{Column Width}\right) L_{segment} \bullet N_{Columns} \bullet 2 \tag{3.5}$$

The closed model calculates the length of the 25th segment to be 5.97 mm. The column width and count are specified as 108 mm and 5, respectively. As shown in Equation 3.5, $A_{boiling}$ = 0.006452 m^2 for this middle segment.

$$A_{boiling} = \left(0.108m\right) 0.00597\text{m} \bullet 5 \bullet 2; \quad A_{boiling} = 0.006452\ \text{m}^2$$

Figure 3.5 shows a schematic of the cross-section of the microchannel array and the flooded column. This figure shows that the wall thickness is 0.15 mm The temperature-dependent thermal conductivity of stainless steel is taken as the wall conductivity. For the 25th segment, k_{Wall} = 17.02 W m^{-1}K^{-1}. From Equation 3.4, the wall conduction resistance is calculated to be R_{Wall} = 0.001366 K W^{-1}.

$$R_{Wall} = \frac{0.15mm}{\left(0.006452\ m^2 \bullet 17.02\ \frac{W}{mK}\right)}; \qquad R_{Wall} = 0.001366\ K/W$$

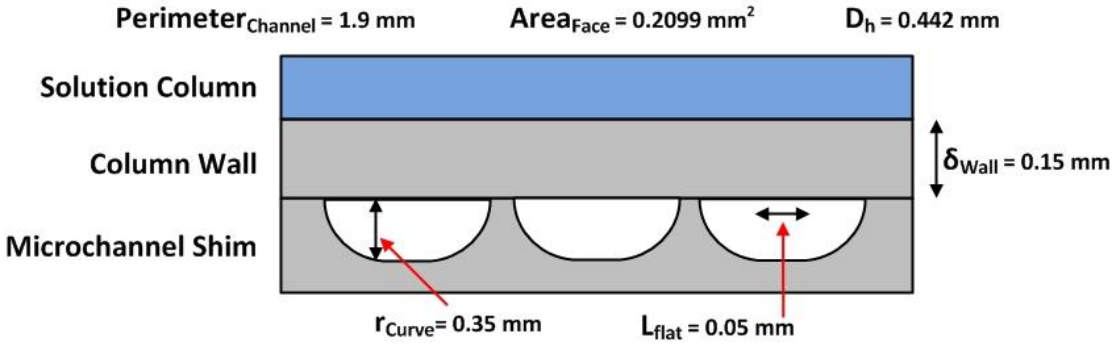

Figure 3.5: Flooded Column Desorber Cross-Section with Microchannel Geometry

The convection resistance from the coupling fluid to the shim wall is determined from the coupling fluid heat transfer coefficient and the total wetted area, as shown in Equation 3.6. This relationship assumes minimal temperature gradients within the microchannel shim and approximates the microchannel array as a set of parallel fins with efficiency approaching 1. This assumption is supported by the large shim thermal conductivity and the geometric dimensions of the microchannels; sample fin efficiency calculations supporting this assumption are presented in Appendix B. For each segment, $A_{CouplingFluid}$ is determined from channel geometric parameters shown in Figure 3.5, as calculated in Equation 3.7. The Sparrow and Haji-Sheikh (1965) correlation for single phase heat transfer in semicircular microchannels, as reported by Kakac *et al.* (1987) and shown in Equation 3.8, is used to determine the coupling fluid heat transfer coefficient.

$$R_{CouplingFluid} = \frac{1}{\alpha_{CouplingFluid} A_{CouplingFluid}} \tag{3.6}$$

$$A_{\text{Coupling Fluid}} = \text{Perimeter}_{\text{Channel}} \bullet N_{CFChannels} \bullet L_{\text{Segment}} \bullet N_{Columns}$$
$$\text{where Perimeter}_{\text{Channel}} = (\pi + 2) r_{\text{curve}} + 2L_{\text{Flat}} \tag{3.7}$$

$$\frac{\alpha D_h}{k_{CF}} = 2.0705\left(1 + 2.2916\phi - 2.5682\phi^2 + 1.4815\phi^3 - 0.3338\phi^4\right)$$
$$\text{where } \phi = \frac{\pi}{2} \tag{3.8}$$

The Paratherm thermal conductivity is temperature dependent, and at the 25th segment, is calculated from a property curve fit to equal $k_{\text{Fluid}} = 0.0973\ \text{W m}^{-1}\text{K}^{-1}$. The channel hydraulic diameter, where $D_h = 4A_{\text{Face}}/\text{Perimeter}$, is calculated from the geometric specifications to be $D_{\text{H,Channel}}$ = 0.442 mm. Using these values, Equation 3.8 yields a coupling fluid heat transfer coefficient of 899.8 W m^{-2}K^{-1} at the 25th segment.

$$\frac{\alpha(0.442mm)}{0.0973\frac{\text{W}}{mK}} = 2.0705\left(1 + 2.2916\left(\frac{\pi}{2}\right) - 2.5682\left(\frac{\pi}{2}\right)^2 + 1.4815\left(\frac{\pi}{2}\right)^3 - 0.3338\left(\frac{\pi}{2}\right)^4\right);$$
$$\alpha = 899\frac{W}{m^2K}$$

The geometric specifications in Figure 3.5 show that r_{Curve} = 0.35 mm and L_{Flat} = 0.05 mm . From these values and Equation 3.8, the channel perimeter is calculated to be 1.9 mm. Each flooded column is heated on the front and back by shims of 75 microchannels, for a total of 150 microchannels per column. With these values, Equation 3.7 yields $A_{\text{Coupling Fluid}}$ = 0.008515 m^2 for the 25th segment.

$$A_{\text{Coupling Fluid}} = 1.9\text{mm} \bullet 150 \bullet 5.97\text{mm} \bullet 5; \qquad A_{\text{Coupling Fluid}} = 8515\ \text{mm}^2 = 0.008515\ \text{m}^2$$

Equation 3.6 yields the coupling fluid convection resistance for the 25th segment, R_{CF} = 0.1305 K W^{-1}. Equation 3.3 provides the total series resistance as $R_{CF\text{-}Wall}$ = 0.1319 K W^{-1}.

$$R_{CouplingFluid} = \frac{1}{899\frac{W}{m^2K}\left(0.008515\text{m}^2\right)}; \qquad R_{CouplingFluid} = 0.1305 \text{ K/W}$$

$$R_{CF\text{-to-Wall}} = 0.1305\frac{K}{W} + 0.001366\frac{K}{W}; \qquad R_{CF\text{-to-Wall}} = 0.1319 \text{ K/W}$$

It is clear from these calculations that the convection within the coupling fluid microchannels contributes most significantly to the resistance across this thermal pathway. Conduction across the thin, highly conductive flooded column wall is less significant.

Figure 3.6 presents a plot of the coupling fluid heat transfer coefficient along the length of the desorber. This heat transfer coefficient decreases toward the bottom of the desorber; this decrease is due to temperature dependent variations in the coupling fluid thermal conductivity. It

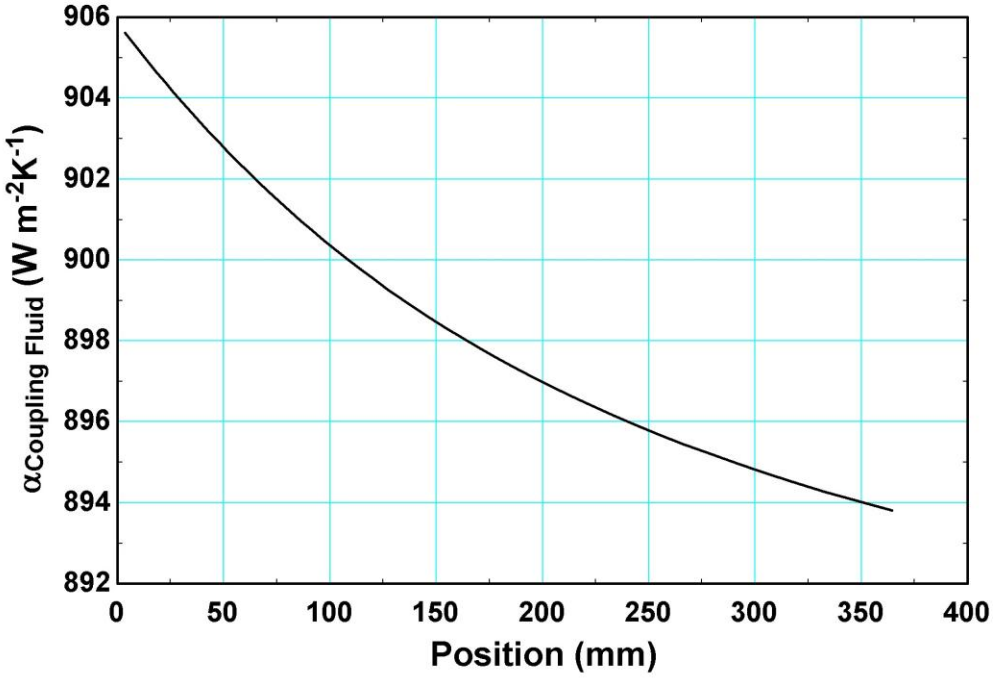

Figure 3.6: Coupling Fluid Heat Transfer Coefficient vs. Position

should be noted that the 25th segment, which has been used in the preceding sample calculations, corresponds to Position = 120 mm, measured from the top of the desorber.

Figure 3.7 presents a plot of resistances comprising the thermal network between the coupling fluid and wall temperatures. Clearly, the coupling fluid convection resistance dominates this thermal pathway: conduction across the thin, highly conductive wall does not significantly deter heat transfer. The coupling fluid convective resistance decreases towards the bottom of the desorber; this is because the segment lengths are not specified, but are instead determined by the model. Figure 3.8 shows that the segment length increases toward the bottom of the component. Equivalently, it is understood that the heat flux transferred to the component decreases down the length of the desorber; the heat flux is greatest at the top of the component, which will be shown

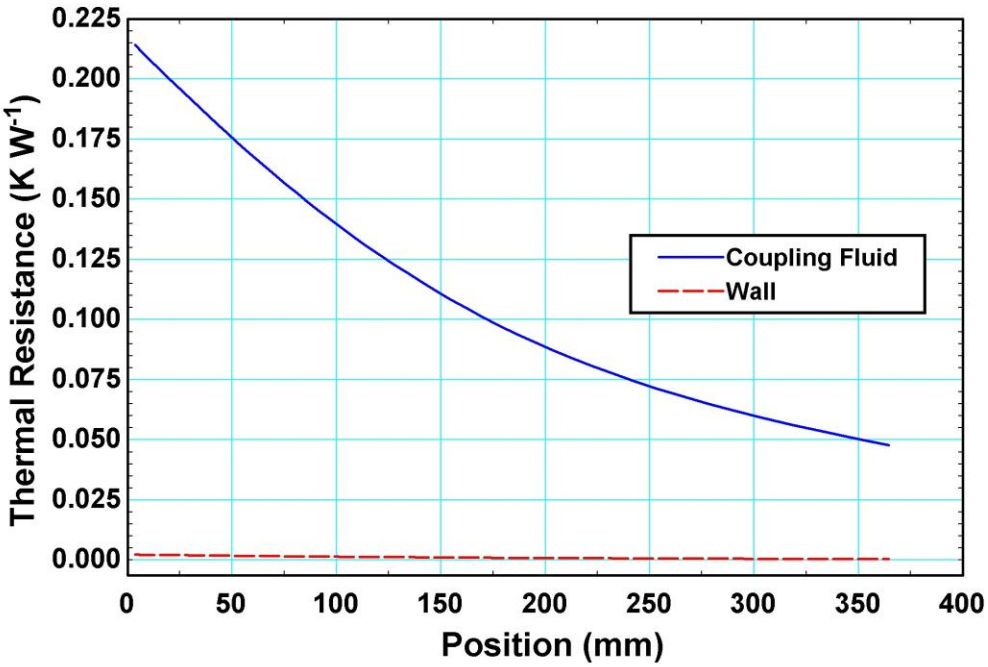

Figure 3.7: Coupling Fluid and Wall Thermal Resistances

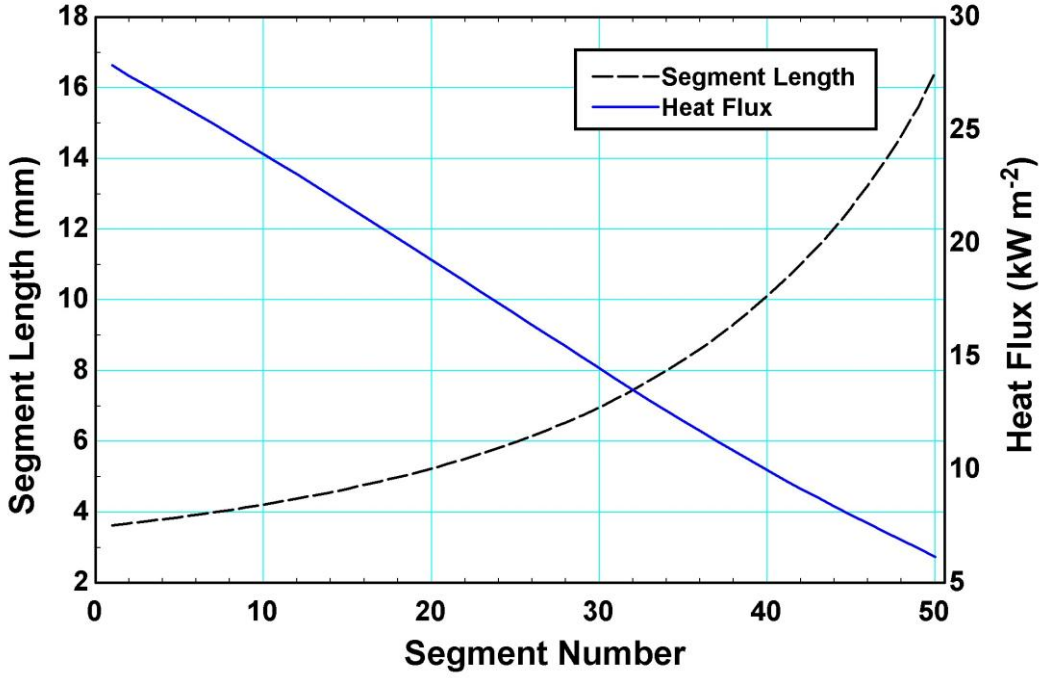

Figure 3.8: Segment Length vs. Segment Number

to be the location of the largest temperature differences between the solution and coupling fluid. The increased segment lengths observed in Figure 3.8 serve to increase the available heat transfer area, causing the decreased thermal resistance at the bottom of the component observed in Figure 3.7.

With the total thermal resistance calculated for every segment, Equation 3.9 can be used to determine the average wall temperature across the length of the component.

$$Q_{segment} = \frac{\left(T_{Coupling\ Fluid,\ Ave} - T_{Wall\ Surface}\right)}{R_{CF\text{-}to\text{-}Wall}} \tag{3.9}$$

At the 25th segment, with an average coupling fluid temperature of 167.5 ˚C, Equation 3.9 yields T_{Wall} = 153.1˚C.

$$0.1089\ \text{kW} = \frac{\left(167.5\ \text{C} - T_{\text{Wall Surface}}\right)}{0.1319\ \frac{\text{K}}{W}}; \qquad T_{\text{Wall Surface}} = 153.1\ ^{\circ}\text{C}$$

Figure 3.9 presents a plot of the average coupling fluid and wall temperatures across the length of the desorber. The coupling fluid is hottest at the lowest point of the component, Position = 364 mm, where it enters the desorber. The highest rates of change in temperature are at the top of the component, where the thermal resistance is the highest.

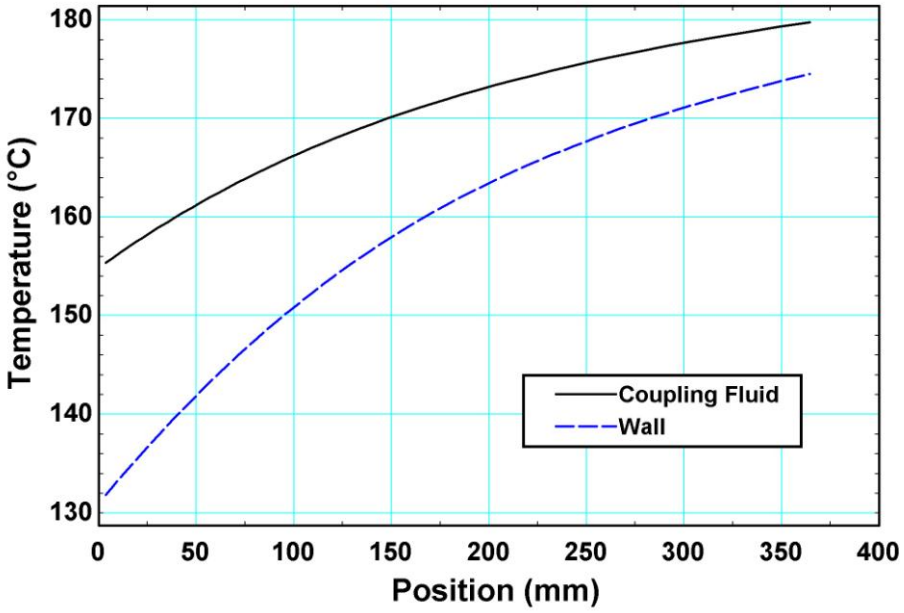

Figure 3.9: Coupling Fluid and Wall Temperatures

3.4 Ammonia - Water Pool-Boiling Correlation

The preceding analysis described the procedure used to determine the temperature of the wall adjacent to the ammonia-water solution. If this wall temperature is sufficiently in excess of the saturation temperature of the solution, phase change can be anticipated. Because the solution

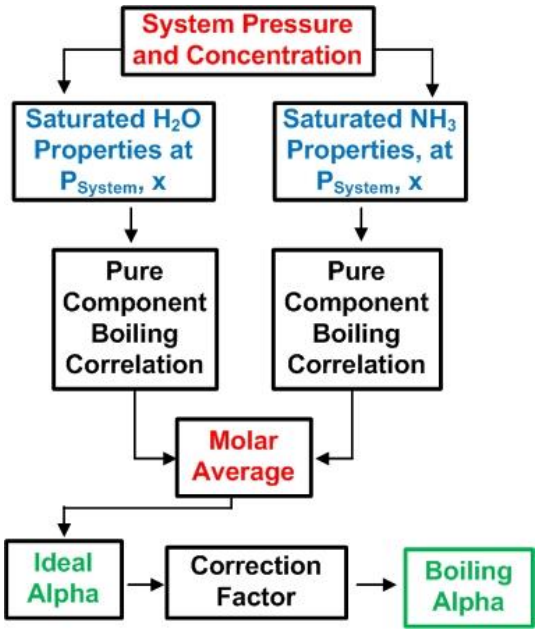

Figure 3.10: Ammonia-Water Correlation Flowchart

flowrate through the flooded column is low relative to the volume of the column, this process will be modeled as pool boiling. Identifying and implementing a pool-boiling correlation appropriate for an ammonia-water mixture is an important step in the analysis. The pool-boiling performance of zeotropic mixtures such as ammonia-water is strongly dependent on the concentration of the mixture, due to the coupled heat and mass transfer phenomena occurring between the components. While the data available for ammonia-water mixtures are relatively scarce, several correlations for the mixture boiling heat transfer coefficients have been proposed. The most successful correlations generally follow the form outlined in Figure 3.10: a pure component correlation is used to determine the boiling heat transfer coefficients of each component at the system pressure and heat flux; if required by the correlation, fluid properties for both components are calculated at the saturation temperatures of each fluid at the operating total pressure. An ideal mixture heat transfer coefficient is calculated from the pure component heat transfer coefficients based on a mole fraction-weighted average. This ideal coefficient is

then adjusted by a correction factor to account for the reduced effectiveness of the boiling process due to the mass transfer effects in the ammonia-water mixture

Inoue *et al.* (2002) used the correction factor of Stephan and Korner (1969) to correlate their data to within ±27%. This correction factor, presented as Equation 3.10, relates the reduced efficiency of the mixture boiling process to both the system pressure and the difference in concentration between the solution and vapor.

$$F_{D,StephanKorner} = \left(1+3.1\left(\tilde{x}_{Vapor,ave} - \tilde{x}_{Solution,ave}\right)\left(0.88+0.12P_{System,Bar}\right)\right)^{-1} \qquad (3.10)$$

This correction factor is used to adjust the ideal mixture boiling coefficient, as shown in Equation 3.11.

$$\alpha_{Boiling} = \alpha_{Boiling,Ideal} F_{D,StehpanKorner} \qquad (3.11)$$

The ideal boiling coefficient is calculated from the pure component boiling coefficients and the molar solution concentration from Equation 3.12

$$\alpha_{Boiling,Ideal} = \left(\frac{\tilde{x}_{Solution,Ave}}{\alpha_{Boiling,NH_3}} + \frac{1-\tilde{x}_{Solution,Ave}}{\alpha_{Boiling,H_2O}} \right)^{-1} \qquad (3.12)$$

The remaining challenge is to define the pure component boiling coefficients. Several different pure component pool-boiling correlations were used in the literature to correlate boiling data for ammonia-water mixtures. Five pure component pool-boiling correlations were considered in the present study: Rohsenow *et al.* (1998), Mostinski (1963), Nishikawa and Fujita (1977), Stephan and Abdelsalam (1980), and Gorenflo (1997). A review of the literature suggested that the Stephan and Abdelsalam or Gorenflo correlations would most reliably calculate boiling heat transfer coefficients for ammonia, while any of the correlations should be expected to sufficiently model the boiling of water (Arima *et al.*, 2003).

Figure 3.11 shows a plot of the mixture boiling coefficients predicted by each of these correlations within the flooded column model. In all cases except the Rohsenow (mixture) plot, the Stephan-Korner correction factor was used to adjust the ideal coefficients provided by the various correlations. The Rohsenow (mixture) plot directly employed the Rohsenow *et al.* (1998) correlation using fluid properties determined for the mixture. While all of the plots employing the correction factor follow the same trend and are within the same order of magnitude, the Gorenflo and Stephan and Abdelsalam correlations achieved the best agreement. Ultimately, the Gorenflo correlation (Equation 3.13), was implemented to calculate the pure component boiling heat transfer coefficients. This is a reduced pressure correlation with empirical parameters fit to each fluid. P_r represents the reduced pressure, defined as the ratio of the saturation pressure to the critical pressure of the fluid. The saturation pressure used for each fluid is the partial pressure of that component, calculated from Equation 3.14.

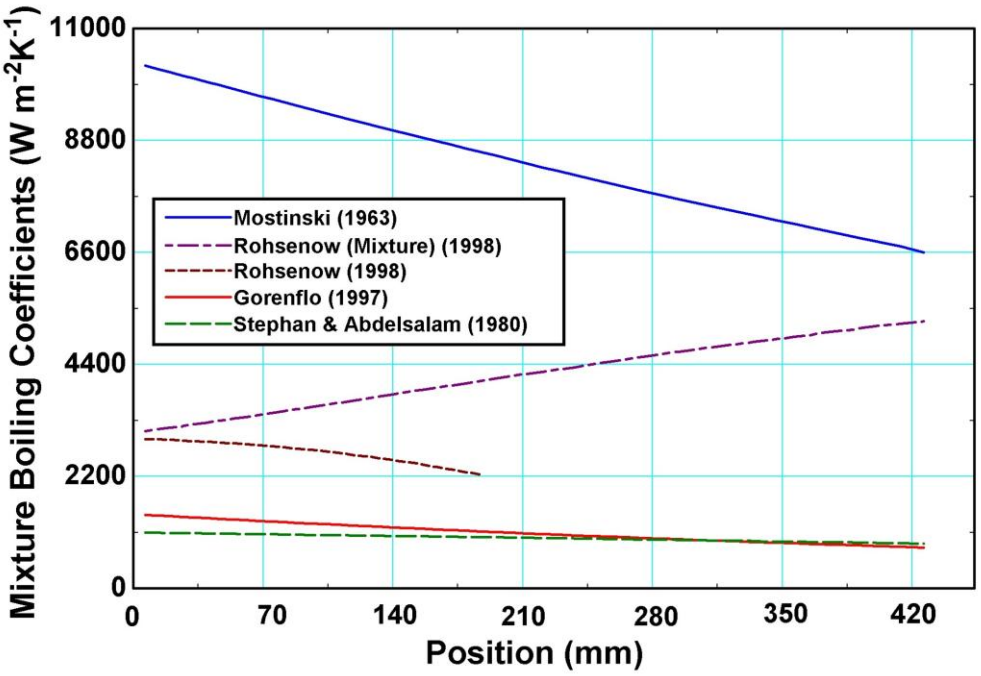

Figure 3.11: Mixture Pool Boiling Coefficients from Several Correlations

$$\frac{h}{h_O} = \left(\frac{q''}{q''_O} \right)^{n(P_r)} F(P_r) \tag{3.13}$$

For Ammonia

$$F(P_r) = 1.2P_r^{0.27} + \left(2.5 + \frac{1}{1-p_r} \right) p_r; \quad n(p_r) = 0.9 - 0.3p_r^{0.15}; \quad q''_o = 7000$$

For Water

$$F(P_r) = 1.73P_r^{0.27} + \left(6.1 + \frac{0.68}{1-p_r} \right) p_r^2; \quad n(p_r) = 0.9 - 0.3p_r^3; \quad q''_o = 5600$$

$$\begin{aligned} P_{Ammonia} &= P_{System}\tilde{x} \\ P_{Water} &= P_{System}(1-\tilde{x}) \end{aligned} \tag{3.14}$$

The desorber operates at a system pressure of 2094 kPa, and at the 25th segment, the molar solution concentration is 0.3551. From Equation 3.14, the partial pressures of ammonia and water are 701.7 kPa and 1392.3 kPa, respectively. The critical pressures of ammonia and water are 11333 kPa and 22064 kPa. Thus, the reduced pressures for ammonia and water at the 25th segment are 0.0656 and 0.0612, respectively. Additionally, q''_o is defined as 20,000 W m^{-2}, and $q'' = 16{,}870$ W m^{-2} for the 25th segment.

With these pressure ratios, the Gorenflo correlation, Equation 3.13, provides ideal ammonia and water boiling coefficients at the 25th segment as 4973 W m^{-2} K^{-1} and 4171 W m^{-2} K^{-1}, respectively.

$$\frac{h_{Ammonia}}{7000} = \left(\frac{16870}{20000}\right)^{n(P_r)} F(P_r)$$

$$n(P_r) = 0.9 - 0.3P_r^{0.15} = 0.9 - 0.3(0.0656)^{0.15} = 0.7006$$

$$F(P_r) = 1.2(P_r)^{0.27} + \left(2.5 + \frac{1}{1+P_r}\right)P_r = 1.2(0.065)^{0.27} + \left(2.5 + \frac{1}{1+0.065}\right)0.065 = 0.8006$$

$$h_{Ammonia} = 4973 \ \frac{W}{m^2K}$$

$$\frac{h_{Water}}{5600} = \left(\frac{16870}{20000}\right)^{n(P_r)} F(P_r)$$

$$n(P_r) = 0.9 - 0.3P_r^{0.3} = 0.9 - 0.3(0.0612)^{0.3} = 0.7702$$

$$F(P_r) = 1.73(P_r)^{0.27} + \left(6.1 + \frac{0.68}{1+P_r}\right)P_r^{\,2} = 1.73(0.0612)^{0.27} + \left(6.1 + \frac{0.68}{1+0.0612}\right)(0.0612)^2 = 0.8389$$

$$h_{Water} = 4171 \ \frac{W}{m^2K}$$

With these pure component boiling coefficients, the ideal mixture coefficient is calculated to be 4425 W m^{-2} K^{-1} using Equation 3.12.

$$\alpha_{Boiling,Ideal} = \left(\frac{0.3551}{4973 \ W/m^2K} + \frac{(1-0.3551)}{4171 \ W/m^2K}\right)^{-1} = 4425 \ \frac{W}{m^2K}$$

The vapor molar concentration is needed to compute the Stephan - Korner correction factor. This concentration is calculated from the closed model to be 0.8826. The resulting correction factor using Equation 3.10 is 0.1527.

$$F_{D,StephanKorner} = \left[1 + 3.1(0.8826 - 0.3551)(0.88 + 0.12(20.94))\right]^{-1} = 0.153$$

Thus, the corrected mixture boiling coefficient is calculated to be 675.6 W m^{-2} K^{-1} from Equation 3.11.

$$\alpha_{Boiling} = 4425(0.153) = 675.6\frac{W}{m^2K}$$

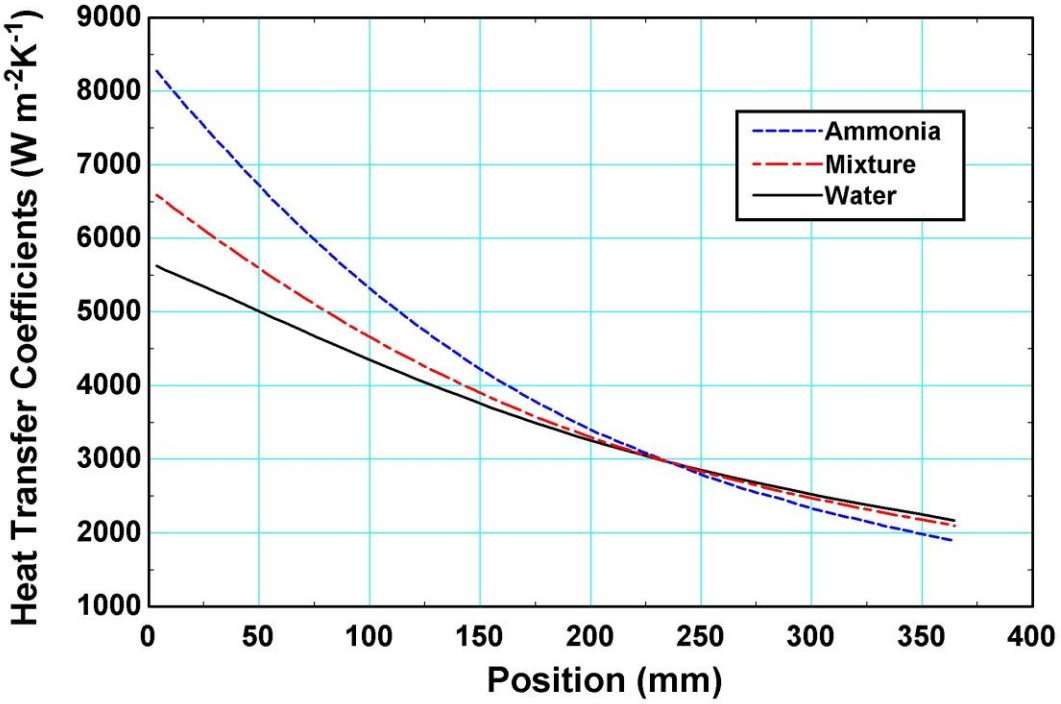

Figure 3.12: NH_3, H_2O and Mixture Ideal Boiling Coefficients

Figure 3.12 presents a plot of the ideal ammonia, water and mixture heat transfer coefficients across the component. The predicted values for both components and the mixture decrease towards the bottom of the component, where the applied heat flux is at its minimum. At the top of the component, the ideal correlation follows the predictions for pure ammonia more closely than at the bottom of the component, underscoring the decrease in concentration of solution towards the bottom of the desorber.

The larger ideal boiling coefficients observed at the top of the component explain the increased heat flux at the top of the desorber, as shown in Figure 3.7. Figure 3.13 presents a plot of the Stephan – Korner correction factor across the component. This correction factor does not significantly change across the length of the component, and remains near 15.6% in all segments.

Having determined the ideal boiling coefficient and the correction factor across the length of the desorber, the adjusted mixture boiling coefficient follows, as plotted in Figure 3.14. As

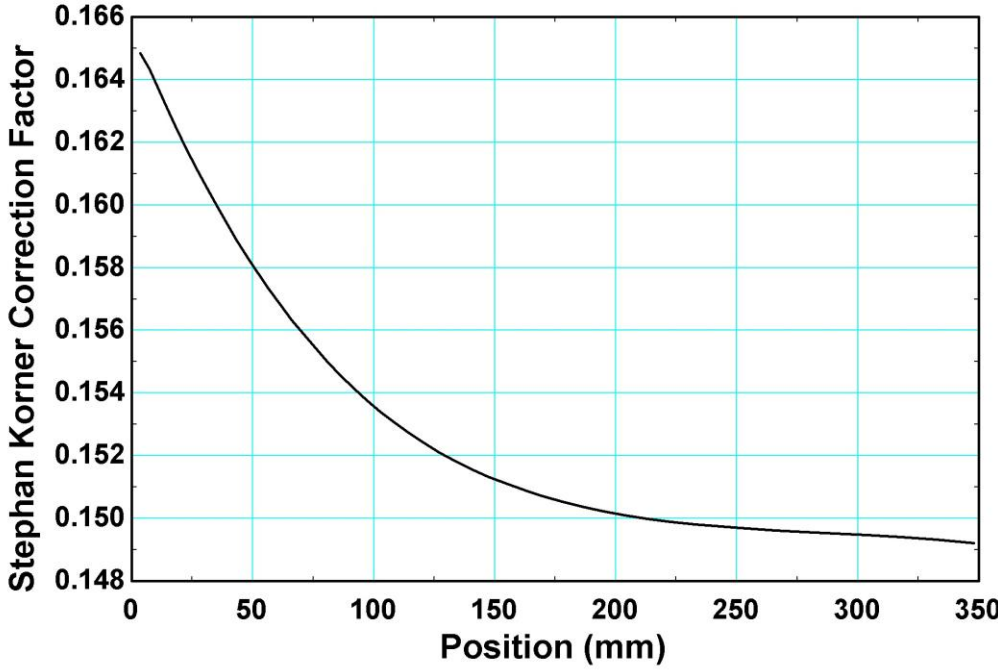

Figure 3.13: Stephan - Korner Correction Factor across Desorber Length

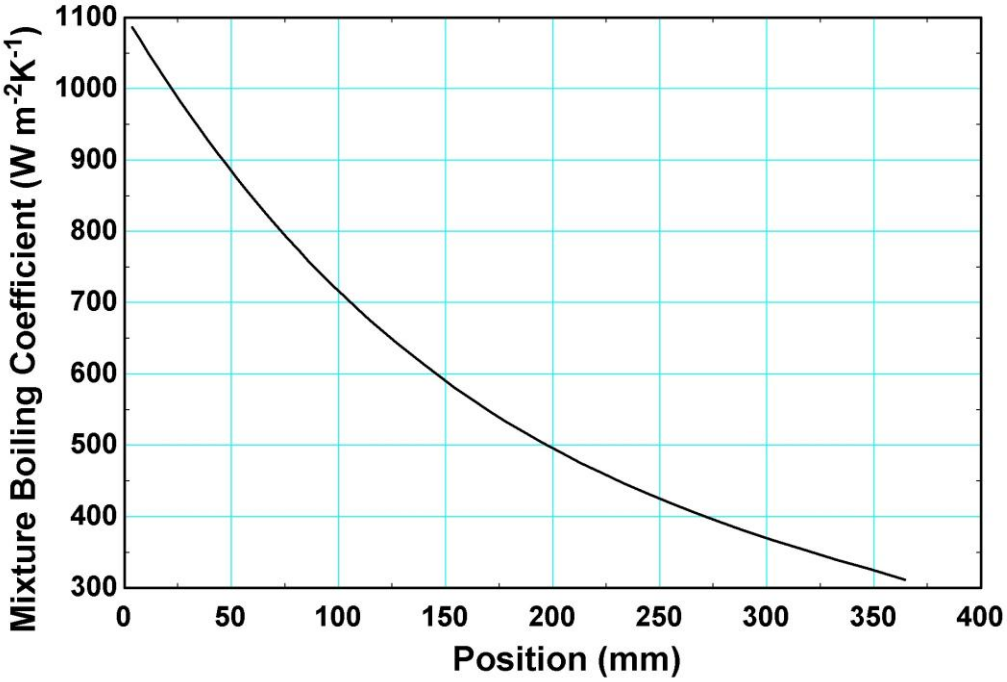

Figure 3.14: NH_3-H_2O Mixture Boiling Coefficient

anticipated, the corrected mixture coefficients closely follow the ideal coefficients from Figure 3.12.

Having calculated the boiling heat transfer coefficients, after previously determining the desorber wall temperatures, the solution saturation temperature can be determined from Equation 3.15.

$$q'' = h_{boiling}\left(T_{Wall} - T_{Sat}\right) \tag{3.14}$$

It is assumed that the saturation temperature calculated in each segment is equal to the average solution temperature in that segment, as shown in Equation 3.16. When this relationship is established for every segment in the completed model, and the solution inlet temperature at the first segment is provided as an specified value, the solution temperatures at the inlet and outlet of every segment are determined.

$$T_{Sat} = T_{Solution,Average} = \frac{1}{2}\left(T_{Solution,Out} + T_{Solution,In}\right) \tag{3.15}$$

At the 25th segment, the boiling coefficient is 675.6 W m^{-2}K^{-1}, the heat flux is 16.87 kW m^{-2} and the wall temperature is 153.1 ˚C, resulting in a saturation temperature of 128.1 ˚C from Equation 3.15. At this segment, the closed model yields a solution inlet temperature of 127.6 ˚C; Equation 3.16 yields a solution outlet temperature of 128.7 ˚C.

$$16.87\frac{kW}{m^2} = 675.6\frac{W}{m^2K}\left(153.1 - T_{Sat}\right); \qquad T_{Sat} = 128.1\,^{\circ}\mathrm{C}$$

$$128.1\ C = T_{Solution,Average} = \frac{1}{2}\left(T_{Solution,Out} + 127.6\right); \qquad T_{Solution,Out} = 128.7\,^{\circ}\mathrm{C}$$

Figure 3.15 presents a plot of the Coupling Fluid, Wall and Solution Temperatures along the length of the desorber. The temperature difference between the solution and wall is relatively

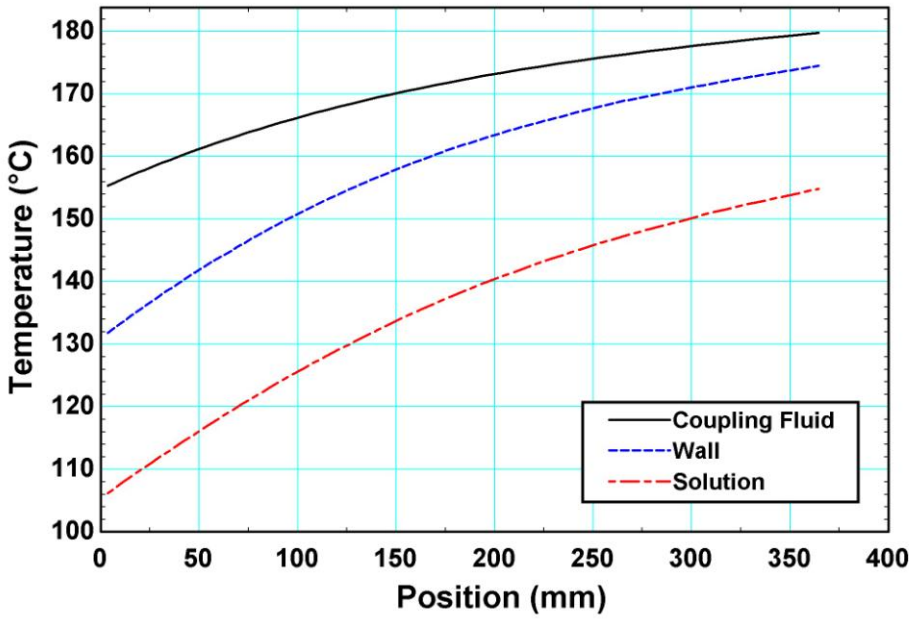

Figure 3.15: Solution, Wall and Coupling Fluid Temperatures

constant across the desorber length, at approximately 22 ˚C. The temperature difference between the wall and solution and the total heat supplied to each segment are roughly constant along the length of the component, but the boiling heat transfer coefficient (Figure 3.14) and the segment length (Figure 3.8) - thus the heat transfer area - behave opposingly, such that the quantity $h_{Boiling} \bullet A_{Boiling}$ is roughly constant across the desorber.

3.5 Conservation Equations

Mass, species and energy balances are applied to each segment in the desorber model. Figure 3.16 presents a schematic representation of the control volumes and streams considered. Vapor and solution flow into and out of each segment at a particular concentration and temperature.

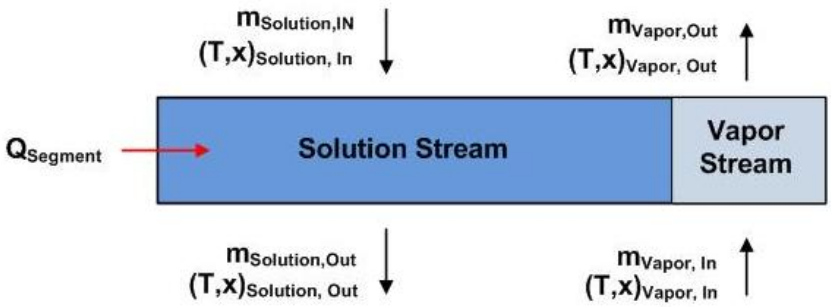

Figure 3.16: Segment Control Volume

The mass, species and energy balances are conducted on this control volume, and are presented as Equations 3.17 - 3.20.

$$\dot{m}_{Solution\ In} + \dot{m}_{Vapor\ In} = \dot{m}_{Solution\ Out} + \dot{m}_{Vapor\ Out} \tag{3.16}$$

$$\dot{m}_{Solution\ In} x_{Solution\ In} + \dot{m}_{Vapor\ In} x_{Vapor\ In} = \dot{m}_{Solution\ Out} x_{Solution\ Out} + \dot{m}_{Vapor\ Out} x_{Vapor\ Out} \tag{3.17}$$

$$\dot{m}_{Solution\ In} h_{Solution\ In} + \dot{m}_{Vapor\ In} h_{Vapor\ In} + q_{Segment} = \dot{m}_{Solution\ Out} h_{Solution\ Out} + \dot{m}_{Vapor\ Out} h_{Vapor\ Out} \tag{3.18}$$

It must also be remembered that the outlet conditions of one segment define the inlet conditions of the next, as shown for the solution and vapor streams in Equations 3.20 and 3.21, respectively. Note the change of indices between these two equations, reflecting the different directions of the counter-flow solution and vapor streams.

$$\text{For Solution: } \left(T,x,\dot{m}\right)_{Out,I} = \left(T,x,\dot{m}\right)_{IN,(I+1)} \tag{3.19}$$

$$\text{For Vapor: } \left(T,x,\dot{m}\right)_{Out,I} = \left(T,x,\dot{m}\right)_{IN,(I-1)} \tag{3.20}$$

Additional specifications required for model closure pertain to the first and last segments. The solution enters the component at the first, or top segment; therefore, the temperature and

flow rate are specified here. Additionally, at the bottom segment, the vapor inlet flow rate is, by definition, zero.

It is now necessary to fully define the thermodynamic state of the ammonia-water mixture at the inlet and outlet of each segment. For the mixture to be fully defined, three of the following properties must be known, while the remainder can be easily calculated: Temperature, pressure, quality, concentration, enthalpy and specific volume. Property functions developed specifically for the ammonia-water mixture are used to define the remaining variables from those supplied.

Three assumptions simplify this problem. First, a minimal pressure drop is assumed along the length of the component, implying that the solution and vapor are at all points at the specified system pressure, 2094 kPa. Second, the vapor stream throughout the component is, by definition, at a quality of 1. Finally, the solution leaving each segment is assumed to be a quality of 0, i.e., exiting as a saturated liquid.

When considering these assumptions, and remembering that previous calculations have determined the solution temperature at the inlet and outlet of each segment, the solution is well defined: at all points, pressure, quality and temperature are known. With the state point defined, the solution concentration and enthalpy are determined from the ammonia-water property functions. Two properties, pressure and quality, are known for all points of the vapor stream – identifying its temperature would fully define the vapor stream.

The vapor rising into a particular segment was generated in the lower segments, where the saturation temperature is higher. The rising vapor stream is thus hotter than the solution it flows through, and can be expected to cool as it transfers heat to the surrounding solution. If this vapor-to-solution heat exchange was as efficient as possible, the vapor temperature at the

segment outlet would equal the solution temperature at the segment inlet; an inequality between these two temperatures should be expected for the actual process. The vapor outlet temperature can be defined based on the solution inlet temperature and this inequality, as shown in Equation 3.22.

$$T_{Vapor,Outlet} = T_{Solution,Inlet} - \Delta_{Inequality} \quad (3.21)$$

Section 3.5 details the analysis employed to determine this temperature inequality, but for the purposes of this discussion, it can be taken as an assumed value. If this inequality is assumed for each segment, the temperature of the vapor stream is known and the state is fixed – the ammonia-water property functions can be used to determine vapor concentration and enthalpy for all points. Under these conditions, and recalling the solution inlet state point as a design specification, only three unknown parameters remain in Equations 3.17 – 3.19: the solution outlet flow rate and both vapor flow rates. These three conservation equations, when solved simultaneously, determine these three variables.

For the 25th segment, the inlet and outlet solution temperatures were determined to be 127.6 ˚C and 128.7 ˚C, respectively. With these temperatures, and a system pressure of 2094 kPa and quality of 0, the solution inlet and outlet concentration and enthalpy can be determined from the ammonia-water property routines. At the inlet: h = 362 kJ kg^{-1}, x = 0.3445 ; at the outlet, h = 366 kJ kg^{-1}, x = 0.3402.

For the 25th segment, the closed model calculates the vapor-to-solution temperature inequality to be 9.25 ˚C. From this value, the vapor outlet temperature is determined to be 136.9 ˚C. For the 26th segment, the closed model calculates the temperature inequality to be 8.9 ˚C; from this value, the 25th segment vapor inlet temperature is calculated to be 137.6 ˚C. With the temperature, pressure and quality defined at these points, the concentration and enthalpy are

determined from the property relations. For the vapor at the inlet: h = 1681 kJ kg^{-1}, x = 0.875; at the outlet: h =1676 kJ kg^{-1}, x = 0.8782.

With the vapor and solution enthalpies and concentrations specified at the inlet and outlet of the 25th segment, Equations 3.17 – 3.19 can be solved to yield the three unknown flow rates. When the model is completely closed, the fourth flow rate – for the solution inlet – propagates down from the specified total solution flow rate into the first segment. For the 25th segment, the solution inlet flow rate is 0.008446 kg s^{-1}, and the conservation equations yield the remaining flow rates: Solution outlet: 0.008386 kg s^{-1}, vapor inlet: 0.001422 kg s^{-1}, vapor outlet: 0.001483 kg s^{-1}.

$$0.008446\ \frac{kg}{s} + \dot{m}_{Vapor\ In} = \dot{m}_{Solution\ Out} + \dot{m}_{Vapor\ Out}$$

$$0.008446\ \frac{kg}{s}(0.3445) + \dot{m}_{Vapor\ In}(0.875) = \dot{m}_{Solution\ Out}(0.3402) + \dot{m}_{Vapor\ Out}(0.8782)$$

$$0.008446\ \frac{kg}{s}\left(362\ \frac{kJ}{kg}\right) + \dot{m}_{Vapor\ In}\left(1676\ \frac{kJ}{kg}\right) + q_{Segment} = \dot{m}_{Solution\ Out}\left(366\ \frac{kJ}{kg}\right) + \dot{m}_{Vapor\ Out}\left(1681\frac{kJ}{kg}\right)$$

$$\dot{m}_{Solution\ Out} = 0.008386\ \frac{kg}{s};\quad \dot{m}_{Vapor\ In} = 0.001422\ \frac{kg}{s};\quad \dot{m}_{Vapor\ Out} = 0.001483\ \frac{kg}{s}$$

The vapor-to-solution temperature inequalities calculated from the closed model are presented in Figure 3.17; the calculations used to develop these values are examined in Section 3.5. With these temperature inequalities and the solution temperatures calculated previously (Figure 3.15), the vapor temperatures along the length of the component are easily determined from Equation 3.22. Figure 3.18 presents the vapor, solution, wall and coupling fluid temperatures along the length of the desorber.

With the vapor and solution temperatures defined throughout the model, the ammonia-water property routines can be used to determine the concentrations of these streams. Figure 3.19 presents a plot the vapor and solution concentrations along the length of the desorber. The property routines also determine enthalpies across the component for both streams, providing the final parameters to close the conservation relationships. These conservation relationships, presented as Equations 3.17 – 3.19, are solved to yield the vapor and solution flow rates, which are presented in Figure 3.20.

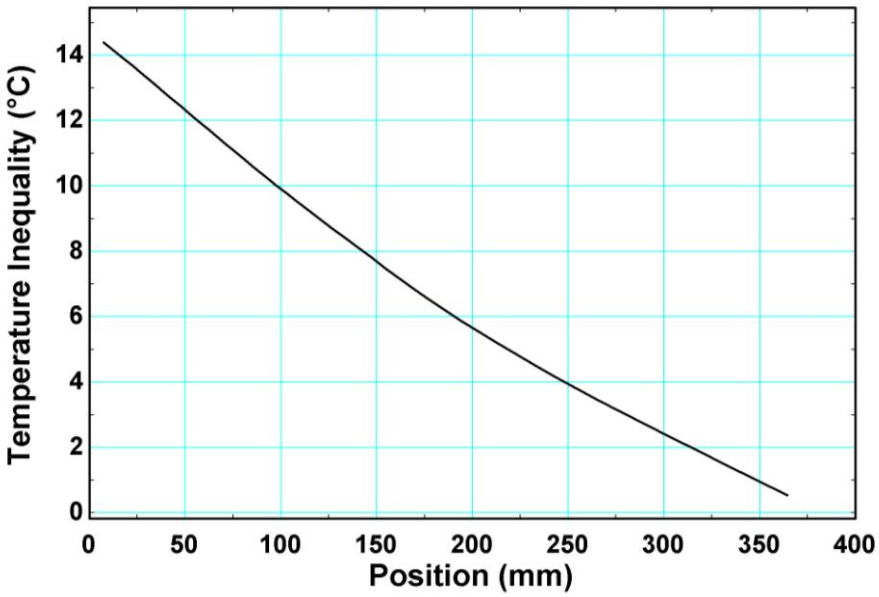

Figure 3.17: Vapor-to-Solution Temperature Inequality

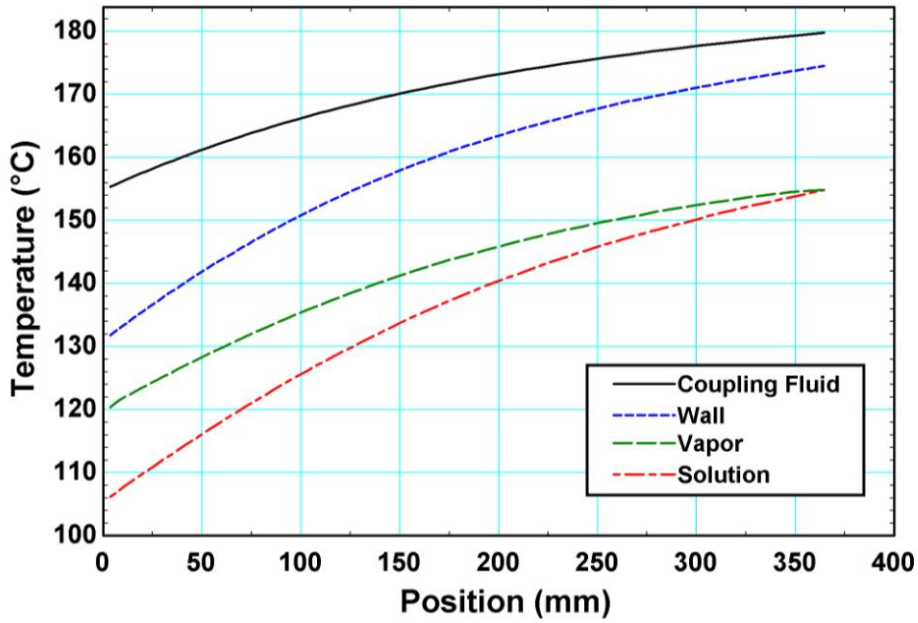

Figure 3.18: Vapor, Solution, Wall and Coupling Fluid Temperatures

At the bottom of the component, where the vapor mass flowrate is zero (Figure 3.19), the generated vapor and the solution are at the same temperature, the saturation temperature (Figure 3.18). As this vapor generated at the bottom of the desorber rises, it mixes with vapor generated at cooler, higher points in the component. Because of this cumulative effect, the rising vapor is at a higher temperature than the solution; this temperature difference causes heat and mass transfer between the two phases. The concentration gradient observed in Figure 3.20 also contributes to the interphase heat and mass transfer. This figure shows that the highest rates of change in the solution concentration are at the top of the component, where the boiling heat transfer coefficient and the heat flux are greatest.

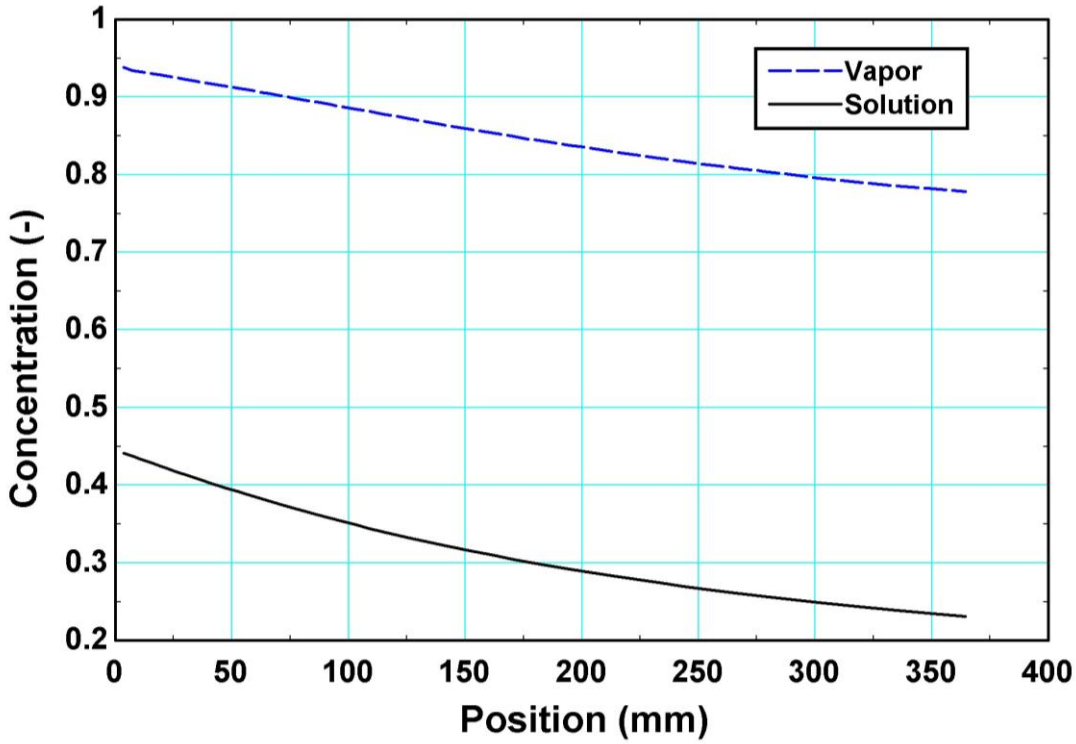

Figure 3.19: Vapor and Solution Concentrations

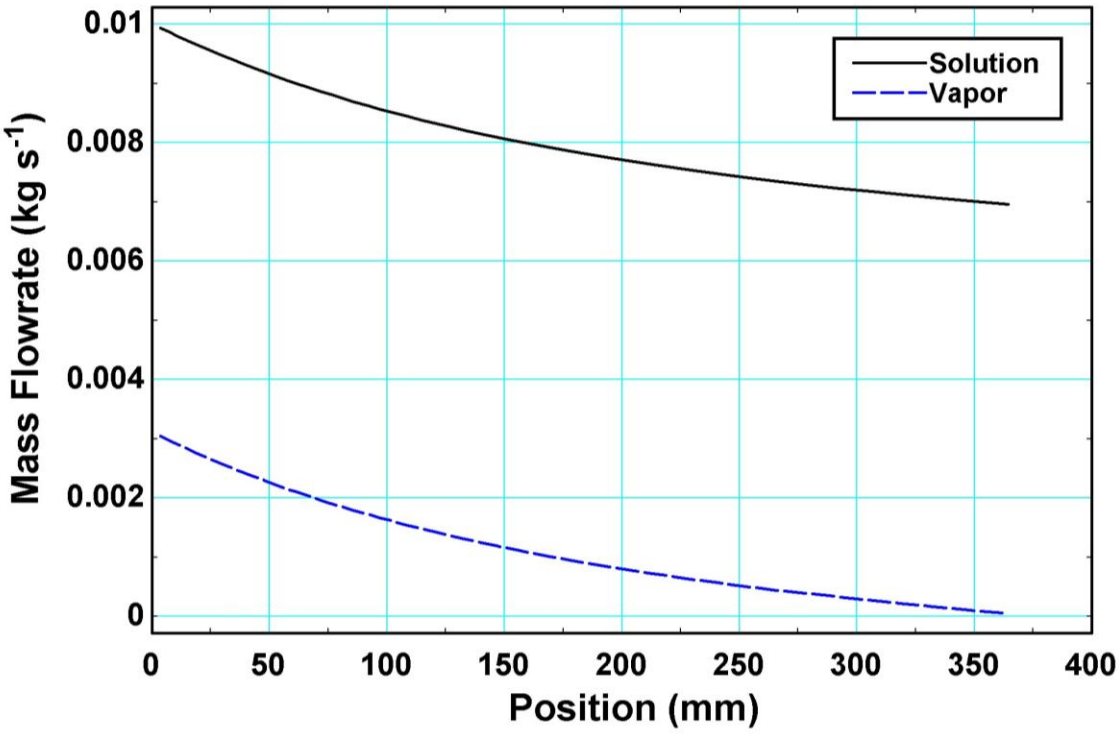

Figure 3.20: Vapor and Solution Flowrates

3.6 Vapor-to-Solution Heat and Mass Transfer

The temperature and concentration gradients between the vapor and solution cause heat and mass transfer between the two phases. A model was developed to address this interaction and is used to analyze the vapor-to-solution temperature inequalities presented in Figure 3.17. Two distinct driving forces lead to transport between the vapor and solution streams. First, because the solution temperature increases towards the bottom of the desorber, the rising vapor stream is surrounded by solution at a lower temperature. This temperature difference causes sensible cooling of the vapor stream, transferring heat back to the solution. Additionally, concentration gradients within the vapor stream lead to mass transfer that serves to refine the vapor stream.

Figure 3.21 presents a schematic representation of the vapor and solution streams in a segment. Within a given segment, three components of the vapor stream are present. First is the

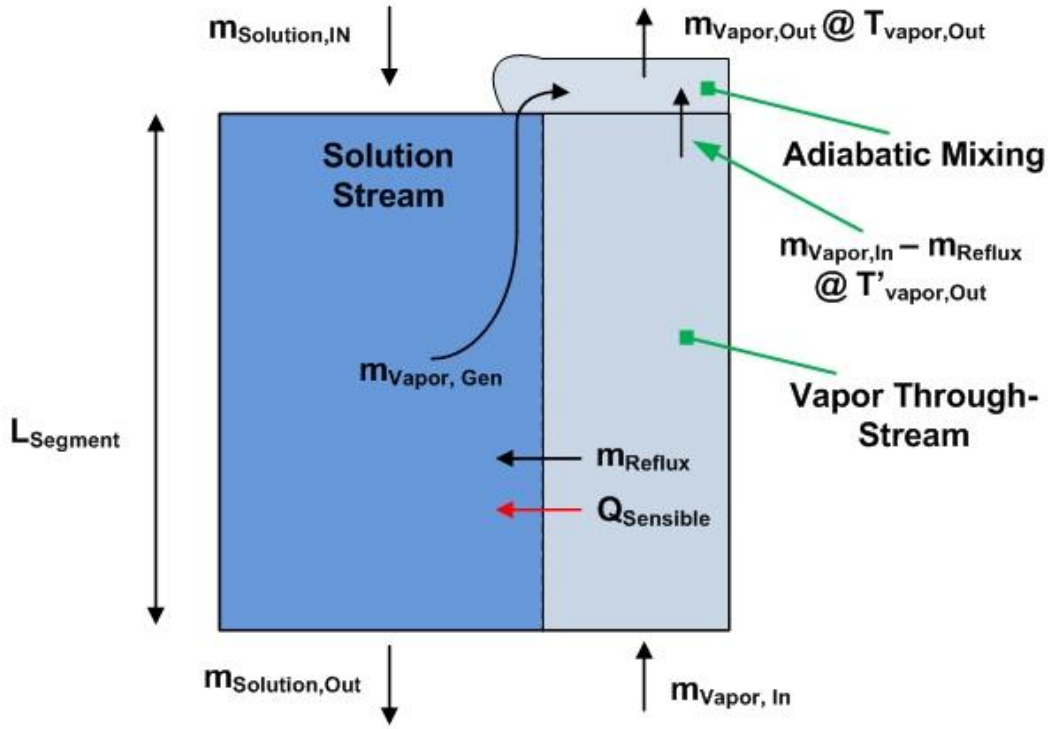

Figure 3.21: Vapor and Solution Interaction Schematic

vapor that flows into the segment from those beneath it, referred to as the through-stream. Because the vapor generated below a given segment is hotter than the solution in that segment, this through-stream is expected to exchange heat with the solution. At the bottom of the segment, the flowrate of the through-stream is equal to $\dot{m}_{\text{Vapor In}}$, but it is reduced by the reflux along the length of the segment.

Also present is the vapor generated within the segment. The vapor generated within a segment is assumed to be at the saturation temperature of the solution in that segment. Thus, there is little temperature difference between the vapor generated in a given segment, and the solution in that segment. This vapor stream is not expected to exchange heat with the solution, and is not included in the calculations of sensible heat transfer between the two phases. The generated vapor is shown to mix with the through-stream at the top of the segment, to form one vapor stream leaving the segment with a mass flowrate, $\dot{m}_{\text{Vapor Out}}$.

A third (condensing vapor) stream, resulting from concentration and temperature gradient-induced condensation, represents the reflux from the vapor to solution stream. This reflux reduces the flowrate of the vapor through-stream.

Equation 3.23 follows from the conservation of mass of the vapor streams within a segment:

$$\dot{m}_{\text{Vapor In}} + \dot{m}_{\text{Vapor } Gen} = \dot{m}_{\text{Vapor Out}} + \dot{m}_{\text{reflux}} \tag{3.22}$$

Two thermal pathways are present between the vapor and solution. First, because the through-stream and the solution are at different temperatures, they will undergo sensible heat transfer. This heat transfer is modeled as occurring between the average temperature of the solution and vapor through-streams, and employs an interfacial area term, A_{V-S} and vapor-to-

solution heat transfer coefficient, h_{V-S}, as shown in Equation 3.24. $T'_{VaporAve}$ is the average temperature of the vapor through-stream.

$$\begin{aligned} Q_{\text{Vapor-to-Solution, Sensible}} &= \left(h_{V-S}A_{V-S}\right)\left(T'_{VaporAve} - T_{Solution,Interface}\right) \\ T'_{VaporAve} &= \frac{1}{2}\left(T_{Vapor,In} + T'_{Vapor,Out}\right) \end{aligned} \tag{3.22}$$

A second thermal pathway represents the energy transferred from the vapor to solution by the condensing reflux. This latent heat is calculated from the reflux mass flowrate and the heat of vaporization of the condensate, as shown in Equation 3.25.

$$Q_{\text{Vapor-to-Solution, Latent}} = \dot{m}_{\text{reflux}}\left(h_{\text{fg,reflux}}\right) \tag{3.22}$$

The total heat transferred between the two phases is the sum of the sensible and latent components, as shown in Equation 3.26.

$$Q_{\text{Vapor-to-Solution, Total}} = Q_{\text{Vapor-to-Solution, Sensible}} + Q_{\text{Vapor-to-Solution, Latent}} \tag{3.22}$$

This total heat transferred between the vapor and solution phases can be included in a formulation of the conservation of energy for the vapor within a segment, as shown in Equation 3.27.

$$\dot{m}_{\text{Vapor In}}h_{\text{Vapor In}} + \dot{m}_{\text{Vapor Gen}}h_{\text{Vapor }Gen} = \dot{m}_{\text{Vapor Out}}h_{\text{Vapor Out}} + Q_{Vapor-to-Solution,\ Total} \tag{3.23}$$

Because the vapor generated within a segment is assumed to be at the saturation temperature of that segment, the enthalpy of the generated vapor stream, $h_{\text{Vapor,Gen}}$, is defined using the property routines at the segment saturation temperature and quality, q = 1. Additionally, the statepoint Vapor Out includes the contributions from both the through-stream and the generated vapor.

The condensation reflux flow rate, and the vapor-to-solution sensible heat transfer coefficient and interfacial area can be determined from heat and mass transfer analyses, to be discussed shortly. With these parameters determined, one additional relationship is required to close the model. At the outlet of the segment, the generated vapor and the through-stream are assumed to mix adiabatically. Equation 3.28 presents this relationship. The first term represents the through-stream vapor at the segment outlet: the inlet mass flow rate has been reduced by the reflux, and its enthalpy is determined from the outlet temperature of the through-vapor stream, $T'_{Vapor,Out}$ from the temperature difference in Equation 3.24.

$$\left(\dot{m}_{\text{Vapor In}} - \dot{m}_{\text{Reflux}}\right) h'_{\text{Vapor } Out} + \dot{m}_{\text{Vapor Gen}} h_{\text{Vapor } Gen} = \dot{m}_{\text{Vapor Out}} h_{\text{Vapor Out}} \qquad (3.24)$$

The remainder of the problem rests in the calculation of the condensing reflux flow rate, and the sensible vapor-to-solution heat transfer coefficient and interfacial area.

In order to determine the interfacial area, the average bubble diameter must be first determined. The correlation of Idogawa *et al.* (1987), as reported by Winterton (2004) is used, relating the Sauter mean diameter of the bubble to the surface tension, σ, system pressure, P, and vapor density, ρ_V, as shown in Equation 3.29 .

$$D_{Bubble} = \left(0.00391\right) \rho_v^{-0.07} \left(\frac{\sigma}{0.072}\right)^{0.22 \exp\left(P_{System,MPa}\right)} \qquad (3.25)$$

Using the average bubble diameter, the characteristic rise velocity can be determined by equating the buoyant and drag forces. Equation 3.30 presents this relationship for determining the rise velocity, U_{Bubble}. Here, the Schlichting (1955) drag coefficient around a sphere was used for C_d.

$$\left(\rho_l - \rho_v\right)\frac{4\pi}{3}\left(\frac{D_{Bubble}}{2}\right)^3 g = C_d \rho_l \left(U_{Bubble}\right)^2 \pi \left(\frac{D_{Bubble}}{2}\right)^2 (0.5) \tag{3.26}$$

Next, the number of bubbles within a segment must be determined. The void fraction is calculated for each segment from the average vapor and solution flow rates and velocities and the geometric parameters of the flooded column. Equations 3.31 – 3.33, when solved together, determine the void fraction within the channel.

$$\dot{m}_{Vapor,Ave} = \rho_v A_v U_{Bubble} \tag{3.27}$$

$$\dot{m}_{Solution,Ave} = \rho_L A_L U_{Solution} \tag{3.28}$$

$$A_{Total} = A_{Solution} + A_{Vapor} = Width \bullet Depth \bullet N_{Columns} \tag{3.29}$$

$$\frac{A_{Vapor}}{A_{Total}} = Void\ Fraction = \frac{V_{Vapor}}{V_{Total}} \tag{3.30}$$

With the void fraction and the volume occupied by vapor within a segment determined, the number of bubbles is easily found by dividing by their volume. With the bubble count, the total bubble surface area, which represents the vapor-to-solution interfacial area, is determined from Equation 3.35. Because the Sauter mean diameter provided by the Idogawa *et al.* (1987) correlation is the diameter of a sphere with a volume equivalent to that of the bubble, Equation 3.35 uses the surface area of a sphere.

$$A_{V-S} = N_{Bubbles}\left(4\pi\left(\frac{D_{Bubble}}{2}\right)^2\right) \tag{3.31}$$

For the 25th segment, the surface tension is 0.02624 N m^{-1}, the vapor density is 11.52 kg m^{-3} and the system pressure is 2094 kPa. With these values, Equation 3.29 yields a bubble diameter of 3.2 mm.

$$D_{Bubble} = (0.00391)(11.52)^{-0.07}\left(\frac{0.0262}{0.072}\right)^{0.22\exp(2.094)} \quad ; \quad D_{Bubble} = 3.2 \text{ mm}$$

With a bubble diameter of 3.2 mm, Equation 3.30 yields a bubble rise velocity of 0.3256 m s^{-1} (The solution density is 826.1 kg m^{-3}, and the drag coefficient is 0.39).

$$\left(826\frac{kg}{m^3} - 11.5\frac{kg}{m^3}\right)\frac{4\pi}{3}\left(\frac{0.0032m}{2}\right)^3 9.81\frac{m}{s^2} = (0.39)826\frac{kg}{m^3}(U_{Bubble})^2\,\pi\left(\frac{0.0032m}{2}\right)^2(0.5)$$

$$U_{Bubble} = 0.3256 \text{ m/s}$$

During flow visualization studies, the bubble rise velocity was observed to be approximately 0.20 m s^{-1}, in good agreement with this calculated value.

For the 25th segment, the average vapor and solution flow rates are 0.001452 kg s^{-1} and 0.008416 kg s^{-1}, respectively. The total cross-sectional area is calculated from the column width and depth, 108 mm and 6.3 mm, respectively, and the number of columns, $N_{Columns}$ = 5. With these parameters and the bubble rise velocity, Equations 3.31 – 3.34 yield a void fraction of 0.113 for this segment.

$$0.001452\ \frac{kg}{s} = 11.52\frac{kg}{m^3}A_v\left(0.325\frac{m}{s}\right); \quad A_v = 0.00038 \text{ m}^2$$

$$0.008416\ \frac{kg}{s} = \left(826\frac{kg}{m^3}\right)A_L U_{Solution}$$

$$A_{Total} = A_{Solution} + 0.00038m^2 = 108mm \bullet 6.3mm \bullet 5; \quad A_{Total} = 0.00343\text{m}^2; \quad A_{Solution} = 0.00304\text{m}^2$$

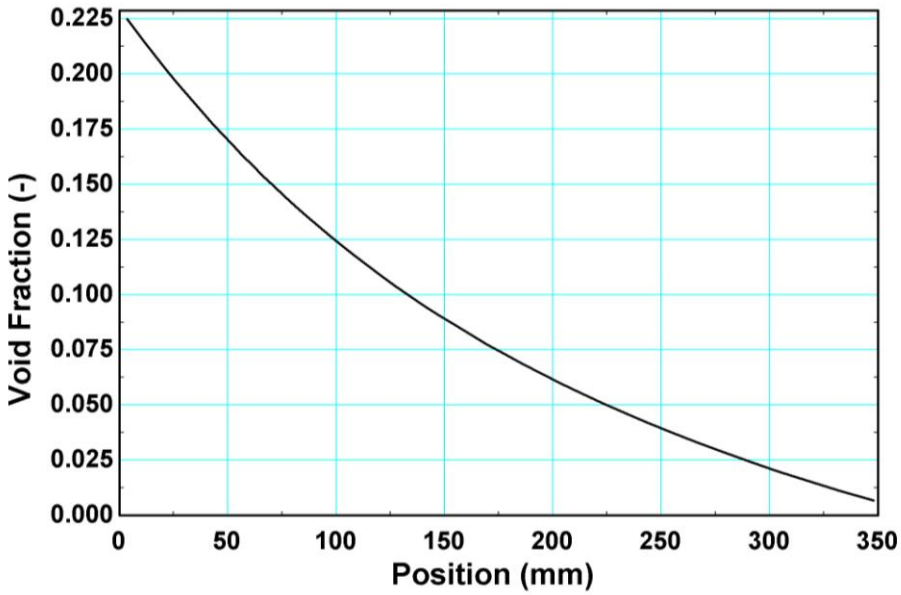

Figure 3.22: Void Fraction across Desorber Length

$$\frac{0.00038m^2}{0.00343m^2} = Void\ \ Fraction = 0.113$$

From the void fraction and the segment length, 5.97 mm, the vapor volume is calculated to be $2.315 \cdot 10^{-6}$ m^3. The average bubble volume is determined from the bubble diameter, and the number of bubbles in this segment is calculated to be 134. Equation 3.34 is used with this bubble count to determine the segment interfacial area, $A_{V\text{-}S} = 0.004332$ m^2.

$$A_{V-S} = 134\left(4\pi\left(\frac{3.2mm}{2}\right)^2\right) = 0.004311\ \text{m}^2$$

The average bubble diameter and rise velocity remain relatively constant throughout the length of the component, around 3.2 mm and 0.32 m s^{-1}, respectively. Figure 3.22 presents a plot of the void fraction across the length of the component: it is zero at the bottom segment, and reaches a value of 0.225 at the top of the component.

Having used an empirical correlation to determine the diameter of the bubbles within the vapor stream, and then calculating the vapor-to-solution interfacial area, the heat transfer coefficient between these two streams must now be determined. Kendoush (2007) reports a heat transfer correlation for rising spherical-cap bubbles as a function of the Peclet number. This correlation is presented as Equation 3.36.

$$\frac{h_{V-S} D_{Bubble}}{K_{Solution}} = 2.1138\sqrt{Peclet} = 2.1138\sqrt{\frac{D_{Bubble} U_{Bubble}}{\alpha_{Vapor}}} \qquad (3.32)$$

For the 25th segment, the solution thermal conductivity is 0.5299 W/m-K and the vapor thermal diffusivity is 0.00128 m^2/s. The vapor-to-solution heat transfer coefficient was calculated to 315.3 W/m^2K using Equation 3.36.

$$\frac{h_{V-S}\left(3.2mm\right)}{0.53\,{}^{W}\!/_{m\text{-}K}} = 2.1138\sqrt{Peclet} = 2.1138\sqrt{\frac{3.2\text{ mm}\left(0.325\text{ m/s}\right)}{1.28\text{ mm/s}}}; \quad h_{V-S} = 315\ \frac{W}{m^2K}$$

The vapor-to-solution heat transfer coefficient remains close to this value along the length of the desorber.

Having considered the bubble hydrodynamics and heat transfer, the mass transfer process must be examined. The mass transfer from the vapor to the reflux solution stream can be treated as the condensation of a binary mixture, and the Colburn and Drew (1937) method has been used to characterize this process (Hewitt *et al.*, 1993). This analysis starts by assuming the solution to be well mixed: the bulk solution concentration and temperature are equal to the interface values. The solution side thus specifies the interface temperature. The vapor interface concentration is determined at this interface temperature and a quality of 1 using the ammonia-water property functions. The Colburn-Drew method then defines the condensing molar flux, $\dot{n}_{Total}$, using the concentration gradient between the vapor interface and bulk, as shown in Equation 3.29. The

molar concentration of the condensing flux, $\tilde{z}$, is also determined when the model is completely closed. C_t is the total molar concentration and β_{Vapor} is the mass transfer coefficient.

$$\dot{n}_{Total} = \beta_{Vapor} C_t \ln\left(\frac{\tilde{z} - \tilde{x}_{v,interface}}{\tilde{z} - \tilde{x}_{v,bulk}}\right)$$
$$C_t = \frac{p}{RT} \tag{3.33}$$

Equation 3.29 is written in molar terms: the mass-based concentrations and flow rates must be converted to a molar basis, as shown in Equations 3.31 – 3.32.

$$\tilde{x}_{Vapor} = x_{Vapor} \frac{M_{Vapor}}{M_a}$$
$$M_{Vapor} = \left(\frac{x_{Vapor}}{M_a} + \frac{\left(1 - x_{Vapor}\right)}{M_w}\right)^{-1} \tag{3.34}$$

$$\tilde{x}_{Solution} = x_{Solution} \frac{M_{Solution}}{M_a}$$
$$M_{Solution} = \left(\frac{x_{Solution}}{M_a} + \frac{\left(1 - x_{Solution}\right)}{M_w}\right)^{-1} \tag{3.35}$$

The mass transfer coefficient, β_{Vapor}, is determined by using the heat and mass transfer analogy based on the vapor-to-solution heat transfer coefficient. The mass transfer form of the correlation for spherical-cap bubbles, as reported by Kendoush (2007) is shown as Equation 3.32, where the Sherwood number is a function of the Peclet number. The Peclet number is a function of the bubble diameter and rise velocity, and the vapor thermal diffusivity. The mass diffusivity, $D_{NH_3\text{-}H_2O}$, is determined for the ammonia-water vapor from the Chapman-Enskog kinetic theory of gases, as shown in Equation 3.33, where σ_{A-W} is the average collision diameter,

Ω is the temperature-dependent collision integral, and P is the system pressure (Chapman and Cowling, 1970).

$$Sh = 2.133\left(Peclet\right)^{0.5}$$

$$\text{Where} \quad \beta_{\text{Vapor}} = \frac{\text{Sh} \bullet \text{D}_{\text{NH}_3\text{-H}_2\text{O}}}{D_{bubble}} \qquad (3.36)$$

$$\text{and} \qquad \text{Peclet} = \frac{\text{D}_{\text{Bubble}}\text{U}_{\text{Bubble}}}{\alpha_{Vapor}}$$

$$\text{D}_{\text{NH}_3\text{-H}_2\text{O}} = 1.86\times10^{-7}\,\frac{T^3\sqrt{1/M_A + 1/M_W}}{\sigma_{A-W}\Omega P} \qquad (3.37)$$

After using Equation 3.37 to determine the total condensing flux, the condensate concentration, $\tilde{z}$ can be used to determine the condensing flux of both species, as shown in Equation 3.42.

$$\begin{aligned} \dot{\text{n}}_{\text{NH}_3} &= \dot{\text{n}}_{\text{Total}}\ \tilde{\text{z}} \qquad \textit{and} \\ \dot{\text{n}}_{\text{H}_2O} &= \dot{\text{n}}_{\text{Total}}\ \left(1\text{-}\,\tilde{\text{z}}\right) \end{aligned} \qquad (3.38)$$

Finally, Equation 3.43 can be used to calculate the reflux mass flow rate from the molar species mass fluxes.

$$\dot{m}_{reflux} = \dot{\text{m}}_{\text{cond,NH}_3} + \dot{\text{m}}_{\text{cond,H}_2O} = \left(\text{M}_{\text{H}_2O}\dot{\text{n}}_{\text{H}_2O} + \text{M}_{\text{NH}_3}\dot{\text{n}}_{\text{NH}_3}\right)\text{A}_{\text{Interface}} \qquad (3.39)$$

For the 25th segment, the interface temperature, which is equal to the bulk solution temperature, is 128.1 ˚C. At this temperature, the interface vapor concentration is determined from the ammonia-water property routines to be $x_{VaporInterface} = 0.9117$, or $\tilde{x}_{VaporInterface} = 0.9161$ on a molar basis. The bulk vapor concentration is $x_{VaporBulk} = 0.876$, or on a molar basis, $\tilde{x}_{VaporBulk} = 0.8826$. The Chapmon-Enskog kinetic theory of gases is used to determine the mass

diffusivity for the ammonia-water vapor to be 2.443 x 10^{-6} m/s, and Equation 3.40 yields a Sherwood number of 1.908. From Equation 3.40, the mass transfer coefficient, β_{Vapor}, is 0.001453 m/s. The mass transfer coefficient remains constant near this value along the length of the desorber.

$$\frac{\beta_{V-S}\left(3.2mm\right)}{2.443 \text{ x } 10^{-6}} = 2.1138\sqrt{Peclet} = 2.1138\sqrt{\frac{3.2mm\left(0.325\text{m/s}\right)}{0.00128\ m/s}}; \quad \beta_{V-S} = 0.001455\frac{m}{s}$$

Additionally, the molar concentration of the condensing flux for this segment is $\tilde{z} = 0.7507$ and C_t = 0.6137. With these values, Equation 3.37 yields a total molar condensing mass flux of $\dot{n}_{Total} = 0.0002023 \text{ mol m}^{-2}\text{s}^{-1}$.

$$\dot{\text{n}}_{\text{Total}} = \left(0.001455\right)\left(0.6137\right)\ln\left(\frac{0.7507\text{- }0.9161}{0.7507\text{ - }0.867}\right) = 0.0002023\frac{mol}{m^2 s}$$

Applying Equations 3.42 and 3.43, the total reflux mass flow rate for this segment is calculated to be $\dot{m}_{\text{Reflux}} = 0.00001514 \text{ kg s}^{-1}$.

$$\dot{\text{n}}_{\text{NH}_3} = 0.0002023\ \left(0.7507\right) \quad = \left(0.0001519\frac{mol}{m^2 s}\right)$$

$$\dot{\text{n}}_{\text{H}_2O} = 0.0002023\ \left(1\text{ - }0.7507\right) \quad = \left(0.00005042\frac{mol}{m^2 s}\right)$$

$$\dot{m}_{reflux} = \left(18.02\frac{kg}{mol}\left(0.00005042\frac{mol}{m^2 s}\right) + 17.03\frac{kg}{mol}\left(0.0001519\frac{mol}{m^2 s}\right)\right)0.004332\text{m}^2$$

$$\dot{m}_{reflux} = 0.00001514\ kg/s$$

Figure 3.23 presents a plot of the vapor concentrations at the bulk and interface, and the concentration of the condensing stream across the component. The condensate is, at all points, at a lower concentration than the vapor at both the interface and bulk. All three concentrations tend

to increase toward the top of the component, where the solution and vapor concentrations are the highest (Figure 3.19)

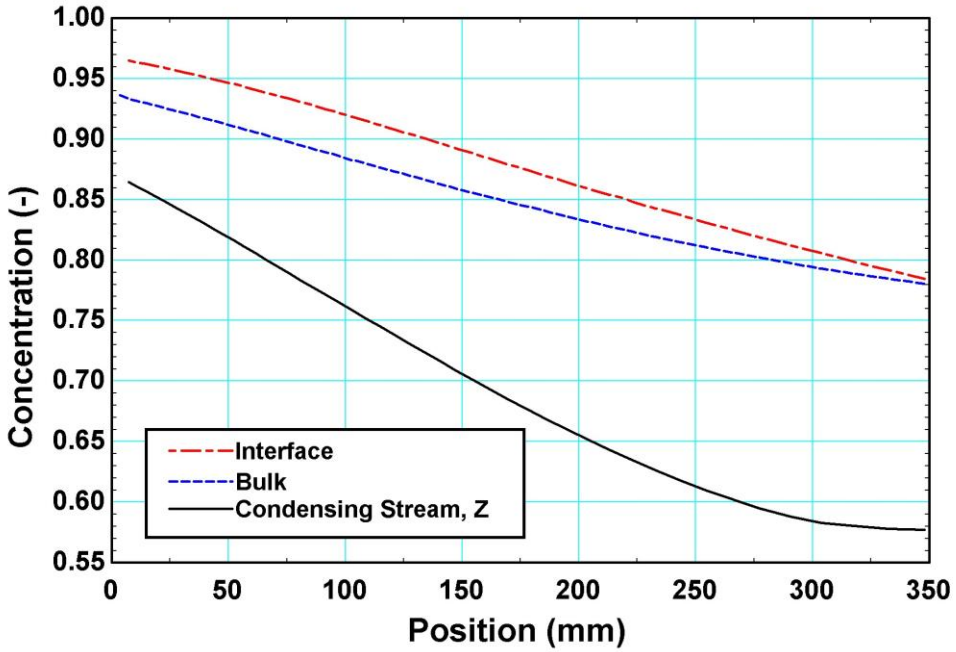

Figure 3.23: Interface, Bulk and Condensate Vapor Concentrations (Mass Basis)

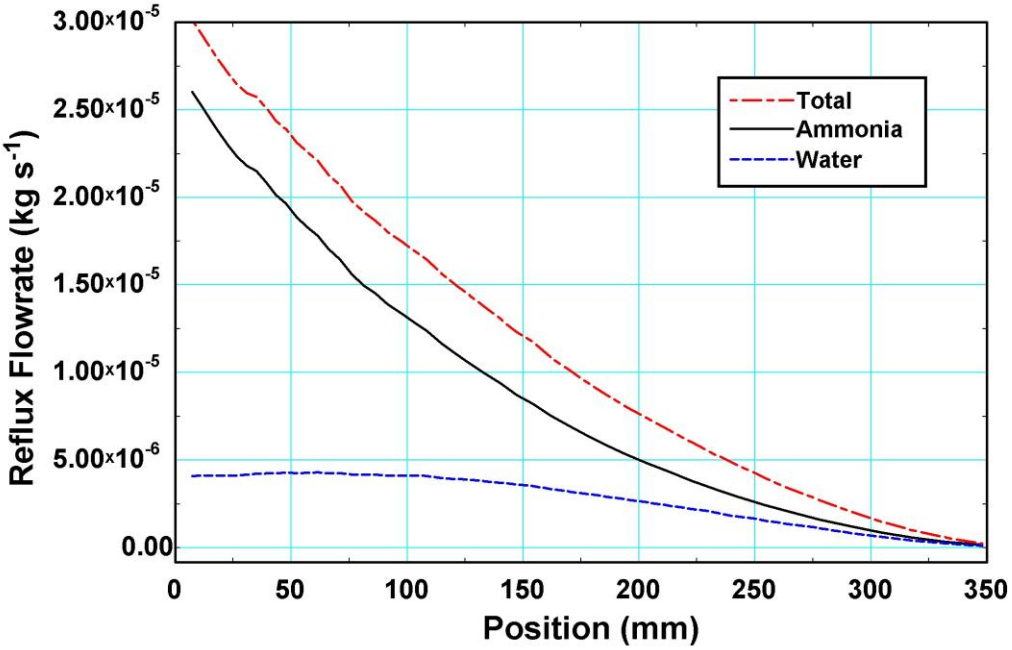

Figure 3. 24: Total and Species Condensation Flowrates

Figure 3.24 presents a plot of the total and species condensate mass flow rates along the length of the component. The reflux flow rate is highest at the top of the component, where the temperature gradient between the solution and vapor is the largest (Figure 18). At the top of the component, ammonia preferentially condenses from the vapor stream, while the condensation of water stays at a constant rate. This is explained by understanding that the vapor stream is increasingly ammonia-rich at the top of the desorber. The irregularities observed in the condensation flowrates at the top of the component are attributed to round-off errors from the computations; this noise is present because the condensation flowrates are comparatively small. Comparison of Figure 3.24 and Figure 3.20 shows that the condensation flowrates are two orders of magnitude smaller than the total vapor flowrates.

Having determined the concentration and flow rate of the concentration-gradient-induced condensation process, and the sensible heat transfer coefficient and interfacial area between the vapor and solution streams, the vapor stream conservation equations presented as Equations 3.23-3.28 can be closed. For the 25th segment, the mass balance on the vapor stream, Equation 3.23, yields a generated vapor flow rate of 7.53×10^{-5} kg s^{-1}. The inlet and outlet vapor flow rates are 0.001422 kg s^{-1} and 0.001483 kg s^{-1}, respectively.

$$0.001422\frac{kg}{s} + \dot{m}_{\text{Vapor } Gen} = 0.001483\ \frac{kg}{s} + 0.00001514\ \frac{kg}{s}; \quad \dot{m}_{\text{Vapor } Gen} = 7.53 \text{ x } 10^{-5} \text{kg/s}$$

The energy balance on the vapor stream, Equation 3.27, can be completed by assuming the outlet temperature – this temperature will be confirmed by closing the model. The closed model yields a vapor outlet temperature of 136.9 ˚C, with a corresponding enthalpy of 1676 kJ kg^{-1}, Equation 3.27 yields a total heat transfer rate from the vapor to solution stream of 28.6 W.

The vapor enthalpies at the inlet and generation points are 1681 kJ kg^{-1} and 1617 kJ kg^{-1}, respectively.

$$\left(0.001422\,\frac{kg}{s}\right)\left(1681\ \frac{\text{kJ}}{kg}\right)+\left(7.53\ \text{x}\ 10^{-5}\,\frac{\text{kg}}{s}\right)\left(1617\ \frac{\text{kJ}}{kg}\right)=$$
$$\left(0.001483\ \frac{kg}{s}\right)\left(1676\ \frac{\text{kJ}}{kg}\right)+Q_{V-to-S,\ Total}$$

$$Q_{V-to-S,\ Total}=29.4\ \text{W}$$

As shown in Equation 3.26, the total heat transferred from the vapor to solution stream is the sum of latent and sensible components. The latent component is calculated from the reflux flowrate and the heat of vaporization of the condensate, as shown in Equation 3.25. For the 25th segment, the condensate has a concentration of $z=0.7401$. The mixture heat of vaporization is calculated from that of the pure components in proportion to this concentration; $h_{FG,Mixture}=1089$ kJ kg^{-1}. Equation 3.25 calculates the latent heat accompanying the condensing reflux to be 16.49 W:

$$\text{Q}_{\text{Vapor-to-Solution, Latent}}=0.00001514\,{kg}/{s}\left(1089\,\frac{kJ}{kg}\right);\quad \text{Q}_{\text{Vapor-to-Solution, Latent}}=16.93\ \text{W}$$

Subtracting the latent component from the total heat transferred, the sensible component must be 12.5 W. Equation 3.24 calculates this sensible heat transfer term from the heat transfer coefficient, interfacial area and temperature difference between the solution and the through-vapor stream. It should be noted that the through-vapor stream does not include the vapor generated within the segment, which does not participate in heat transfer with the solution. For the 25th segment, $h_{V-S}=315$ W $m^{-2}K^{-1}$ and $\text{A}_{\text{V-S}}=0.004311\ \text{m}^2$. With $\text{T}_{\text{Solution,Interface}}=128.3$

˚C and $T_{Vapor\ In}$ = 137.6 ˚C, Equation 3.24 yields an outlet temperature of the through vapor stream of $T'_{Vapor,Out} = 137.5$ ˚C.

$$12.5\ \text{W} = \left(315 \frac{W}{m^2 K} \bullet 0.004311 m^2 \right) \left(T'_{VaporAve} - 128.3 \right); \quad T'_{VaporAve} = 137.55\ ^{\circ}\text{C}$$

$$T'_{VaporAve} = \frac{1}{2}\left(137.6 + T'_{Vapor,Out} \right); \quad T'_{Vapor,Out} = 137.5\ ^{\circ}\text{C}$$

With the outlet temperature of the through-vapor stream determined, Equation 3.28 can be applied to determine the enthalpy of the total vapor outlet stream. The adiabatic mixing equation recombines the through-vapor and generated vapor streams at the segment outlet. The outlet enthalpy of the through-vapor stream is calculated from $T'_{Vapor\ Out}$; $h'_{Vapor\ Out} = 1680\ \text{kJ kg}^{-1}$.

Equation 3.28 yields the total outlet enthalpy of $h_{Vapor\ Out} = 1676\ \text{kJ kg}^{-1}$, corresponding to a temperature of $T_{Vapor\ Out} = 136.9\ ^{\circ}\text{C}$. This is the outlet vapor temperature calculated from the closed model, and for the purpose of illustrating the calculations, was specified as an input value earlier in Section 3.4. From Equation 3.28:

$$\left(0.001422 - 0.00001564\right)1680 + 0.0000758\left(1617\right) = \left(0.001483\right) h_{Vapor,Out}; \quad h_{Vapor,Out} = 1676 \frac{\text{kJ}}{\text{kg}}$$

From this vapor outlet temperature, the vapor-to-solution temperature inequality is calculated using Equation 3.22 to be $\Delta_{Inequality} = 9.25^{\circ}\text{C}$, as specified in the previous discussion.

These calculations were conducted for all segments; the vapor-to-solution temperature inequality along the length of the component is reported in Figure 3.17.

3.7 Summary of Heat and Mass Transfer Modeling

The principles of coupled heat and mass transfer were employed as discussed above to model the performance of a Flooded Column desorber for a 3.5 kW ammonia-water absorption system. Table 3.2 presents the outlet conditions and other salient parameters calculated from the heat and mass transfer model.

Table 3.2: Flooded Column Desorber Model Outputs

Heating Input		5.44 kW	Column Length		364 mm
Coupling Fluid Inlet			Coupling Fluid Outlet		
	Temperature	180 °C		Temperature	155.1 °C
	Flowrate	0.084 kg/s		Flowrate	0.084 kg/s
Concentrated Solution Inlet			Dilute Solution Outlet		
	Temperature	105.7 °C		Temperature	155.3 °C
	Concentration	0.4767		Concentration	0.23
	Flowrate	0.010 kg/s		Flowrate	0.069 kg/s
			Vapor Outlet		
				Temperature	119.6 °C
				Concentration	0.938
				Flowrate	0.0305 kg/s

CHAPTER 4: EXPERIMENTAL APPARATUS AND PROCEDURE

4.1 Experimental Apparatus

To investigate the component-level performance of a counterflow desorber, a facility was developed to conduct heat transfer and flow visualization experiments at operational temperatures and pressures. These experiments are necessary to validate the component modeling and design methodology by experimentally confirming not only the thermal performance of the desorber, but also the two-phase flow patterns and heat transfer processes actually occurring within the component. Preliminary component level flow visualization efforts were previously conducted, but were limited to near-atmospheric pressures and room temperatures. However, absorption systems operate routinely at over 1400 kPa, with maximum temperatures approaching 180°C. While surrogate fluids were chosen to replicate the thermophysical properties of ammonia and water at typical desorber conditions, these substitutions limit the utility of these investigations.

4.1.1 Facility Overview

The present test facility was designed to conducted flow visualization experiments at the operational conditions of a desorber in a typical absorption cycle, and is rated to pressures up to 2000 kPa and temperatures of 200°C.

The facility includes two of the most important components in an absorption cycle, the absorber and desorber. The desorber is installed within a pressure vessel equipped with large sight glasses for camera access and illumination necessary for flow visualization studies. Heat is

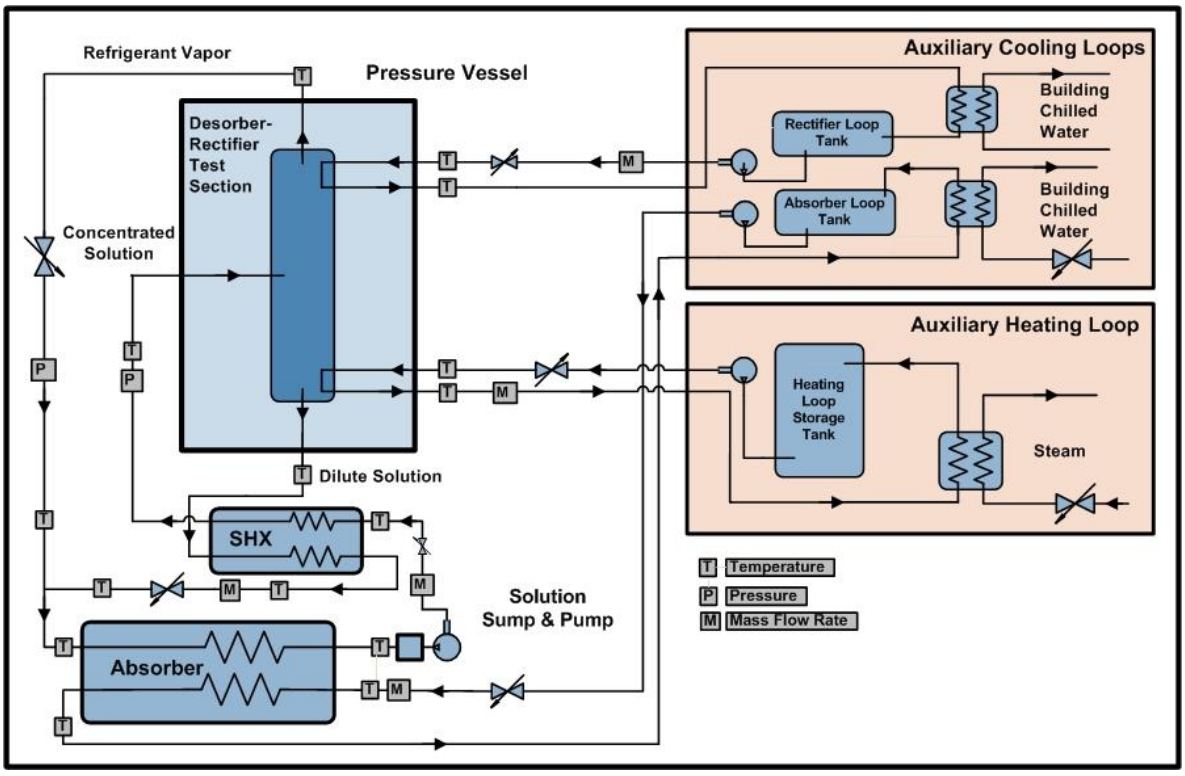

Figure 4.1: Flow Visualization Test Facility Schematic

supplied to the desorber by a steam-heated coupling fluid, Paratherm NF, which generates refrigerant vapor from the concentrated solution.

Dilute solution drains from the desorber and flows through a recuperative heat exchanger and an expansion device before entering the absorber. The refrigerant vapor generated in the desorber flows through an expansion device and enters the absorber, where it is absorbed back into the dilute solution. Concentrated solution leaving the absorber enters a sump before flowing to the solution pump, which sends the solution through the recuperative solution heat exchanger and to the desorber.

Coupling fluid loops convey heat into and out of the solution loop. The desorber is heated by a steam-heated Paratherm coupling fluid loop, while the absorber rejects heat to a chilled water coupling fluid loop, which is cooled by the building's chilled water. The facility also

includes a second chilled water coupling fluid loop to cool a rectifier, although this is not used in this investigation.

A schematic and photograph of the test facility are presented in Figures 4.1 and 4.2.

Figure 4.2: Flow Visualization Facility

4.1.2 Desorber Test Section

The Flooded Column desorber test section generates refrigerant vapor from the concentrated solution when heated by a high-temperature coupling fluid. It is housed within a pressure vessel with visual access to allow for determination of local flow phenomena. The test section consists of the flooded column itself and a microchannel heating unit welded to the flooded column. The heating unit is composed of a stainless steel plate that has been chemically

etched with features that, when stacked between the flooded column and a rear plate, forms an array of parallel micro-scale fluid passages that carry the high temperature Paratherm coupling fluid. Figure 4.3 shows a rendering of this etched microchannel shim. The flooded column is instrumented with 8 T-Type thermocouples to determine the solution temperature profile.

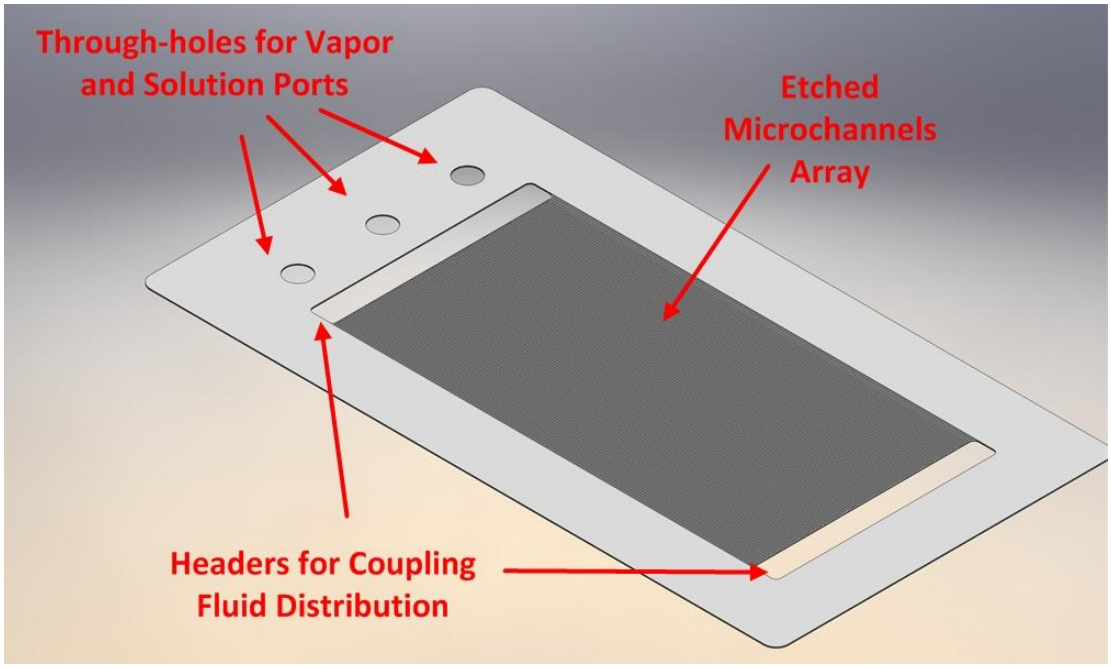

Figure 4.3: Etched Microchannel Shim

Figure 4.4 presents an image of the flooded column test section, and Table 4.1 provides the geometric specifications of the component. The dimensions of the Flooded Column were determined using the heat and mass transfer modeling process detailed in Chapter 3, scaled to a heat duty of 0.5 kW.

Table 4.1: Flooded Column Test Section Dimensions

Flooded Column		Heating Unit	
Depth	6.4 mm	Channel Diameter	0.76 mm
Width	114.3 mm	Number of Channels	90
Heated Legnth	219.7 mm		

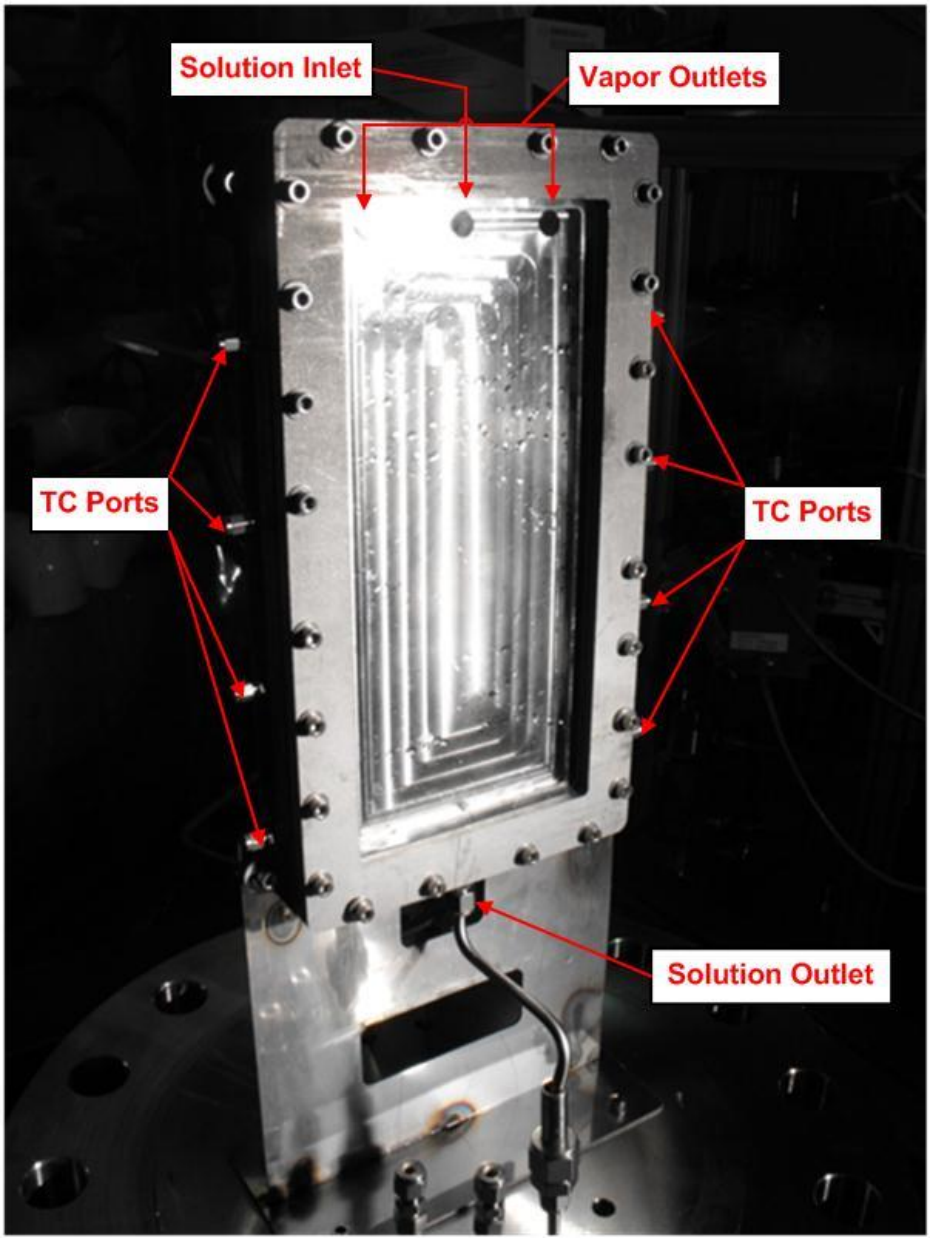

Figure 4.4: Flooded Column Test Section

4.1.3 Solution Loop and Auxiliary Heat Exchangers

FlatPlate™ brazed-plate heat exchangers serve as the absorber and solution heat exchanger in the solution loop, and as conditioning heat exchangers in the rectifier and absorber coupling fluid loops. An American Industrial shell-and-tube heat exchanger is used to couple high pressure steam to the desorber heating coupling fluid. Figures 4.5 and 4.6 show photos of these heat exchangers, and their specifications are summarized in Table 4.2.

Figure 4.5: Solution Heat Exchanger and Absorber CF Heat Exchanger (Left) and Absorber (Right)

Table 4.2: Heat Exchanger Specifications

	Solution Loop			Conditioning Loops	
	SHX	Absorber		Absorber CF	Paratherm CF
Manufacturer	FlatPlate	FlatPlate		FlatPlate	American Intustrial
Model	FPN 3x8-10	FPN 3x8-12		FPN 3x8-12	URCS-830
Volume, Side A	0.113 L	0.142 L		0.142 L	
Volume, Side B	0.142 L	0.170 L		0.170 L	
Max Pressure	2068 kPa	2068 kPa		2068 kPa	1034 / 2068 kPa
Max Temperature	175°C	175°C		175°C	230°C

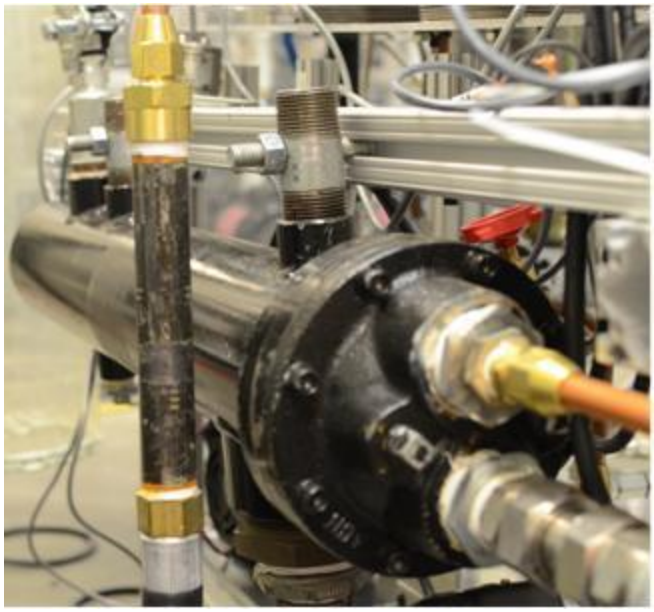

Figure 4.6: Paratherm Heating Steam Heat Exchanger

4.1.4 Pumps

A variable speed Tuthill gear pump is used in the solution loop, and Laing centrifugal pumps are used to circulate water through the rectifier and absorber coolant loops. A high-temperature Tuthill gear pump is used to circulate the desorber coupling fluid. Figures 4.7 and 4.8 present photos of these pumps, and their specifications are summarized in Table 4.3.

Table 4.3: Pump Specifications

	Solution Pump	Paratherm Pump	Absorber CF Pump
Manufacturer	Tuthill	Tuthill	Laing
Model	DGS - 0.38	0LE	SM-1212-26
Type	External Gear	Internal Gear	Centrifugal
Coupling	Magnetically Coupled	Close Coupled	
Flowrate	315 mL / min @ 1725 kPa	6.05 L / min @ 345 kPa	
Δ Pressure	1725 kPa	3450 kPa	1035 kPa
Max Temperature	175°C	245°C	110°C

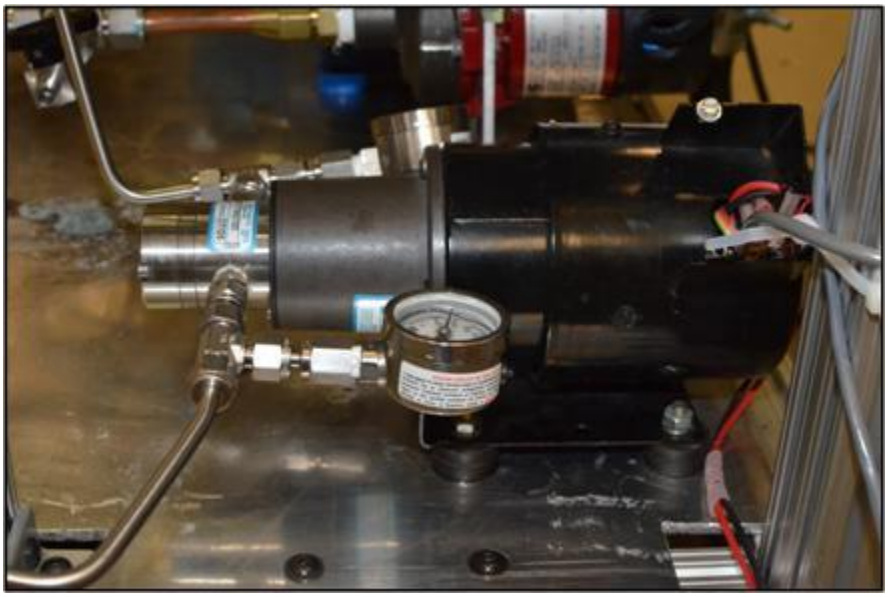

Figure 4.7: Tuthill D-Series Solution Pump

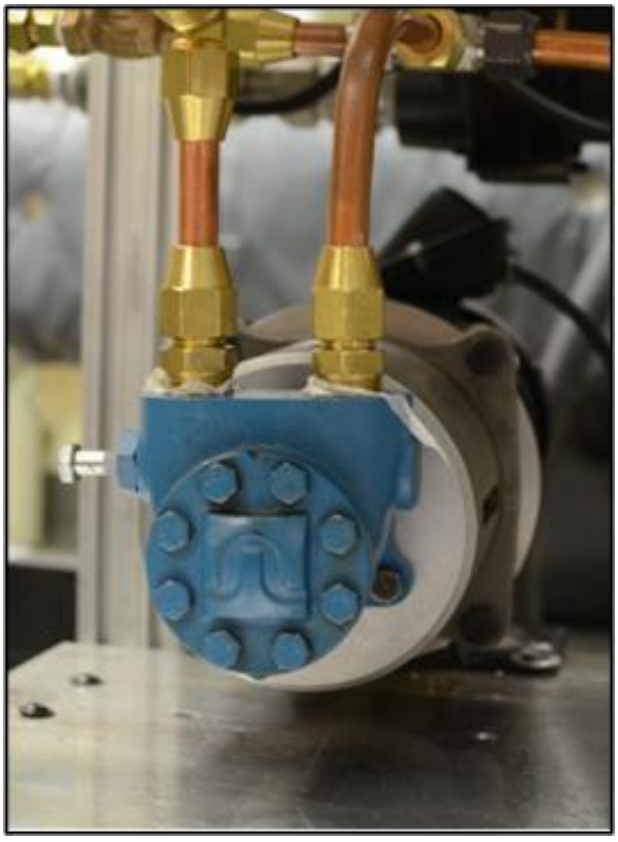

Figure 4.8: Tuthill L Series Paratherm Pump

4.1.5 Data Acquisition

Type-T thermocouples are used throughout the system to provide temperature measurements, and Wika pressure transducers are used to measure the system high-side and low-side pressures. The concentrated solution flow rate from the pump is measured with a Rheonik low-flow Coriolis meter, while positive displacement flow meters from DEA Engineering are used in the dilute solution and absorber coupling fluid lines. The desorber coupling fluid loop is measured with an AW Lake high-temperature gear flow meter. Thermocouple, pressure transducer and flow meter outputs are recorded using a National Instruments SCXI Data Acquisition system. The measurements are communicated to a personal computer via USB and are integrated into a LabVIEW virtual instrument for real-time control, display and documentation. Table 4.4 summarizes the specifications of the instruments and data acquisition system.

The flow visualization studies were conducted with a Nikon D7000 digital SLR camera using a 35 mm 1.8/f lens. Flow phenomena within the flooded column were recorded in 1080p High-Definition video at a frame rate of 24 frames per second.

Table 4.4: Data Acquisition System Specifications

	Flowmeters	
Manufacturer	DEA	DEA
Model	FMTD - 4	FMTD - 20
Range	1 to 250 mL/min	5 to 1250 mL/min
Accuracy	± 0.5%	± 0.5%

Thermocouples	Pressure Sensors
Omega	Wika
TMQ-SS	A-10
-270 to 400°C	0 to 3450 kPa
± 0.5%	± 1% of Range

Manufacturer	Rheonik
Model	RHM 015
Range	0 to $1.0 \cdot 10^{-3}$ kg/s
Accuracy	± 0.15%

Data Acquisition System	
Chassis	SCXI 1000
Modules	SCXI 1102, 1126
Terminals	SCXI 1303, 1320

4.2 Experimental Procedures

Heat and mass transfer experiments and flow visualization studies were conducted on the flooded column desorber for a wide range of parameters. The basic operating procedures followed are presented here.

4.2.1 Facility Preparation

After fabrication, and every subsequent modification, the facility was pressure checked. Large leaks were identified by spraying the plumbing with a leak-detection spray and charging the facility with low-pressure compressed air. Smaller leaks were identified by charging the system with R-134a and examining the facility with a refrigerant detection wand (Yellow Jacket AccuProbe, # 69365). After addressing all identified leaks, the system was charged with compressed nitrogen to the rated system pressure, 2000 kPa. The system was considered leak-free if it maintained this pressure overnight.

After ensuring the pressure integrity of the system, the facility was charged with water and ammonia. To charge the facility, the system was first evacuated using a vacuum pump. A specified amount of water, followed by the required amount of ammonia, was charged into the sump upstream of the solution pump. The experiments in this study were conducted at conditions with the same overall ammonia-water concentration in the entire test facility; the initial charge consisted of approximately 60% water and 40% ammonia.

4.2.2 Facility Operation and Data Collection Procedures

The experimental facility was designed to evaluate the desorber at conditions characteristic of a complete single–stage absorption cycle. Operating at pressures and

temperatures representative of the full cycle is necessary to validate the design. The facility allows direct control of several parameters characterizing the operating state point, while other parameters are controlled indirectly. Manipulation of the controlled parameters, both directly and indirectly, allows for the evaluation of the desorber across a range of operating conditions.

The concentrated solution flow rate into the desorber is controlled directly; the solution pump is equipped with a DC speed control allowing for fine flow rate adjustments. Similarly, the flow rate of the Paratherm coupling fluid, used to heat the desorber, is directly controlled by a variable speed DC motor. The Paratherm temperature at the desorber inlet is controlled by regulating the steam pressure. The operating pressure in the desorber is indirectly controlled, and is influenced by a combination of the Paratherm flow rate and temperature, absorber coupling fluid flow rate and temperature, and the solution flow rate. Similarly, the dilute solution flow rate, and thereby the solution level within the component, is indirectly controlled. The solution level is a function of the pressure gradient between the inside of the flooded column and the pressure vessel; this pressure gradient is a function of nearly every variable parameter, including the Paratherm temperature and flow rate, solution flow rate, system pressure and refrigerant and dilute solution valve settings.

When starting up the facility, concentrated solution was transferred from the sump to the flooded column test section using the solution pump. With the test section flooded, the steam line was opened and the Paratherm pump was started to circulate the heated coupling fluid to the desorber. Upon heating, the solution in the test section began to boil; this boiling establishes the required pressure gradient between the desorber and absorber, and drives the dilute solution from the pressure chamber back to the solution pump. The large thermal mass of the pressure vessel, and the interdependent nature of the indirectly controlled parameters, required careful monitoring

and control of the system during this startup period. After the system reached a steady state, the directly controlled parameters were manipulated to achieve the required operating point.

Flow visualization studies were conducted during steady-state operation of the facility, but were also used to document the transient instabilities in the flooded column. Heat and mass transfer data were collected only during steady state operation. When operating stably at the required data point, the temperatures, pressures and flow rates from the data acquisition system were recorded and averaged over a 2 minute period.

The flooded column desorber operated most stably in a partially flooded condition, where a pool-boiling regime occupied the lower portion of the desorber, under a segment of the desorber marked by falling-film heat transfer. Figure 4.9 presents an image of the desorber in the partially flooded condition.

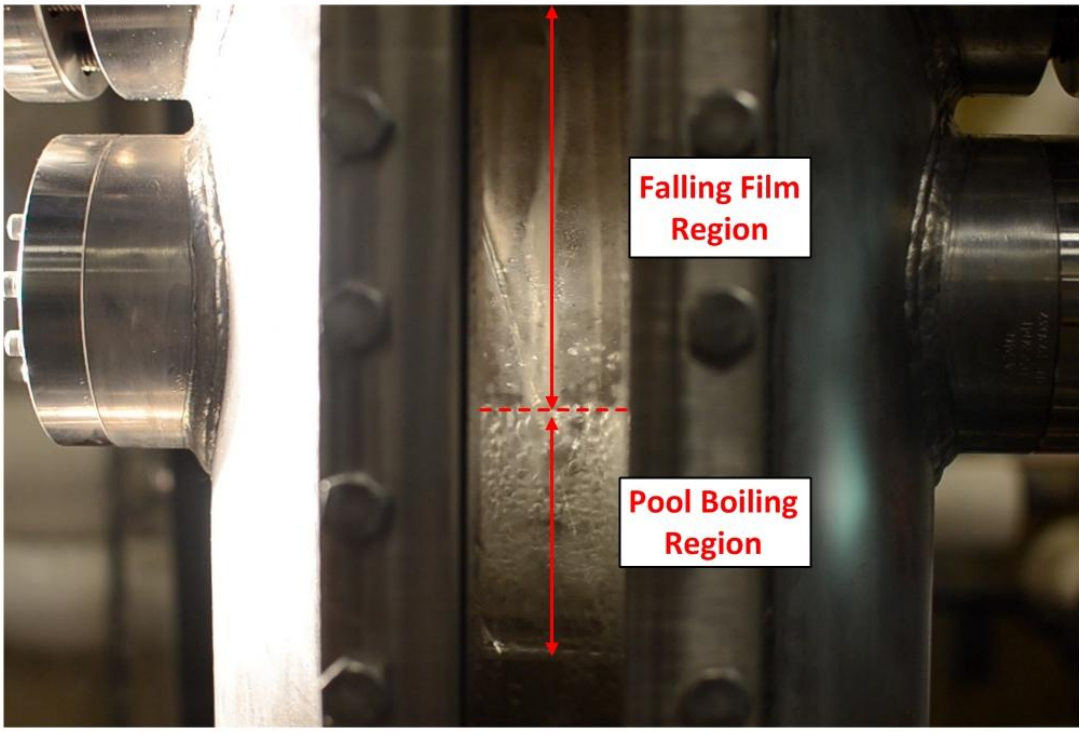

Figure 4.9: Flooded Column in Partially Flooded Operation

4.2.3 Test Matrix

To evaluate the flooded column desorber across a range of operating conditions, heat and mass transfer experiments were conducted across several system pressures, solution flow rates, and Paratherm flow rates. Table 4.5 summarizes the nominal parameter values that compose the test matrix. Data were collected and analyzed at these conditions, with a total of 27 unique data points collected during this study.

Table 4.5: Nominal Test Matrix

Parameter	Units				
Pressure	kPa	410	690	970	1250
Solution Flowrate	g/min	175	275	375	
Paratherm Flowrate	mL/min	200	320	530	

CHAPTER 5: EXPERIMENTAL RESULTS

Flow visualization and heat and mass transfer experiments were conducted on the flooded column desorber across a range of system pressures, solution flowrates and heat inputs. Results from these experiments are presented here.

5.1 Flow Visualization Results

Flow visualization studies on the flooded column desorber across a range of the system pressures, solution flowrates and heating inputs reveal several aspects of its performance. First, pool boiling is a significant mode of heat transfer in this component. Vapor bubbles are seen to nucleate along the length of the heated surface and flow countercurrent to the falling solution. Figure 5.1 presents a representative image of this pool boiling process.

Figure 5.1: Pool Boiling in Flooded Column Desorber

5.1.1 Pool Boiling: Flow Characteristics

Flow visualization experiments also show that this pool boiling process is well mixed in nature; vapor generation and flow within the pool-boiling region promotes efficient mixing between the two phases. Figure 5.2 presents a sequence of images capturing the mixing process within the pool-boiling regime. An eddy is shown forming at the bottom of the column at t = 0. The swirling motion of this eddy is captured as it rises in each progressive image, demonstrating the mixing mechanisms present within the pool-boiling region. Each image is at a time step of 1/24 seconds. The mixing observed in these experiments, and the accompanying heat and mass transfer, play a significant role in the operation of the desorber; higher rates of heat and mass transfer between the vapor and solution serve to cool the generated vapor, thereby preferentially condensing water and increasing the concentration of the refrigerant leaving the desorber.

The extent of mixing in the pool-boiling regime is also suggested by the relative uniformity of the solution temperatures within the component. Four pairs of thermocouples are installed along the length of the flooded column; their locations are shown in Figure 5.3. The spatial variations in solution and Paratherm temperature in the flooded column are presented for a representative data point in Figure 5.4. While the coupling fluid cools by 54°C over the length of the component, including across the falling-film region, a temperature variation of approximately 5.5°C is observed in the solution undergoing pool boiling. Because of the absence of large spatial gradients in solution temperature within the pool-boiling region, and the vigorous mixing observed during flow visualization trials, the average solution temperature within the pool-boiling region is used to represent the process in subsequent data reduction procedures.

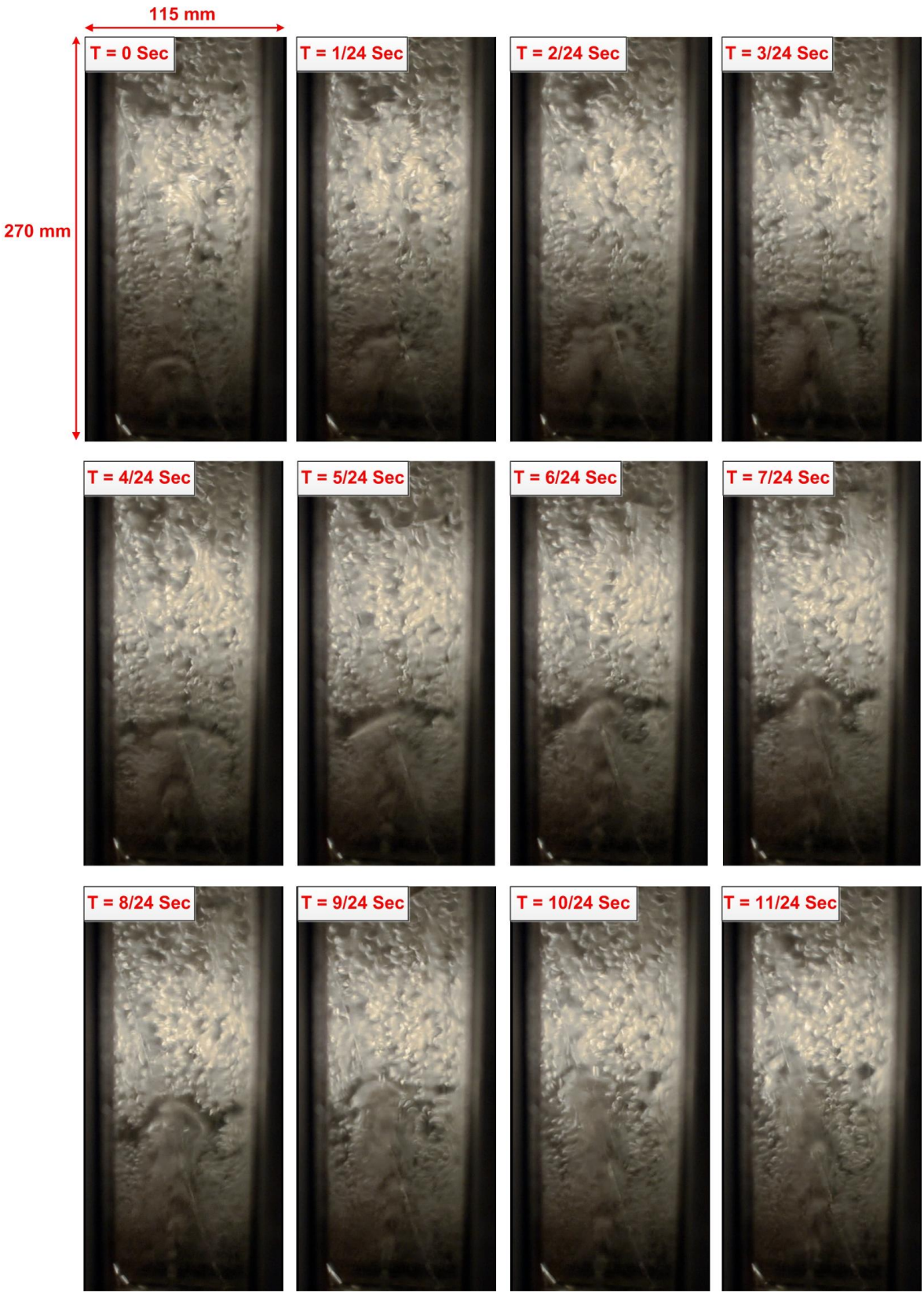

Figure 5.2: Flow Visualization Sequence: Eddy Development

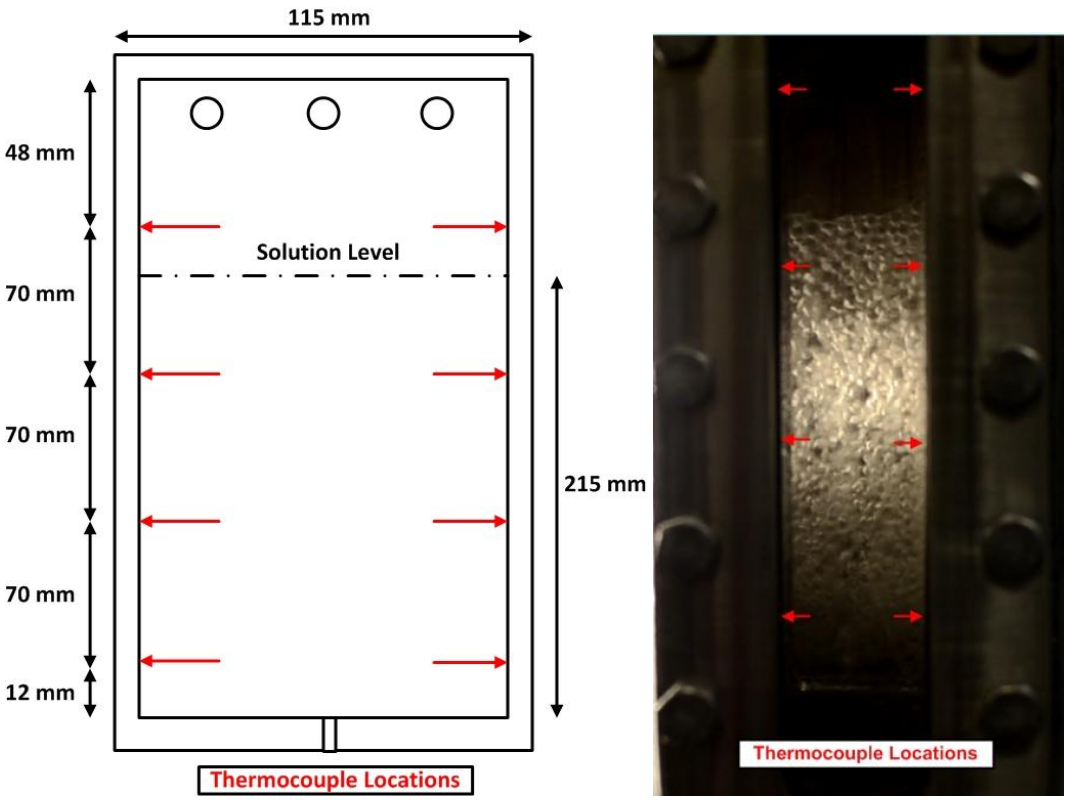

Figure 5.3: Thermocouple Locations: Photograph and Schematic

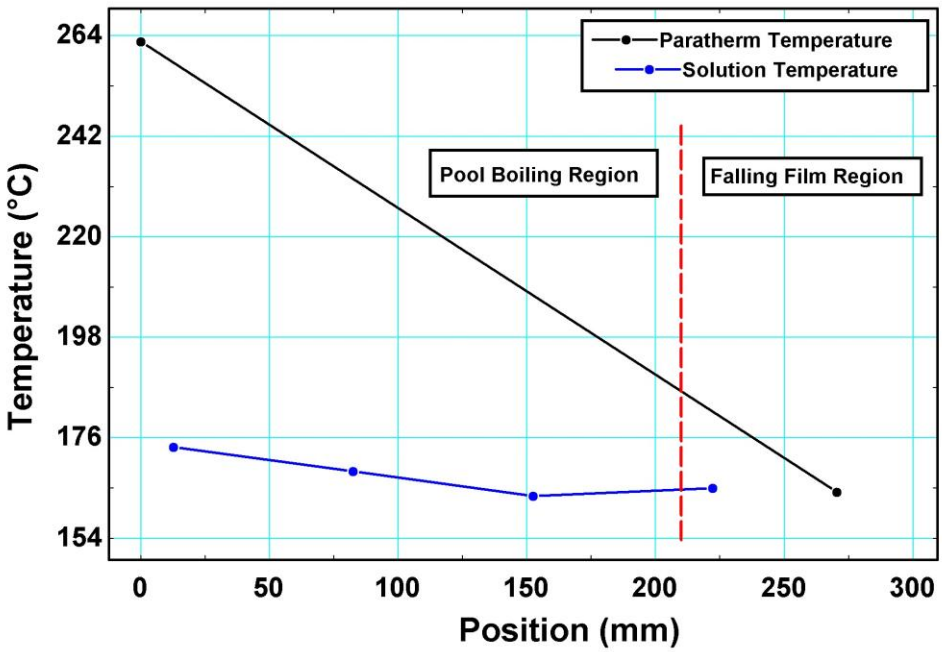

Figure 5.4: Spatial Temperature Distribution in Flooded Column

5.1.2 Variable Solution Level: Partially Flooded Condition

In addition to the turbulent nature of the pool boiling process, another significant characteristic of the flooded column desorber's performance can be established through flow visualization. These investigations showed that the solution level in the desorber is a function of numerous parameters, and that the component operates most stably in a partially flooded condition, where a pool-boiling regime occupied only the lower part of the column. The height of this pool-boiling regime was unstable under certain conditions. Figure 5.5 presents a time-lapse sequence of flow visualization images capturing this varying solution level for a representative run. Each image in Figure 5.5 represents a 1-second time interval. In the sequence shown, the solution level drops from 220 to 60 mm over a 12-second period.

The solution level in the desorber is a function of the pressure difference between the flooded column and the interior of the pressure vessel; this pressure gradient provides the driving force for solution flow out of the bottom of the desorber. Experiments showed that this pressure difference, and thus both the dilute solution flowrate and solution level in the flooded column, are dependent on nearly every adjustable parameter, including the solution flowrate, Paratherm flowrate and temperature, system pressure, and dilute solution and refrigerant valve settings. Many sets of these parameters resulted in the solution level instabilities represented by Figure 5.5, however, subsequent heat and mass transfer studies were conducted only at steady state partially flooded conditions.

At a specified pressure, increasing the solution flowrate into the component tends to increase the solution level. Figure 5.6, a plot of column height versus solution flowrate for each tested pressure, presents this trend. Additionally, experiments showed that increasing the

Paratherm flowrate at a specified pressure tended to decrease the solution level, as shown in Figure 5.7. The Paratherm flowrate directly influences the heat duty, and thus the vapor generation rate; increasing the Paratherm flowrate serves to generate more vapor, increasing the pressure within the desorber and reducing the solution level.

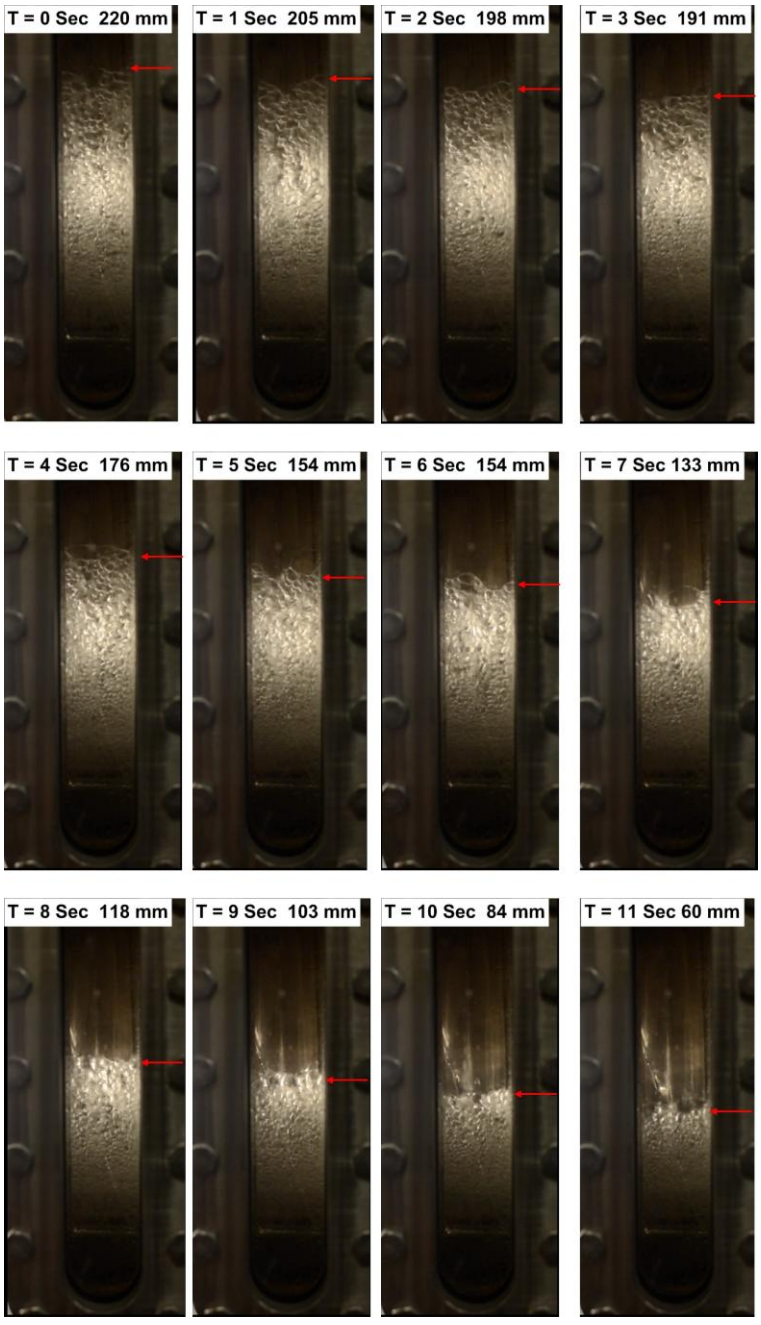

Figure 5.5: Flow Visualization Sequence: Solution Level Variations

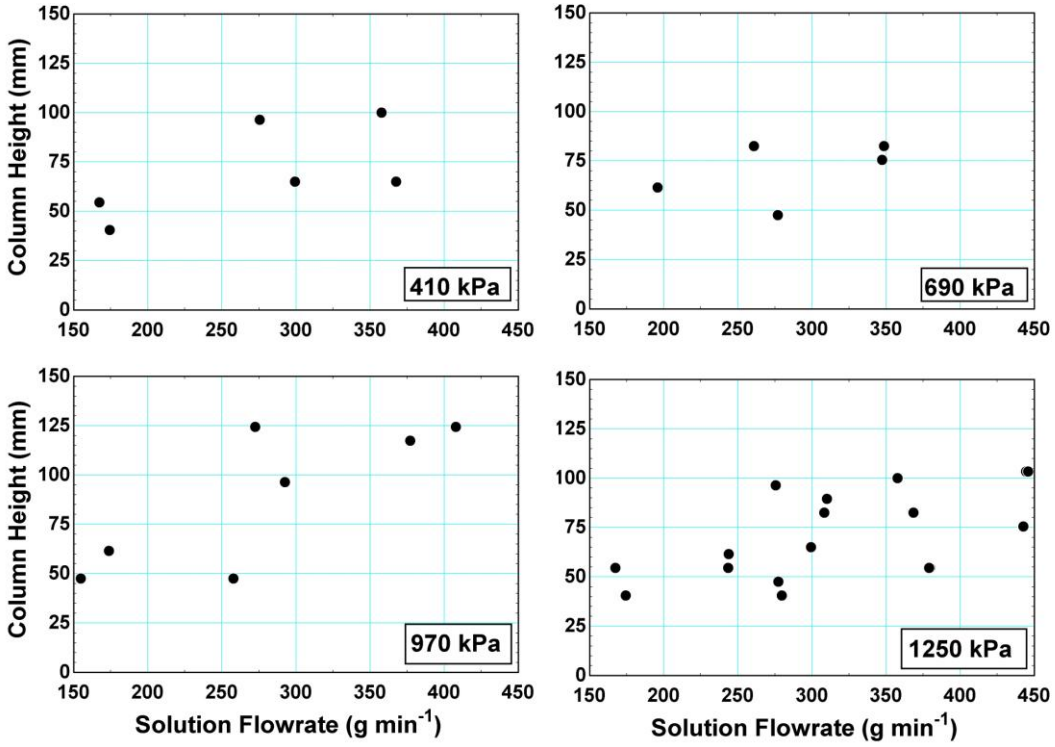

Figure 5.6: Column Height vs. Solution Flowrate for System Pressures of 410, 690, 970 and 1250 kPa

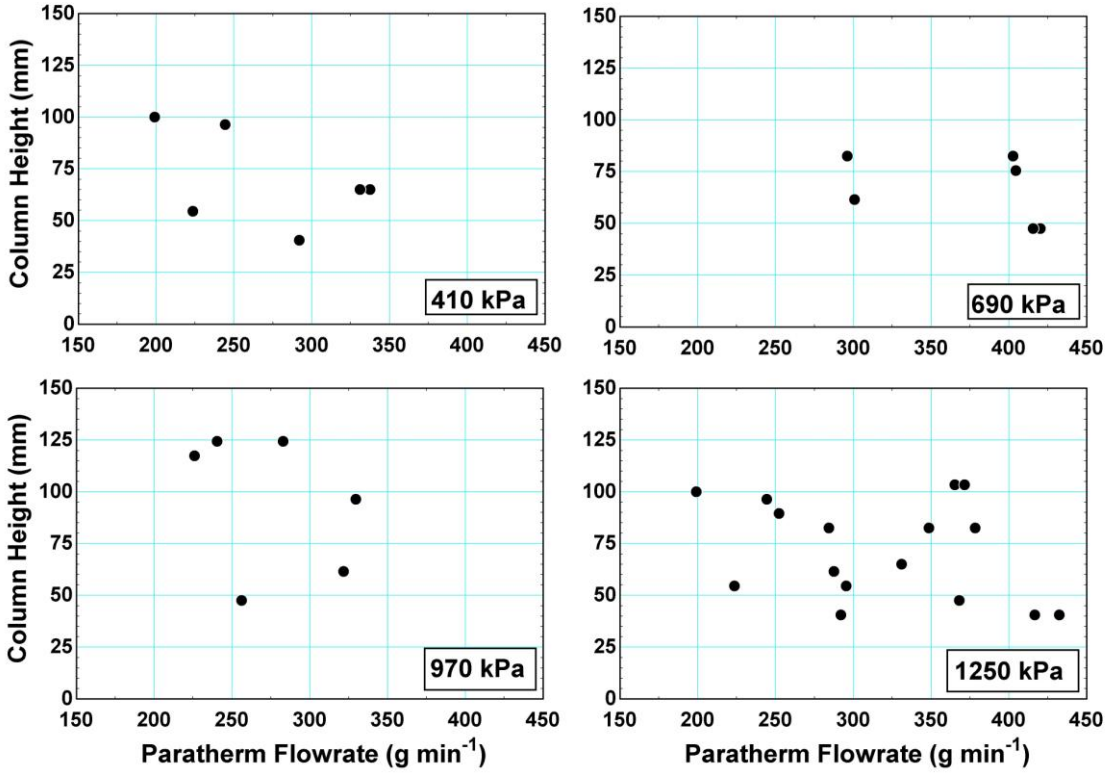

Figure 5.7: Column Height vs. Paratherm Flowrate for System Pressures of 410, 690, 970 and 1250 kPa

5.2 Data Analysis: Partially Flooded Column

The flooded column desorber operated most stably in the partially flooded condition, where both pool-boiling and falling-film regimes contribute. While this partially flooded condition represents a departure from the intended operation of the desorber, it can still provide useful insight into the thermal performance of the design.

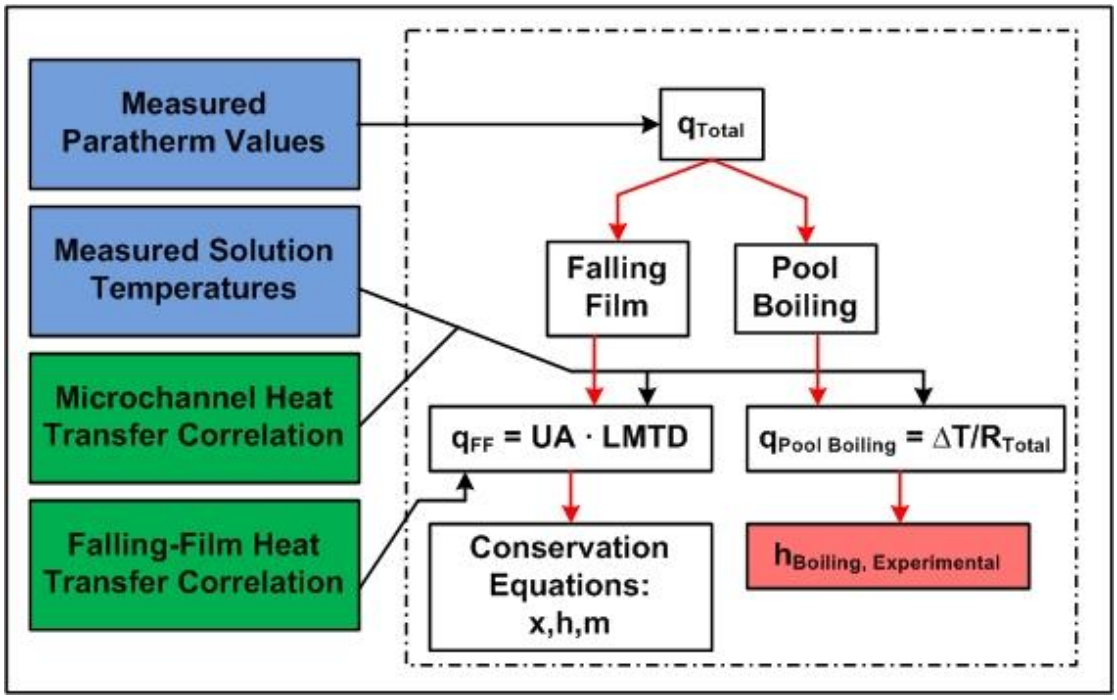

Figure 5.8: Summary of Partially Flooded Data Analysis Procedure

The experimental pool-boiling heat transfer coefficient is used to evaluate the thermal performance of the component; a data reduction procedure was developed to calculate this coefficient from the measured parameters, accounting for heat and mass transfer in both the falling-film and pool-boiling regimes. Figure 5.8 summarizes this procedure.

The analysis begins by using the measured values from the Paratherm loop – the inlet and outlet temperature and flowrate – to calculate the total heat delivered to the desorber. In the partially flooded mode of operation, this total heat supplied to the desorber is subdivided

between the falling-film and pool-boiling regimes. The fraction of heat transferred through each regime is determined through a heat transfer model of the falling-film segment. This model uses a correlation for falling-film heat transfer, as well as mass, species and energy conservation equations. With the amount of heat transferred through the pool-boiling regime identified, the experimental pool-boiling heat transfer coefficient is determined using a resistance network analysis.

Table 5.1 summarizes the measurements employed in the data reduction calculations and their uncertainties. Temperature, pressure and flowrate measurements are taken from the data acquisition system. Additionally, the solution level within the flooded column and the width of the falling-film rivulet are taken from the flow visualization information, as shown in Figure 5.9. In addition to the measurements employed in the data reduction calculations, Table 5.1 lists the two heat transfer correlations used in this analysis; uncertainties of 25% are assumed for both of these correlations.

Table 5.1: Measurements used for Data Reduction Calculations

Measurand	Manufacturer	Model #	Uncertainty
$T_{Coupling\ Fluid,\ Inlet}$	Omega	Type-T TC	0.5°C
$T_{Coupling\ Fluid,\ Outlet}$	Omega	Type-T TC	0.5°C
$T_{solution,\ Inlet}$	Omega	Type-T TC	0.5°C
$T_{Solution,\ Boiling,\ Average}$	Omega	Type-T TC	0.5°C
$V_{Coupling\ Fluid}$	AW-Lake	JVS-20KG	0.5% of Reading
$m_{Solution}$	Rheonik	RHM 015	0.15% of Reading
P_{High}	Wika	A-10	1% of Range

Correlations		
Microchannel Heat Transfer	Sparrow and Haji-Sheikh (1965)	25%
Falling Film Heat Transfer	Chun and Seban (1971)	25%

Figure 5.9: Measurements from Flow Visualization

To demonstrate the data reduction procedure, values from a sample point are considered. Table 5.2 presents the measurements taken for this sample data point, and Figure 5.9 shows the test section during this trial.

Table 5.2: Sample Point Measurements

Table 5.2: Sample Point Measurements					
Measurand	Value	Units	Measurand	Value	Units
$T_{Coupling\ Fluid,\ Inlet}$	136.9	°C	$V_{Coupling\ Fluid}$	398.2	mL/min
$T_{Coupling\ Fluid,\ Outlet}$	89.3	°C	$m_{Solution}$	292.6	g/min
$T_{solution,\ Inlet}$	38.9	°C	P_{High}	846	kPa
$T_{Solution,\ Boiling,\ Average}$	88.2	°C	$L_{Boiling}$	97	mm
22 December, 3:51			$Width_{Falling\ Film}$	12	mm

5.2.1 Heat Duty Calculations

The focus of the present analysis is to determine the heat supplied by the coupling fluid to both the falling-film and pool-boiling regimes which is reflected in the temperature of the coupling fluid at the inlet of the falling-film regime, as shown in Figure 5.10. This intermediate coupling fluid temperature is calculated by the closed model to be $T_{CF,In,FF} = 120\ ^{\circ}C$. The inlet and outlet Paratherm temperatures are measured as reported in Table 5.2. For the sample data point:

$$T_{CF,In} = 136.9\ ^{\circ}C;\ T_{CF,In,FF} = 120\ ^{\circ}C;\ T_{CF,Out} = 89.3\ ^{\circ}C$$

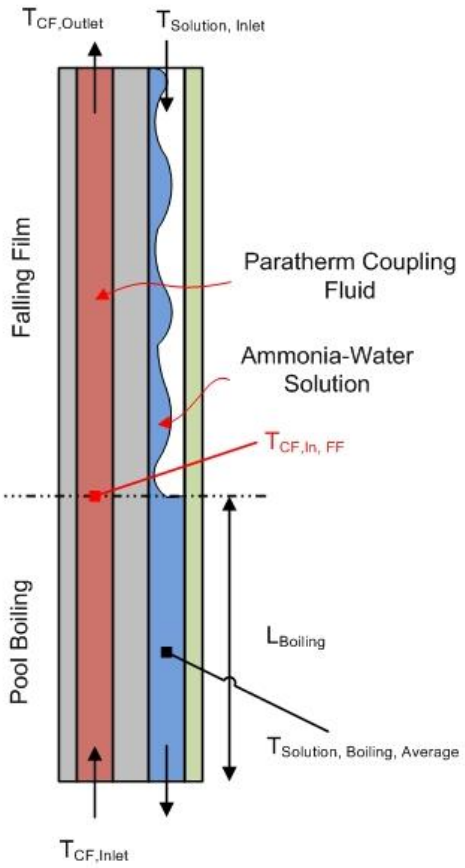

Figure 5.10: Partially Flooded Data Analysis Schematic

The temperature-dependent Paratherm properties are calculated at the average temperature in the falling-film region, and are reported below. Equation 5.1 uses these property values to calculate the Paratherm mass flowrate from the measured volumetric flowrate. Using the Paratherm temperatures, properties and mass flowrate, the heat supplied to the falling-film region is calculated using Equation 5.2.

$$\left(Cp_{CF,FF}, \rho_{CF,FF}\right) = f\left(T_{CF,Ave,FF}\right);\ Cp_{CF,FF} = 2.274\ \frac{kJ}{kg\text{-}K};\ \rho_{CF,FF} = 827.9\ \frac{kg}{m^3}$$

$$m_{CF,FF} = V_{CF,mL/min} \bullet \rho_{CF,FF} \bullet \left(\frac{m^3}{100^3 mL}\right)\bullet\left(\frac{min}{60sec}\right)$$
$$m_{CF,FF} = 0.005494\frac{kg}{s} \qquad (5.1)$$

$$Q_{Falling\ Film} = m_{CF,FF} \bullet Cp_{CF,FF}\ \left(T_{CF,In,FF} - T_{CF,Out}\right) \qquad (5.2)$$

For the sample point considered here:

$$Q_{Falling\ Film} = 0.005494\frac{kg}{s} \bullet 2.27\frac{kJ}{kg\text{-}K}\ \left(120^oC - 89.3^oC\right)$$
$$Q_{Falling\ Film} = 0.3835\ kW$$

Similarly, the heat supplied to the pool-boiling region can be evaluated. Again, the temperature-dependent properties of the Paratherm are evaluated at the average temperature in the pool-boiling region, and are reported below. The Paratherm mass flowrate in the pool-boiling region is calculated using Equation 5.3. The heat transferred to the pool-boiling region is calculated using Equation 5.4.

$$\left(Cp_{CF,FF}, \rho_{CF,FF}\right) = f\left(T_{CF,Ave,PB}\right);\ Cp_{CF,PB} = 2.399\ \frac{kJ}{kg\text{-}K};\ \rho_{CF,PB} = 812.1\ \frac{kg}{m^3}$$

$$m_{CF,PB} = V_{CF,mL/min} \bullet \rho_{CF,PB} \bullet \left(\frac{m^3}{100^3 mL}\right) \bullet \left(\frac{min}{60sec}\right)$$
$$m_{CF,PB} = 0.00539 \frac{kg}{s} \tag{5.3}$$

$$Q_{Pool\ Boiling} = m_{CF,PB} \bullet Cp_{CF,PB} \left(T_{CF,In} - T_{CF,IN,PB}\right) \tag{5.4}$$

For the sample point considered:

$$Q_{Pool\ Boiling} = 0.00539 \frac{kg}{s} \bullet 2.399 \frac{kJ}{kg\text{-}K} \left(136.9^oC - 120^oC\right)$$
$$Q_{Pool\ Boiling} = 0.2195\ kW$$

For this data point, therefore, 36% of the heat is transferred in the pool-boiling region.

To validate the intermediate Paratherm temperature, $T_{CF,In,FF}$, heat transfer in the falling-film region is modeled. In this model, a resistance network analysis is used to determine the

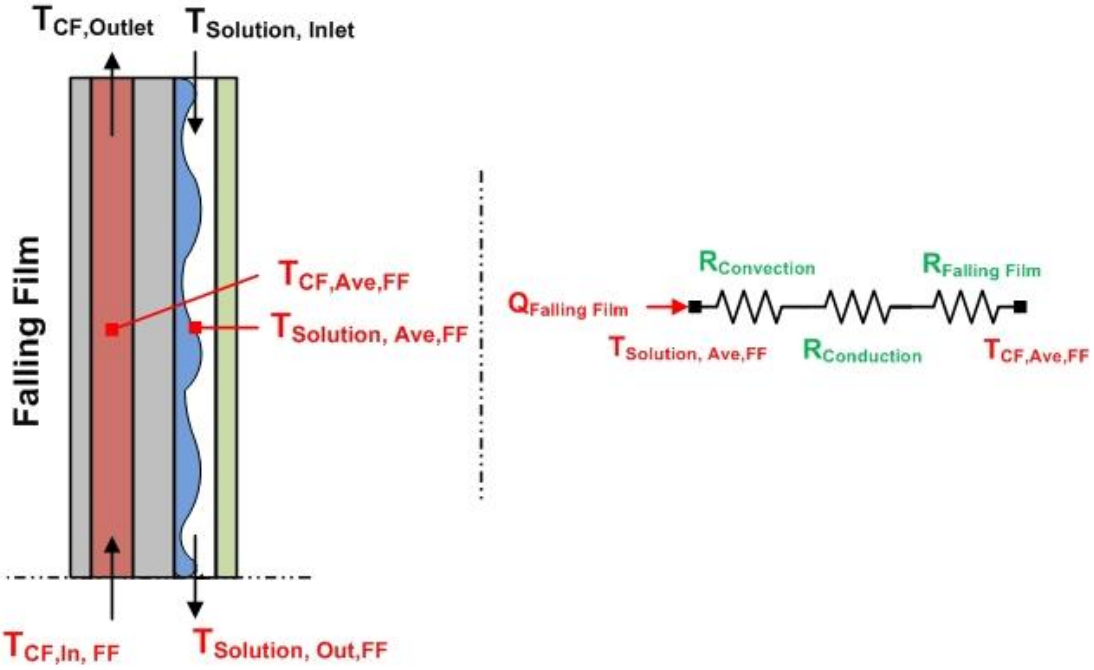

Figure 5.11: Falling-Film Model Schematic

conductance between the coupling fluid and the falling-film solution. This conductance is used in a UA - LMTD analysis to determine the solution temperature at the outlet of the falling-film segment. Equations for the conservation of mass, species and energy close the falling-film segment model. The falling-film segment and this modeling process is outlined schematically in Figure 5.11.

5.2.2 Resistance Network Analysis

The analysis of the falling-film regime begins with the resistance network between the coupling fluid and the falling film. Three resistances are included: convection resistance in the microchannel, conduction resistance across the column wall, and convection resistance to the falling film. These resistances, and their series sum, are presented as Equations 5.5 – 5.8.

$$UA = \frac{1}{R_{Total}}; \quad R_{Total} = R_{Convection} + R_{Conduction} + R_{Falling\ Film} \tag{5.5}$$

$$R_{Convection} = \frac{1}{h_{CF,FF} A_{CF,FF} \eta_T} \tag{5.6}$$

$$R_{Conduction} = \frac{\delta_{Wall}}{k_{Wall} A_{Wall,FF}} \tag{5.7}$$

$$R_{Falling\ Film} = \frac{1}{h_{FF} A_{Wall,FF}} \tag{5.8}$$

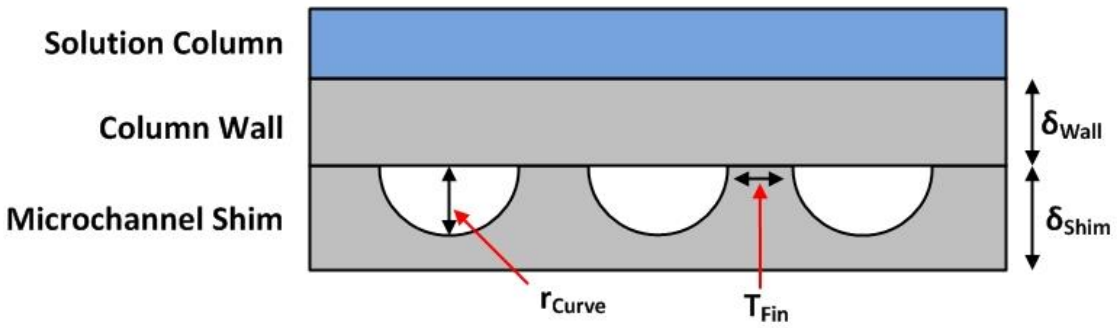

Figure 5. 12: Microchannel Geometry Schematic

Figure 5.12 presents a schematic of the cross-section of the desorber. The heat transfer area used in the microchannel convection resistance term is calculated from this geometry. This area, $A_{CF,FF}$, is calculated from the number of channels, the channel radius, and the length of the falling-film segment, as shown in Equation 5.9. Values for these parameters for the sample point are presented below:

$$r_{Curve} = 0.356 \text{ mm};\ N_{Channel} = 92;\ \text{Height} = 267.7 \text{ mm};\ L_{Boiling} = 96.52 \text{ mm}$$

$$A_{CF,FF} = \left(\pi \bullet r_{Curve} + 2 \bullet r_{Curve}\right) \bullet N_{Channel}\left(\text{Height} - L_{Boiling}\right) \tag{5.9}$$

$$A_{CF,FF} = 0.001828 \text{ m} \bullet 92\ \left(0.2677 \text{ m} - 0.09652 \text{ m}\right)$$

For the sample point, $A_{CF,FF} = 0.0288 \text{ m}^2$.

The single-phase heat transfer coefficient in the Paratherm microchannel is calculated using the Sparrow and Haji-Sheikh (1965) correlation for laminar flow in semicircular microchannels, as reported by Kakac *et al.* (1987), and presented as Equation 5.10. For the

sample point considered, the hydraulic diameter and average Paratherm conductivity are reported below, where $D_h = \frac{4A_{CF,FF}}{\left(\pi \bullet r_{Curve} + 2 \bullet r_{Curve}\right)}$.

$$D_h = 0.4346 \text{ mm}; \; k = 0.1007 \; \frac{W}{m\text{-}K}$$

$$h_{CF,FF} = \frac{k}{D_h}\left(2.0705 \bullet \left(1 + 2.2916 \bullet \phi - 2.5682 \bullet \phi^2 + 1.4815 \bullet \phi^3 - 0.3338 \bullet \phi^4\right)\right) \quad (5.10)$$

$$\text{where } \phi = \frac{\pi}{2}$$

Using the hydraulic diameter and Paratherm conductivity from the sample point:

$$h_{CF,FF} = \frac{0.1007}{0.0004346}\left(2.0705 \bullet \left(1 + 2.2916 \bullet \phi - 2.5682 \bullet \phi^2 + 1.4815 \bullet \phi^3 - 0.3338 \bullet \phi^4\right)\right); \; \phi = 1.571$$

$$h_{CF,FF} = 946.2 \frac{W}{m^2 K}$$

The calculations for the microchannel convection resistance account for temperature gradients within the microchannel shim by introducing an array efficiency, η_T. To determine this efficiency, the microchannel shim is modeled as an array of fins, as reported in Appendix B. The calculations in Appendix B show that this array efficiency approaches unity, due to the geometric dimensions of the microchannels and the large shim thermal conductivity. Because this efficiency approaches unity, all of the microchannel area $A_{CF,FF}$ can be approximated as prime area.

With the active area, heat transfer coefficient and total fin array efficiency defined for the coupling fluid passages in the falling-film segment, the thermal resistance is calculated using Equation 5.6. For the sample point considered, $R_{Convection} = 0.0367\ K/W$.

$$R_{Convection} = \frac{1}{946.2 \frac{W}{m^2 K}\ 0.0288\ m^2}$$

The area term in the conduction resistance is calculated using the rivulet width and the falling-film segment length, as shown in Equation 5.11. These intermediate values for the sample point considered are shown in Figure 5.9 and are reported below:

$$L_{Boiling} = 97\ mm;\ Width_{FF} = 12\ mm$$

$$A_{Wall,FF} = Width_{FF} \bullet \left(Height - L_{Boiling}\right) \tag{5.11}$$

For the sample point considered, $A_{Wall,FF} = 0.002038\ m^2$

In addition to this area term, the wall thickness and conductivity are required to calculate the conduction resistance. For the sample point considered, these values are reported below.

$$\delta_{Wall} = 0.2794\ mm;\ k_{Wall} = 16.0\ \frac{W}{m\text{-}K}$$

From these values, the thermal resistance due to conduction across the column wall is calculated using Equation 5.7. For the sample point considered, $R_{Conduction} = 0.008567\ K/W$.

$$R_{Conduction} = \frac{0.0002794\ m}{16.0\ \frac{W}{m\text{-}K} \bullet 0.002038\ m^2}$$

The final thermal resistance, due to convection to the falling film, is calculated using Equation 5.8, and employs the same area term, $A_{Wall,FF}$. The heat transfer coefficient to the falling film is calculated using the turbulent correlation of Chun and Seban (1971), as reported by Rohsenow *et al.* (1998), and is presented as Equation 5.12. Solution property values for the sample point considered are reported below:

$$Re_{FF} = 4182;\ \mu = 0.0003918\ \frac{\text{N-s}}{\text{m}^2};\quad Cp = 4.632\ \frac{\text{kJ}}{\text{kg-K}};\ k = 0.5062\ \frac{\text{W}}{\text{m-K}};\ \rho = 743.2\frac{\text{kg}}{\text{m}^3}$$

$$h_{FF} = k \bullet 0.0038\left(Re_{FF}\right)^{0.4}\left(\frac{\mu Cp}{k}\right)^{0.65}\left(\frac{\mu}{\rho\sqrt{g}}\right)^{-2/3} \tag{5.12}$$

$$h_{FF} = \left(0.5062\right) \bullet 0.0038\left(4182\right)^{0.4}\left(\frac{0.0003918 \bullet 4.632}{0.5062}\right)^{0.65}\left(\frac{0.0003918}{743.2\sqrt{9.81}}\right)^{-2/3}$$

For the sample point considered, $h_{FF} = 4063\frac{\text{W}}{\text{m}^2\text{-K}}$

With the active area and heat transfer coefficient defined, the thermal resistance for convection to the falling film is calculated from Equation 5.8. For the sample point considered, $R_{\text{Falling Film}} = 0.1207\frac{\text{K}}{\text{W}}$.

$$R_{\text{Falling Film}} = \frac{1}{4063\ \frac{\text{W}}{\text{m}^2\text{-K}} \bullet 0.002038\text{m}^2}$$

With the three component resistances defined, the total series resistance is calculated from Equation 5.5. For the sample point considered, $R_{\text{Total}} = 0.166\ \frac{\text{K}}{\text{W}}$ and $UA = 6.025\ \frac{\text{W}}{\text{K}}$.

$$UA = \frac{1}{R_{Total}}; \quad R_{Total} = 0.0367\frac{K}{W} + 0.008567\frac{K}{W} + 0.1207\frac{K}{W}$$

These resistance network calculations demonstrate that the falling-film evaporation term contributes most significantly to the thermal resistance of this pathway. The large heat transfer area of the microchannel array, and the high conductivity of the wall material minimize the single-phase convection and conduction terms.

5.2.3 UA - LMTD Analysis

Having defined the total conductance between the Paratherm coupling fluid and the falling film, and the heat duty of the falling-film segment, a UA - LMTD analysis is used to determine the solution temperature at the outlet of the falling-film segment. Equation 5.13 presents the equation that relates the heat transferred in the falling-film segment to the total conductance and an effective temperature difference.

$$Q_{FallingFilm} = UA \bullet LMTD \tag{5.13}$$

The Log Mean Temperature Difference used in Equation 5.13 is defined by Equation 5.14. A schematic of the falling-film region is shown in Figure 5.13, with the temperatures required for the LMTD calculation identified.

$$LMTD = \frac{\Delta T_A - \Delta T_B}{\ln\left(\Delta T_A / \Delta T_B\right)} \tag{5.14}$$

where $\Delta T_A = T_{CF,Out} - T_{Solution,In}$ and $\Delta T_B = T_{CF,In,FF} - T_{Solution,Out,FF}$

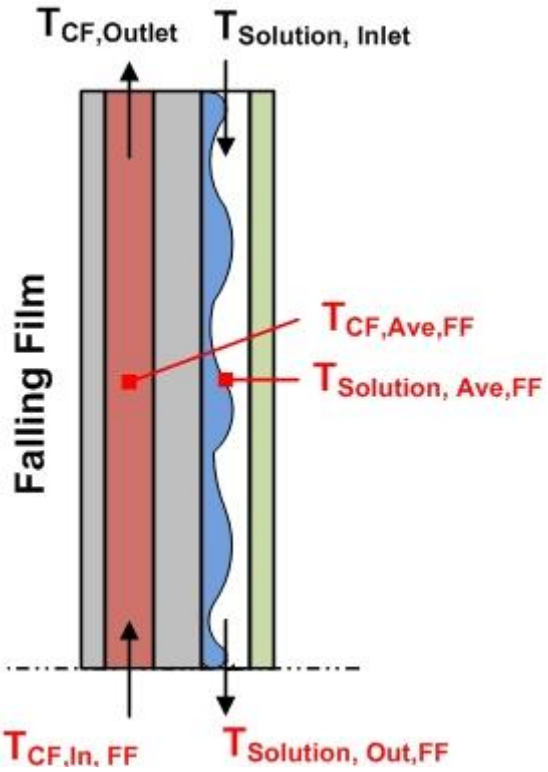

Figure 5.13: Falling Film Segment LMTD Schematic

Four temperatures are required for the LMTD. Two, $T_{CF,Out}$ and $T_{Solution,In}$, are measured values. The intermediate coupling fluid temperature, $T_{CF,In,FF}$, is obtained from the closed model as described in the next section; for the sample point considered, the closed model calculates $T_{CF,In,FF} = 120\ ^{\circ}C$. The final temperature, $T_{Solution,Out,FF}$, is obtained by solving Equation 5.13.

$$Q_{Falling\ Film} = 0.3835\ kW \text{ and } UA = 6.025\ \frac{W}{K}$$

$$383.5\ W = 60.025\frac{W}{K} \bullet LMTD \qquad LMTD = 63.65\ K$$

$$\Delta T_A = 89.28 - 38.94 = 50.33\ ^\circ C \qquad \Delta T_B = 79.13\ ^\circ C = 120 - T_{Solution,Out,FF}$$

For the sample point considered, $T_{Solution,Out,FF} = 40.84\ ^oC$.

5.2.4 Falling–Film Conservation Equations

The solution temperature at the outlet of the falling-film region was identified through the UA – LMTD analysis discussed above. In the preceding analysis, $T_{CF,In,FF}$ was presented as a product of the completed model; to close the model and validate the assumed $T_{CF,In,FF}$, a set of three conservation equations is solved for the falling-film segment. The mass, species and energy conservation equations for the falling-film segment are presented as Equations 5.15 – 5.17.

$$m_{Solution,In} = m_{Solution,Out,FF} + m_{Vapor,Out,FF} \tag{5.15}$$

$$m_{Solution,In} \bullet x_{Solution,In} = m_{Solution,Out,FF} \bullet x_{Solution,Out,FF} + m_{Vapor,Out,FF} \bullet x_{Vapor,Out,FF} \tag{5.16}$$

$$m_{Solution,In} \bullet h_{Solution,In} + Q_{Falling\ Film} = m_{Solution,Out,FF} \bullet h_{Solution,Out,FF} + m_{Vapor,Out,FF} \bullet h_{Vapor,Out,FF} \tag{5.17}$$

These three equations are solved with the following set of assumptions. First, the desorber is assumed to operate at a single pressure, P_{System}, which is a measured value. Second, the liquid solution in the falling-film region is assumed to have a quality $q = 0$, while the generated vapor is assumed to be $q = 1$. Third, it is assumed that the vapor generated in the falling-film segment is generated at the average saturation temperature of the solution. Finally, the vapor stream from the pool-boiling region is assumed to have no influence on heat transfer in

the falling-film segment; this assumption is supported by the small solution - to - vapor interfacial area in the falling-film region, and the low heat transfer coefficients anticipated between these phases.

Equations of state are used to relate the concentration and enthalpy of the ammonia – water solution to the temperature, pressure and quality. When solved simultaneously, the conservation equations and equations of state determine the solution temperature at the falling-film segment outlet to be $T_{Solution,Out,FF} = 40.84\ ^{o}C$, the same value determined by the UA – LMTD analysis. This agreement demonstrates that the model is closed.

5.2.5 Pool-Boiling Segment

Having closed the heat transfer model for the falling-film segment, the heat duties for both the pool-boiling and falling-film segments are known. The heat duty for the pool-boiling segment, calculated from Equation 5.3, is used in a resistance network model to determine the experimental pool-boiling heat transfer coefficient. In the pool-boiling region, the thermal pathway between the coupling fluid and the flooded column consists of three resistances: convection resistance in the microchannel, conduction resistance across the wall, and convection resistance due to pool boiling in the flooded column. As in the falling-film segment, the microchannel convection and conduction resistances are easily calculated. The pool-boiling coefficient is then calculated by subtracting these two resistances from the total resistance, which is determined experimentally. Figure 5.14 presents the schematic of the pool-boiling segment used for this analysis.

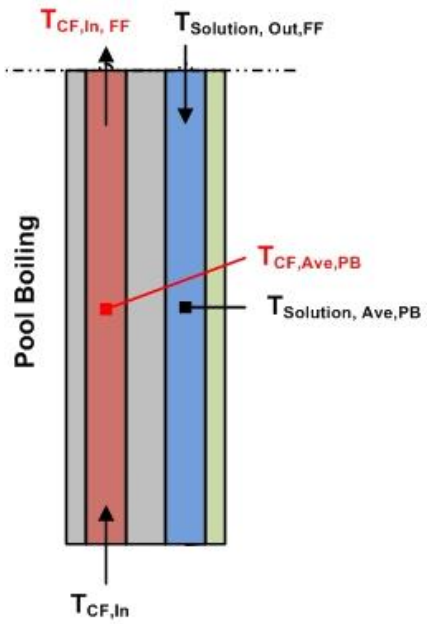

Figure 5.14: Pool Boiling Segment

Having calculated the heat transferred through the pool-boiling segment, $Q_{\text{Pool Boiling}}$, and the temperature difference between the coupling fluid and the solution, $\left(T_{\text{CF,Ave,PB}} - T_{\text{Solution,Ave,PB}}\right)$, the total resistance in the thermal pathway can be calculated from Equation 5.18.

$$Q_{\text{Pool Boiling}} = \left(T_{\text{CF,Ave,PB}} - T_{\text{Solution,Ave,PB}}\right) \bullet {}^{1}\!/_{R_{\text{Total}}} \tag{5.18}$$

For the data point considered, Equation 5.3 provides $Q_{\text{Pool Boiling}} = 0.2195\ \text{kW}$, while direct measurements provide $T_{\text{CF, Ave, PB}} = 128.5\ ^{\circ}\text{C}$, and $T_{\text{Solution, Ave, PB}} = 88.17\ ^{\circ}\text{C}$. From these values the total thermal resistance in the pool-boiling region is calculated to be $R_{\text{Total}} = 0.1835\ \text{K/W}$.

$$219.5\ \text{W} = \left(128.5^{\circ}\text{C} - 88.17^{\circ}\text{C}\right) \bullet {}^{1}\!/_{R_{\text{Total}}}$$

This total thermal resistance is equal to the series sum of the three component resistances, as shown in Equation 5.19.

$$R_{Total} = R_{Convection} + R_{Conduction} + R_{Pool\ Boiling} \tag{5.19}$$

The microchannel convection resistance is calculated from the active area and the microchannel heat transfer coefficient, as shown in Equation 5.20. As for the falling-film region, the active area is a function of the channel count and perimeter, and the height of the solution level in the flooded column; additionally, the fin array efficiency is assumed to be $\eta_T = 1$ based on the calculations presented in Appendix B. The heat transfer coefficient is calculated from the Sparrow and Haji-Sheikh (1965) correlation to $h_{CF,PB} = 946.2 \frac{W}{m^2 - K}$.

$$R_{Convection} = \frac{1}{h_{CF,PB} A_{CF,PB} \eta_T} \tag{5.20}$$

$$A_{CF,PB} = P_{Channel} \bullet N_{Channel} \left(L_{Boiling} \right) \tag{5.21}$$

For the sample point considered, $A_{CF,PB} = 0.01624\ m^2$ and $R_{Convection} = 0.06509 \frac{K}{W}$.

$$R_{Convection} = \frac{1}{946.2 \frac{W}{m^2 K} \bullet 0.01624 m^2}$$

The conduction term is, as in the falling-film segment, calculated from the active area, the wall thickness and thermal conductivity. Equation 5.22 is used to calculate the conduction resistance in the pool-boiling segment. The active area is calculated from the column height and the channel width, as shown in Equation 5.23.

$$R_{Conduction} = \frac{\delta_{Wall}}{k_{Wall} A_{Wall,PB}} \tag{5.22}$$

$$A_{Wall,PB} = \text{Width} \bullet L_{Boiling} \tag{5.23}$$

For the sample point considered, $A_{Wall,PB} = 0.01103\ m^2$, $\delta_{Wall} = 0.2794\ mm$, and $k_{Wall} = 16.0\ W/m\text{-}K$. The conduction resistance is calculated to be $R_{Conduction} = 0.001538\ K/W$

$$R_{Conduction} = \frac{0.0002794\ m}{16.0\ \frac{W}{m\text{-}K} \bullet 0.01103 m^2}$$

With the microchannel convection and conduction resistances calculated, and the total resistance determined from Equation 5.18, Equation 5.19 can be solved to determine the resistance due to pool boiling. For the sample point considered, $R_{Pool\ Boiling} = 0.1169\ K/W$.

This pool-boiling resistance is a function of the active area from Equation 5.23, and the experimental pool-boiling coefficient, as shown in Equation 5.24. For the sample point considered, $h_{PB,Experimental} = 775.6\ W/m^2\text{-}K$.

$$R_{Pool\ Boiling} = \frac{1}{h_{PB,Experimental} A_{Wall,PB}} \tag{5.24}$$

$$0.1169 \frac{K}{W} = \frac{1}{h_{PB,Experimental} \bullet 0.01103\ m^2}$$

5.3 Pool-Boiling Coefficient Correlation Development

Using the data analysis procedure described above, experimental pool-boiling coefficients were calculated for all of the statepoints considered. Heat and mass transfer experiments were conducted across a range of solution flowrates, Paratherm flowrates and system pressures. At a given pressure, changing the solution and Paratherm flowrates did influence the calculated experimental pool-boiling coefficient. However, a plot of the pool-boiling coefficient as a function of the heat flux in the pool-boiling region does not exhibit a strong dependence on the solution and Paratherm flowrates; these flowrates influence the solution level within the flooded column, which is accounted for in the data analysis. For a given system pressure, the experimental pool-boiling coefficients vary approximately linearly with heat flux. Figure 5.15 demonstrates this trend with plots of the data at each pressure considered. Figure 5.16 presents the data at all pressures together.

The experimental boiling heat transfer coefficients were compared with the predictions of correlations developed for the pool boiling of multi-component mixtures. As discussed in Chapter 3, multi-component mixture pool-boiling correlations are based on ideal heat transfer coefficients, based on a molar average of the coefficients for both pure substances, combined with corrections to account for the binary fluid heat and mass transfer phenomena.

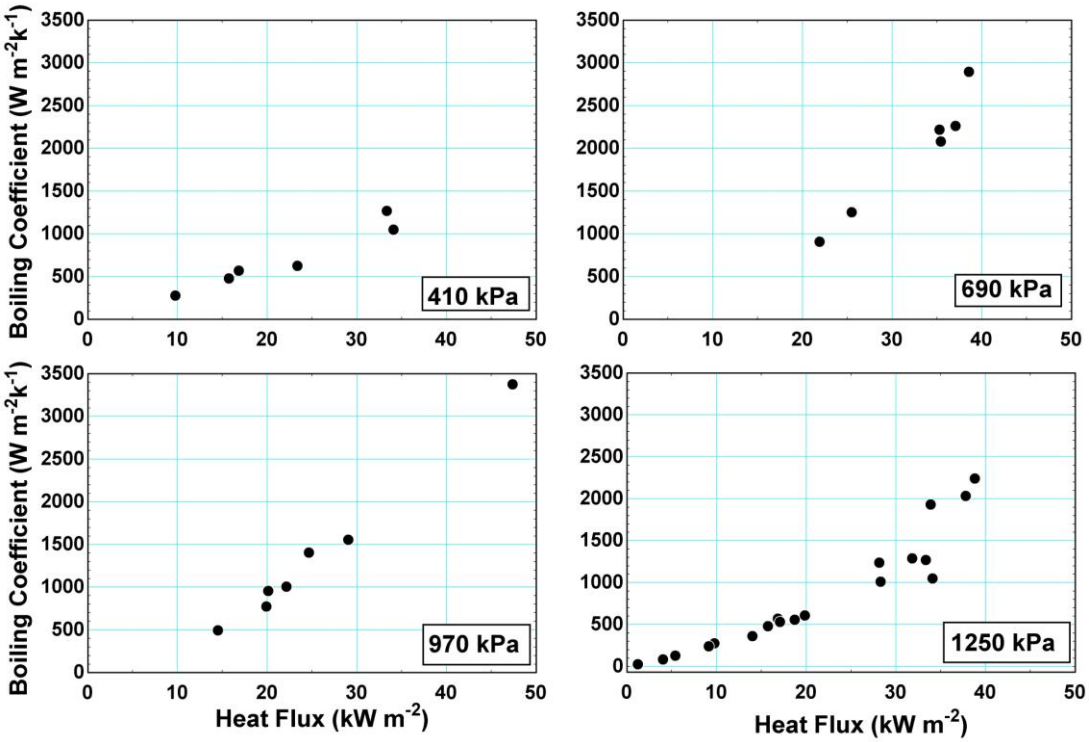

Figure 5.15: Experimental Pool Boiling Coefficients vs. Heat Flux at 410 kPa, 690 kPa, 970 kPa and 1250 kPa

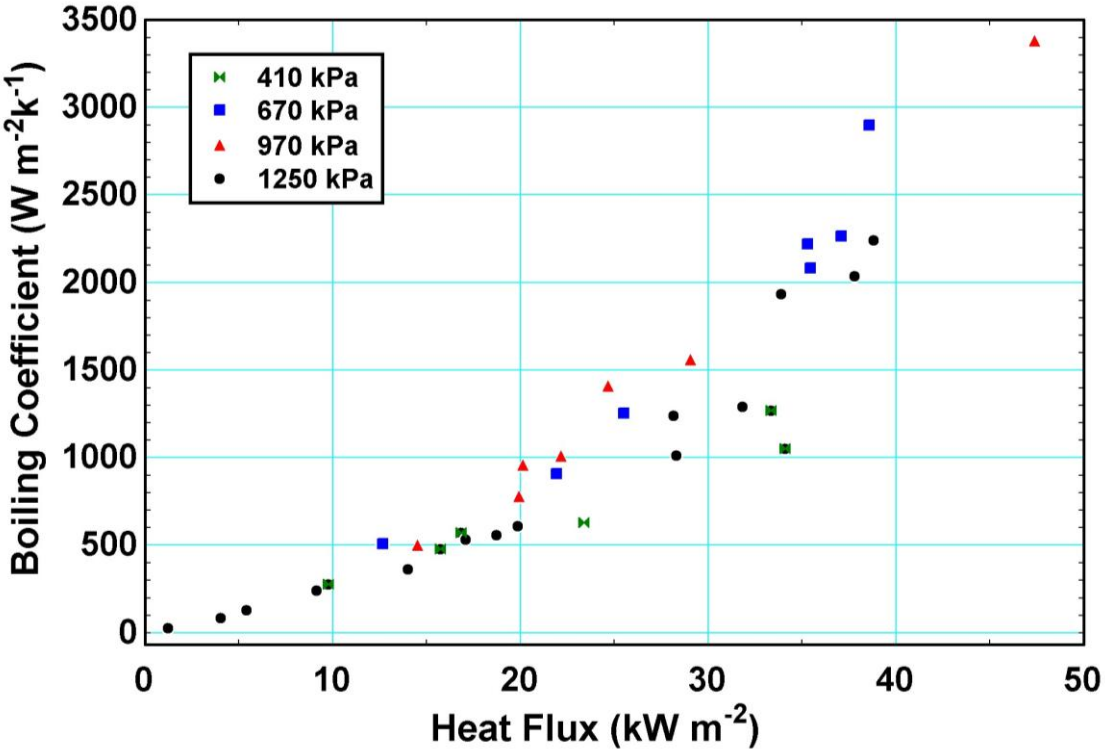

Figure 5.16: Experimental Heat Transfer Coefficients vs. Heat Flux for All Pressures

This ideal coefficient is adjusted by a correction factor, which accounts for the heat and mass transfer resistances inherent to the multi-component nature of the mixture. Numerous authors have developed multi-component correction factors of various forms. Four different correction factors were applied to the Mostinski (1963) pure-component correlation and were compared with the data from this study, as shown in Figures 5.17 and 5.18.

All of the correction factors attempt to account for the resistance to pool boiling due to the multi-component nature of the mixture. Stephan and Korner (1969) developed their correction factor based on the assumption that the representative temperature difference in a non-azeotropic mixture is higher than that in an azeotropic mixture by a specified value, which they found related to the difference in concentration between the vapor and solution phases.

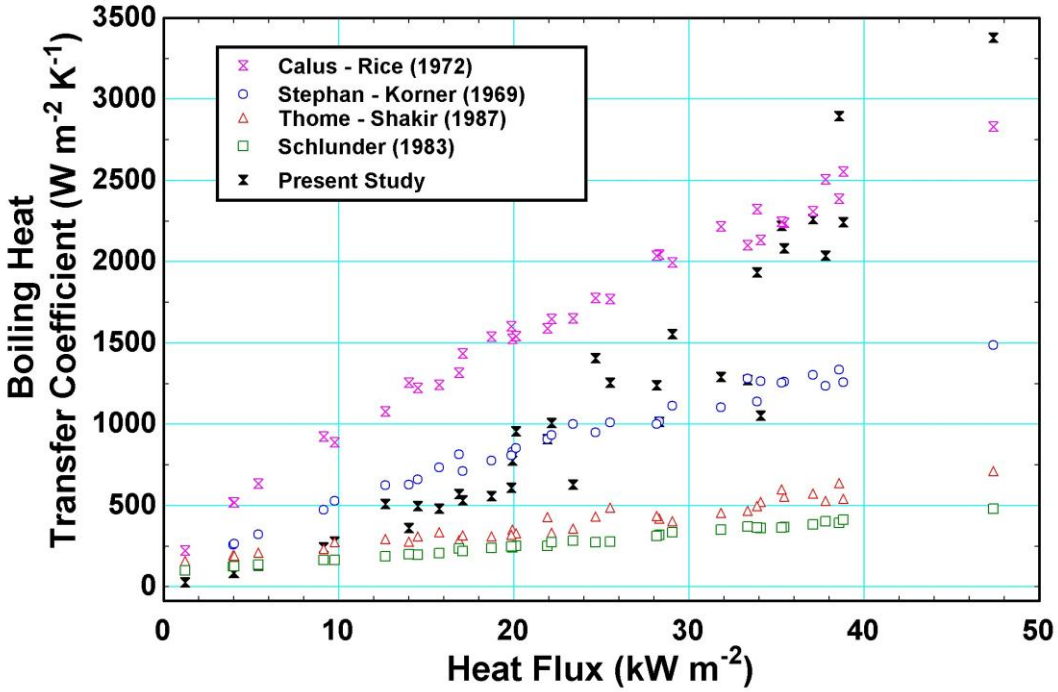

Figure 5.17: Various Multi-Component Correction Factors with the Experimental Data

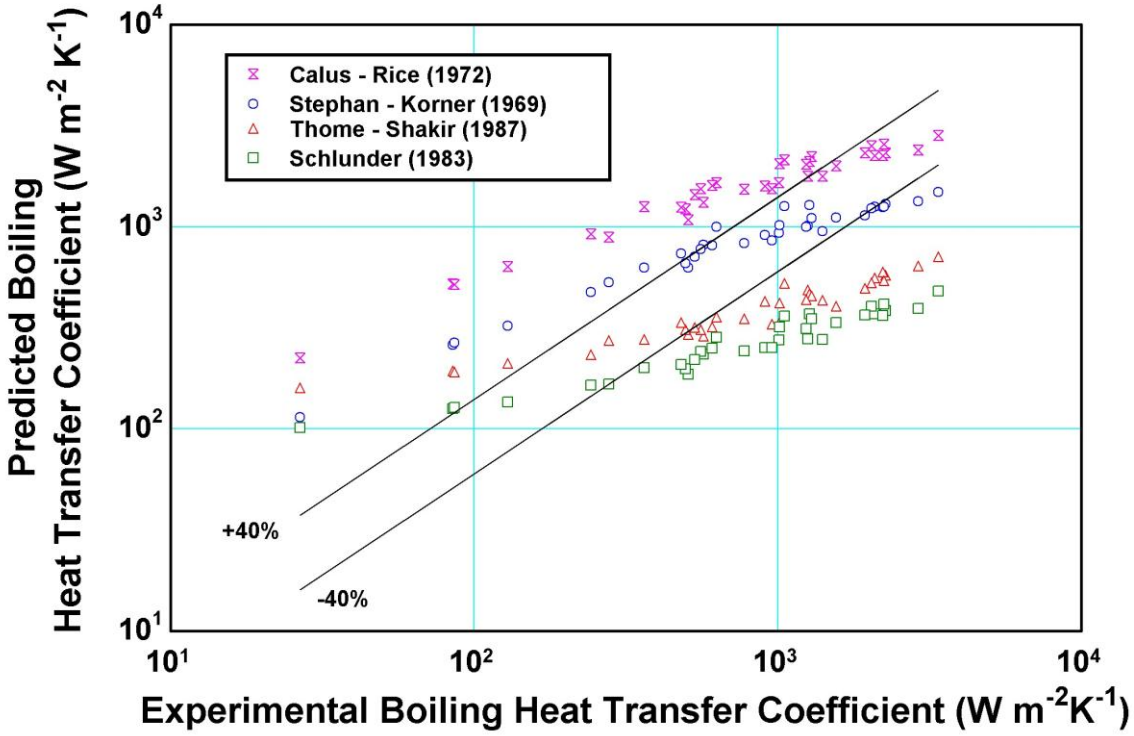

Figure 5.18: Various Multi-Component Correction Factors vs. Experimental Data

The pressure dependence in their correlation was empirically determined (Nahra and Naess 2009). Equation 5.25 presents the Stephan and Korner (1969) correction factor where A_o is a constant mixture-specific constant, set to 3.56.

$$\frac{h}{h_{id}} = \frac{1}{1+A_o\left(y_i - x_i\right)\left(0.88+0.12P_{Bar}\right)} \tag{5.25}$$

Schlunder (1983) developed a semi-empirical correction factor based on mass transfer film theory, where the vapor-to-solution interface is approximated as a plane wall, with the evaporating liquid flowing perpendicular to it. This correction factor is presented as Equation 5.26, where B_o is a parameter defined as 1, while β_l is the liquid mass transfer coefficient, defined by Schlunder (1983) as 2×10^{-4} m s^{-1}.

$$\frac{h}{h_{id}} = \left(\frac{h_{id}}{q''} \left(T_{Sat,NH_3} - T_{Sat,H_2O} \right) \left(y_i - x_i \right) \left[1 - \exp\left(\frac{B_o q''}{\rho_l h_{LV} \beta_l} \right) \right] \right)^{-1} \tag{5.26}$$

Thome and Shakir (1987) modified Schlunder's correlation by representing the property variation in the mixture using the temperature glide instead of the difference in saturation temperatures and concentrations (Nahra and Naess 2009). The Thome - Shakir correction factor is presented as Equation 5.27, where ΔT_{BP} is the temperature glide of the mixture; B_o and β_l are defined as in Equation 5.26.

$$\frac{h}{h_{id}} = \left(\frac{h_{id}}{q''} \Delta T_{BP} \left[1 - \exp\left(\frac{B_o q''}{\rho_l h_{LV} \beta_l} \right) \right] \right)^{-1} \tag{5.27}$$

The correlation of Calus and Rice (1972) relates the reduction of the heat transfer coefficient to the reduction of the bubble growth rate, and includes the ratio of thermal and mass diffusivities, as shown in Equation 5.28.

$$\frac{h}{h_{id}} = \left(\left[1 + \left(y_i - x_i \right) \left(\frac{\alpha_l}{D} \right)^{0.5} \right]^{0.7} \right)^{-1} \tag{5.28}$$

As evidenced from Figures 5.17 and 5.18, none of these four pool-boiling mixture correction factors, when applied to the Mostinski correlation for the pure component coefficients, adequately predict all of the data from this study.

To identify an existing correlation that could adequately predict the data from this study, three different pool-boiling correlations were used to compute the corresponding values for the pure components of the mixture. In addition to the Mostinski (1963) correlation, the pool-boiling correlations of Gorenflo (1997) and Nishikawa and Fujita (1977) were considered. Figures 5.19

and 5.20 present the predictions of these correlations with data. To provide a standard of comparison, the Stephan and Korner (1969) correction factor, which was recommended by Inoue *et al.* (2002), was used for all three correlations considered here.

All three of the pure component correlations considered correlate pool-boiling coefficients using both the pressure and heat flux raised to specified powers. Equations 5.29 - 5.31 present the Mostinski (1963), Gorenflo (1997) and Nishikawa and Fujita (1977) correlations, respectively.

Mostinski (1963)

$$h_{Component} = 4.17 \times 10^{3} P_{cr}^{\,0.69} q''^{0.7} F_p; \quad (5.29)$$

$$F_p = 1.8(p_r)^{0.17} + 4(p_r)^{1.2} + 10(p_r)^{10}; \quad \text{and } p_r = P/P_{cr}$$

Gorenflo (1997)

$$\frac{h_{component}}{h_o} = \left(\frac{q''}{q_o''}\right)^{n(p_r)} F(p_r) \quad (5.30)$$

For Ammonia

$$F(p_r) = 1.2 p_r^{\,0.27} + \left(2.5 + \frac{1}{1-p_r}\right) p_r; \quad n(p_r) = 0.9 - 0.3 p_r^{\,0.15}; \quad h_o = 7000$$

For Water

$$F(p_r) = 1.73 p_r^{\,0.27} + \left(6.1 + \frac{0.68}{1-p_r}\right) p_r^{\,2}; \quad n(p_r) = 0.9 - 0.3 p_r^{\,0.3}; \quad h_o = 5600$$

Nishikawa-Fujita (1977)

$$h_{component} = 0.3073\left[\left(\frac{P}{P_{ATM}}\right)^{0.23} \left(f_\xi q''\right)^{0.8}\right] \times 1/R^{0.2} \quad (5.31)$$

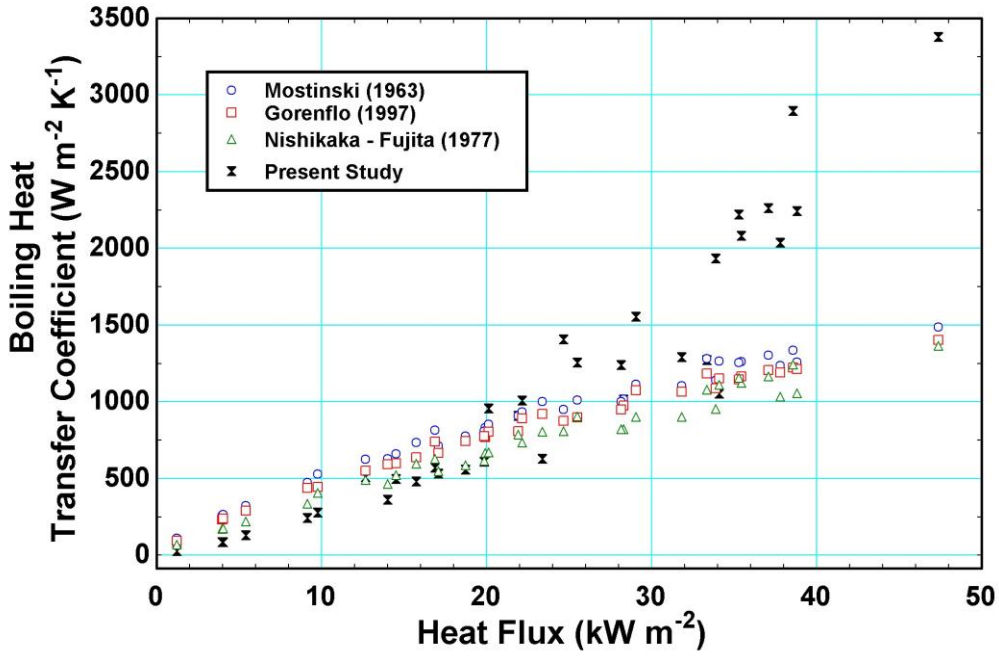

Figure 5.19: Three Pure Component Correlations with Stephan - Korner (1969) Correction. Predicted h vs. Flux

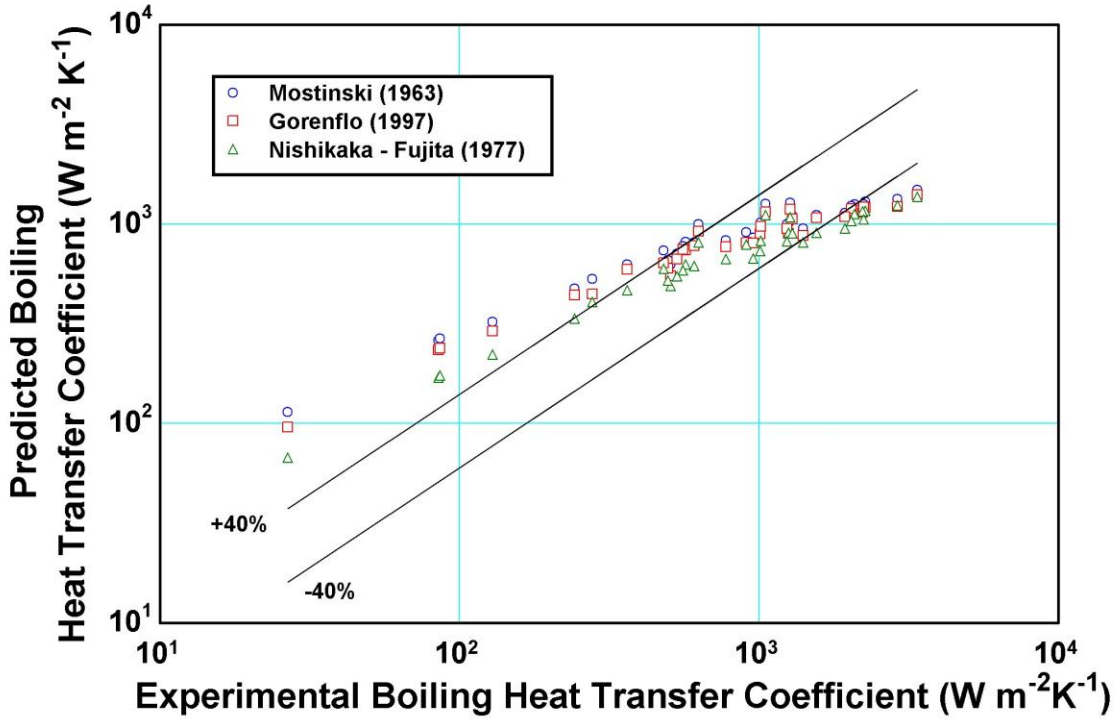

Figure 5.20: Three Pure Component Correlations with Stephan - Korner (1969) Correction. Predicted h vs. Experimental h

As shown in Figures 5.21 - 5.22, the three pure-component pool-boiling correlations are in general agreement; however, none of them adequately predicts all of the data from this study. All three correlations present the pool-boiling coefficient as proportional to the heat flux raised to some power, between 0.7 and 0.9. However, the data from the present study show a stronger flux dependence, where $h \propto q^{1.7}$. If either the pure component correlation or the correction factor were modified to incorporate this stronger flux dependence, the data can be accurately predicted.

Such a modification is presented as Equation 5.32. Here, the Thome and Shakir (1987) correlation has been modified by using an additional term, Cq''^{-1}; this modified correlation best fits the data when applied to the Mostinski correlation and with $C = 7.49$ kW m^{-2}. Figures 5.21 - 5.22 compare the data from this study with this modified correction factor applied to the Mostinski correlation.

$$\frac{h}{h_{id}} = \left(\left(\frac{C}{q''} \right) \frac{h_{id}}{q''} \Delta T_{BP} \left[1 - \exp\left(\frac{B_o q''}{\rho_l h_{LV} \beta_l} \right) \right] \right)^{-1} \tag{5.32}$$

This modified correlation fits the data with $R^2 = 0.93$ and an average absolute error of 18.9%. Figure 5.22 shows that, of the 35 data points considered, this modified correlation predicts 33 points within the ±40% error bands. Compared to the correction factors considered from the literature, the modified correlation more accurately captures the relationship between the applied heat flux and pool-boiling coefficient.

The poor agreement between the experimental pool-boiling coefficients from the present study and those predicted by the models from the literature implies that the heat transfer process occurring within the flooded column is not completely explained as simple pool boiling. This is

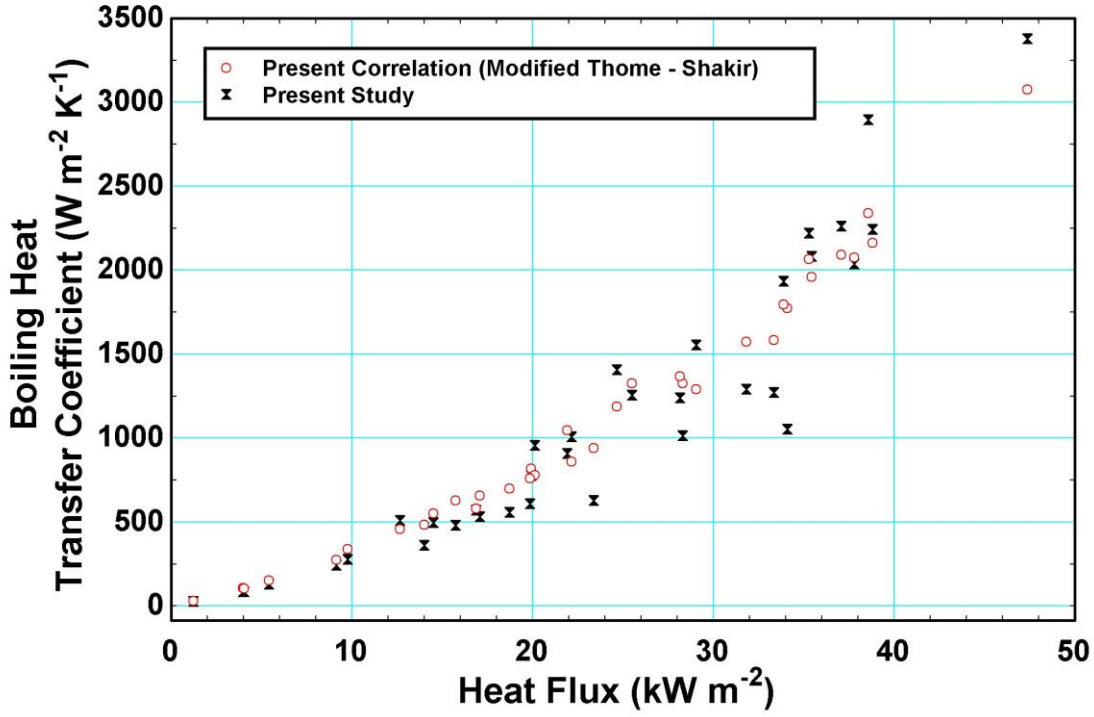

Figure 5.21: Correlation from Present Study (Modified Thome - Shakir): h vs. Flux

not surprising when considering the geometry of the test section: the spacing between the plates forming the column - 6.4 mm - is on the same order of magnitude as the bubble diameter - which was calculated to be approximately 3 mm in Chapter 3. These dimensions support the conclusions of the flow visualization studies - the pool-boiling region of the flooded column is marked by intense agitation of the liquid phase by the generated vapor stream. This agitation is likely stronger than is typical of the pool-boiling models considered from the literature, and could account for the increased heat transfer coefficients observed in this study.

While the boiling process within the component is not best described as simple pool boiling, it is adequately predicted by the modified correction factor, as demonstrated by Figures 5.21 -5.22. This modified correlation is based on data collected from experiments with heat fluxes ranging from 1.2 to 47.3 kW m^{-2}, system pressures between 410 and 1250 kPa, and heat transfer coefficients between 26.6 and 3378 W m^{-2} K^{-1}, and the applicability of this correlation is

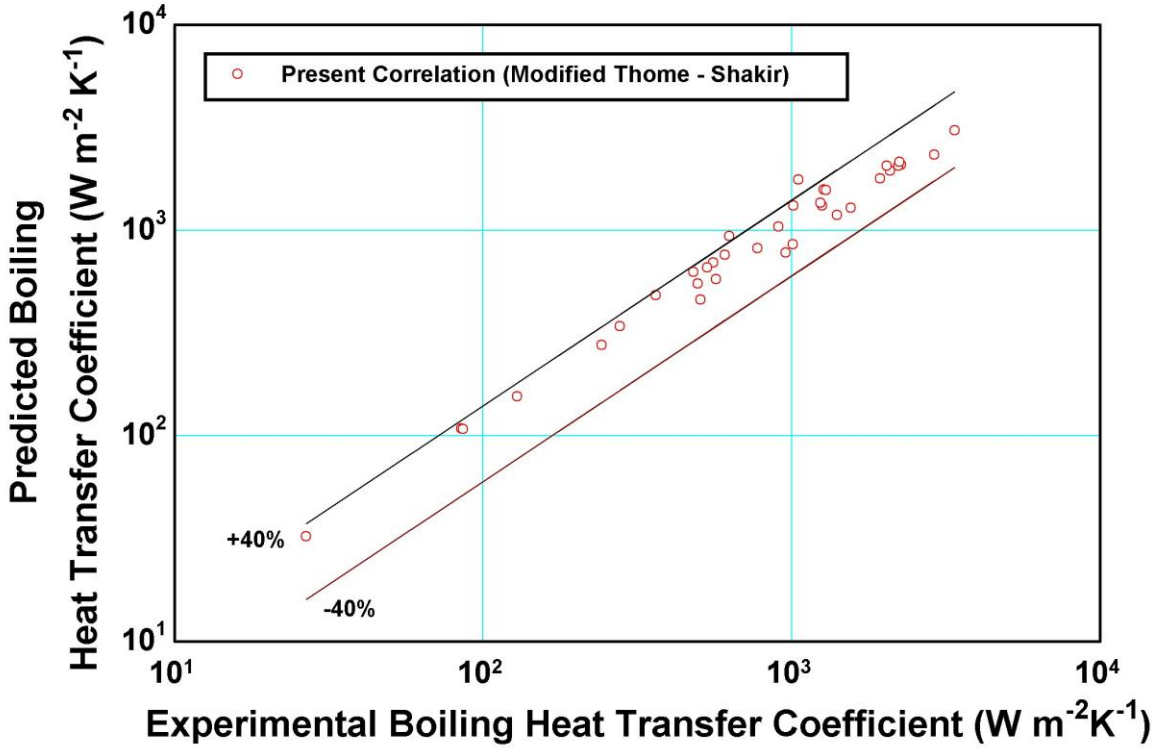

Figure 5.22: Correlation from Present Study (Modified Thome - Shakir): $h_{Predicted}$ vs. $h_{Experimental}$

limited to these ranges. Figure 5.23 presents a plot of the predictions of this modified correlation across this range of parameters. At constant solution concentration and temperature, the predictions of the heat transfer coefficient are presented as a function of the heat flux and system pressure. The system pressure was observed to have a slight inverse relationship with the predicted heat transfer coefficient. A similar analysis conducted by considering the predictions of the modified correlation for varying solution concentration showed that this parameter alone does not significantly influence the predicted heat transfer coefficient.

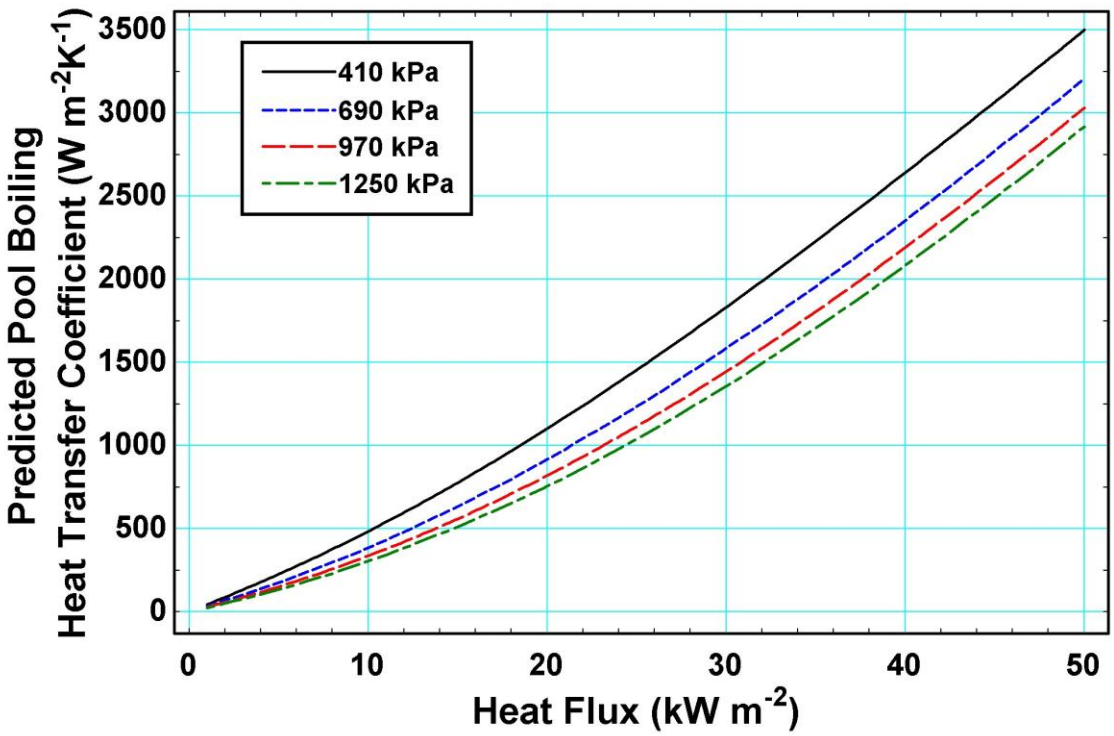

Figure 5.23: Heat Transfer Coefficient Predictions of the Modified Correlation as a function of Heat Flux and System Pressure

5.4 Uncertainty Analysis

The experimental uncertainties for the various measurement systems were reported in the discussion of the data reduction procedure. In addition to the uncertainties inherent to the measurement devices, the data reduction procedure itself propagates additional uncertainty. The procedure incorporates two heat transfer correlations, one for the analysis of single phase convection in the Paratherm microchannels and another for heat transfer to an evaporating falling film. As documented in Table 5.1, these correlations are assumed to carry uncertainties of 25%.

Uncertainty propagation calculations were conducted in Engineering Equation Solver (Klein 2009); the details of these calculations are reported in Appendix A. Figure 5.24 presents

the calculated experimental pool-boiling coefficients with error bars representing their uncertainty, while Figure 5.25 presents the uncertainty ratio, that is, $\text{Uncertainty}\left(h_{Experimental}\right)^{-1}$ as a function of the column height

The uncertainties of all of the calculated heat transfer coefficients are quite large; for many points, the uncertainty is over 200% of the calculated value. The calculations in Appendix A demonstrate that most significant source of experimental uncertainty is the falling-film heat transfer correlation; for the sample point considered in the development of the data reduction procedures, the falling-film correlation is responsible for 78% of the experimental uncertainty. The significance of the falling-film correlation is also demonstrated by considering Figure 5.25, a plot of the uncertainty ratio vs. column height. Clearly, the uncertainty ratio is a strong function of the column height. As the column height increases and the falling-film region - and thus the falling-film correlation - becomes less significant, the uncertainty ratio decreases. For instance, the points with column heights between 40 and 50 mm have an uncertainty ratio between 2 and 7, while the ratio decreases to less than 1 for points with column heights above 100 mm.

In the present study, the partially flooded condition seen in the experiments requires the data reduction procedure to include the analysis of the falling-film region. This aspect diminishes the significance of the flooded region in determining the overall heat transfer rates, which in turn increases the uncertainties due to the reliance on falling-film heat transfer correlations for determining the heat transferred in the pool-boiling region of interest here. Future experiments conducted under conditions that yield operation in a substantially pooling mode are expected to yield lower uncertainties than those seen in the present study.

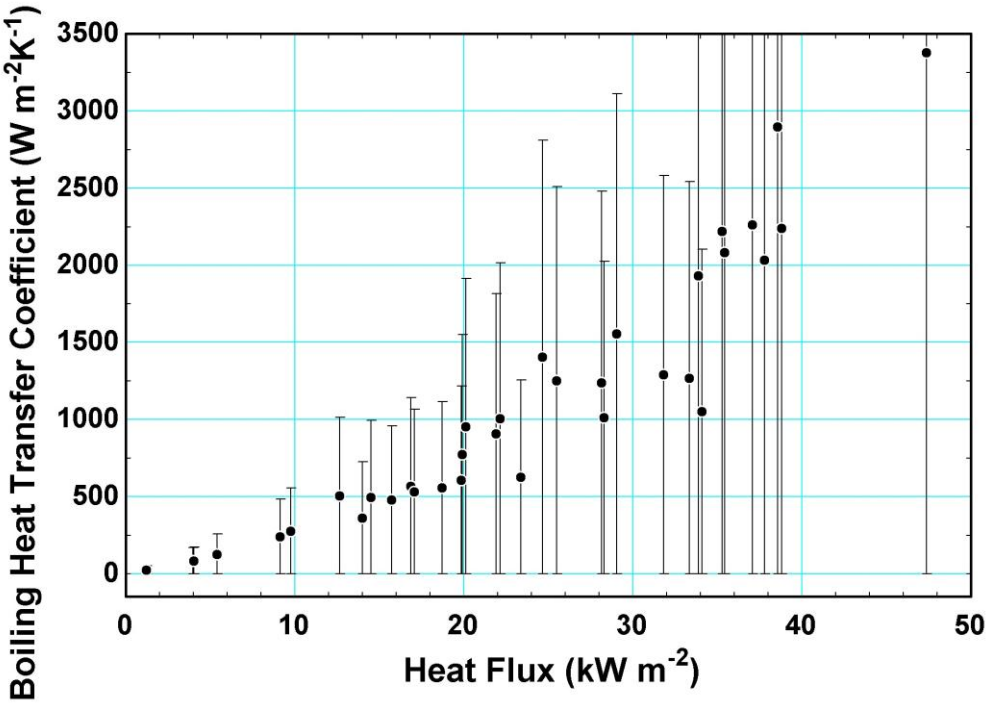

Figure 5.24: Experimental Pool Boiling Coefficients with Error Bars

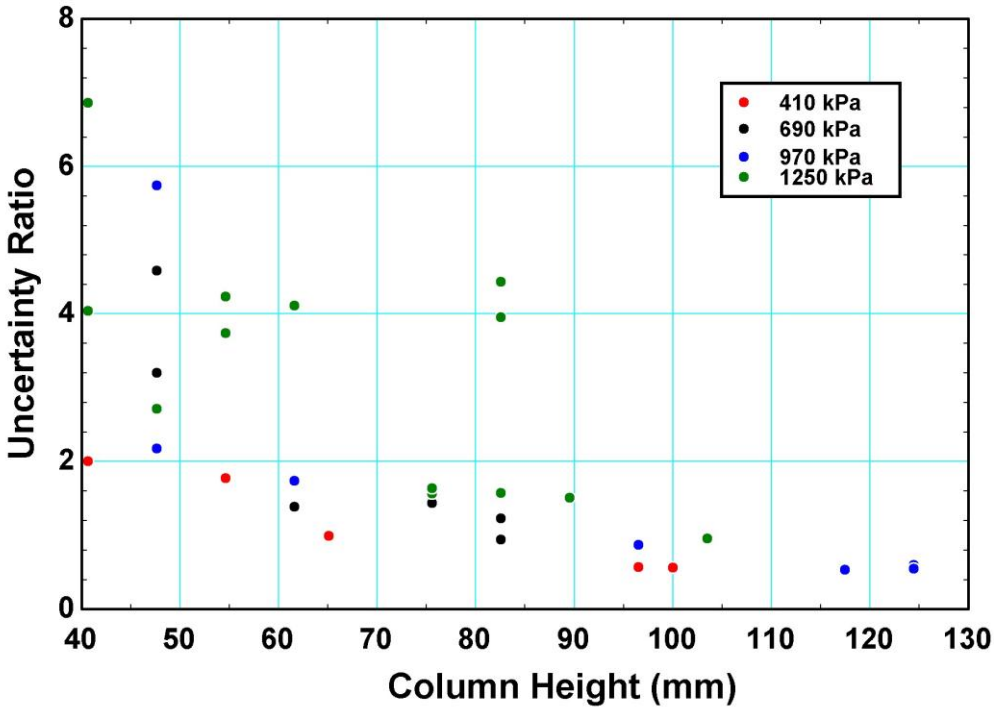

Figure 5.25: Uncertainty Ratio vs. Solution Column Height

CHAPTER 6: CONCLUSIONS AND RECOMMENDATIONS

This chapter provides a summary of the results and contributions of this research, and offers recommendations for continued investigation.

6.1 Summary of Results and Contributions

A novel counter-flow desorber for application in a micro-scale ammonia-water absorption system was investigated in this study. Several counterflow designs were considered, and the Flooded Column was selected as the focus of this investigation. In this component, ammonia-rich solution undergoes pool boiling to generate a refrigerant vapor stream. The geometry of the design allows for mixing between the vapor and solution streams, increasing the generated refrigerant purity by promoting inter-phase heat and mass transfer.

A combined heat and mass transfer model was developed to analyze the Flooded Column design. This model used an ammonia-water specific mixture pool-boiling correlation in a discretized geometry, where changes in the solution fluid properties and the respective heat transfer rates were tracked from segment to segment. This heat and mass transfer model demonstrated the viability of the design, and was employed as a design tool in the development of a prototype Flooded Column test section.

To further investigate the performance of the Flooded Column desorber, an experimental facility was developed for both flow visualization and heat and mass transfer experiments. Flow visualization experiments were used to observe the multi-phase flow phenomena in the counterflow desorber at operating conditions representative of absorption heat pumps. Heat and

mass transfer experiments and analysis yielded the transfer coefficients at these conditions, which were subsequently used for correlation development.

Flow visualization tests confirmed the turbulent nature of the pool-boiling process; vigorous mixing was observed between the vapor and solution phases. This mixing, a key element of this Flooded Column design, ensures efficient heat and mass transfer between the two phases, increasing the refrigerant content of the generated vapor stream. Flow visualization studies also revealed that the solution level within the Flooded Column is dependent on an interconnected set of system parameters that must be carefully controlled. The component operated most stably in a partially flooded condition, where both falling-film and pool-boiling regions contribute to the heat transfer process.

Heat and mass transfer experiments were conducted on the component in this partially flooded condition. Experiments were conducted at four system pressures between 410 to 1250 kPa, and the heat flux applied to the boiling region ranged from 1.2 to 47.3 kW m^{-2}. The pool-boiling contribution to the overall heat transfer was used to obtain heat transfer coefficients for this region; these heat transfer coefficients ranged from 26.6 to 3378 W m^{-2} K^{-1}. The experimental uncertainties accompanying these heat transfer coefficients were quite large, ranging between 30% and 680% of the calculated values. A major portion of this uncertainty can be traced to the falling-film heat transfer coefficient used to obtain the heat transferred in the pool-boiling region of the test section. Therefore, while the results and the correlations from the present study offer some guidance on flooded column heat and mass transfer, the level of confidence that can be placed in their predictive ability, especially for conditions outside the range under which the experiments were conducted, is low. Tests conducted with a much larger portion of the test section in the pool-boiling mode would yield higher accuracies and lower

uncertainties in the heat transfer coefficients, leading to more reliable correlations. However, the results from the present study represent a first step in modeling flooded column desorbers for heat pumping applications, in which the components are likely to operate at least with some portion of the component being in the falling-film mode.

The heat and mass transfer experiments demonstrated a strong dependence between the heat transfer coefficient and the applied heat flux; for a given system pressure, the heat transfer coefficient varied nearly linearly with heat flux. The heat transfer coefficients were compared with several multi-component pool-boiling models from the literature; however, none successfully fit all of the data from this study. The pool-boiling coefficients in the Flooded Column were shown to depend more strongly on the applied heat flux than anticipated by the models. The correlation of Thome and Shakir (1987) was modified by incorporating an additional term to account for this stronger dependence on heat flux. This modified correlation fits the data from this study within an average absolute error of 19%, and is applicable within the range of conditions tested.

While the disparity between the data and the mixture correlations demonstrate that the heat transfer process within the component deviates from predictions based on pool boiling, this should not be surprising. The confined boiling process observed within the desorber is a departure from the less agitated conditions used to develop the widely used mixture pool-boiling correlations.

6.2 Evaluations and Recommendations

The heat and mass transfer experiments conducted here showed that pool boiling within the component was more effective than anticipated by the mixture boiling models; for large

applied heat fluxes, the calculated experimental values were larger than those predicted. At the highest applied heat fluxes, the experimental heat transfer coefficients from this study ranged up to 120% higher than the values predicted by the Mostinski (1963) correlation and the Stephan and Korner (1969) correction factor. While this is encouraging, the limitations of the design were documented through the flow visualization efforts. The unstable behavior of the solution level within the component markedly influences the performance of the desorber, and presents system-level implications. A successful and reliable desorber design should be able to account for variations in system pressure, flowrate and heat duty without fundamental changes in performance. To perform well across such variations, the Flooded Column desorber should be modified to either prevent the partially flooded condition, or should be designed to account for this mode of operation.

Analysis of the data from this study shows that the falling-film boiling process is much more efficient than pool boiling. For the data points collected, the falling-film heat transfer coefficients, as calculated from the Chun and Seban (1971) turbulent correlation, are between 2500 and 6500 W m^{-2} K^{-1}. The experimental pool-boiling heat transfer coefficients for these data are between 100 and 3500 W m^{-2} K^{-1}. The Flooded Column desorber, relying primarily on pool boiling, was selected in spite of the fact that superior rates of heat transfer are observed in falling films; the high rates of inter-phase heat and mass transfer in the pool-boiling region, and the simplicity of design and fabrication make it an attractive design. However, if it must operate in a partially flooded condition, the component should be designed to maximize the effectiveness of the falling-film portion. In the present design, the solution is introduced through one port at the top of the column, and forms a narrow rivulet, decreasing the effective transfer area. Introducing

the solution across the entire width of the column, thus using all of the channel width in the falling-film region, would increase the efficacy of the design.

Other desorber designs incorporating the beneficial aspects of both falling-film and pool boiling can be envisioned. The Staggered Tray design, presented in Chapter 1 (Figure 1.9) could be particularly attractive. In this component, the solution undergoes pool boiling in several alternating trays. As the solution overflows from each successive tray and flows along the channel surface, it also experiences falling-film evaporation. This design potentially presents an optimal balance between the high-flux falling-film process, and the vapor-purity-promoting pool boiling process. Because it is not intended to operate in the flooded condition, it could experience a lesser degree of solution level instabilities that hamper the Flooded Column.

The utility of the experimental apparatus developed and fabricated here will be demonstrated as it is used for subsequent investigations into other desorber designs, such as the Staggered Tray. The experimental procedures developed and experience gained while carrying out these investigations offer additional guidance about potential modifications to the apparatus to facilitate future testing.

To reduce experimental uncertainties, the test section itself should be instrumented for more detailed temperature measurements, especially in the Paratherm coupling fluid channels. In the present study, a complicated data analysis procedure was required to calculate the pool-boiling heat transfer coefficients from the measured parameters; by relying on a heat transfer correlation from the literature to determine the heat flux into both segments of the desorber, this procedure significantly increased the experimental uncertainty. Intermediate temperature measurements within the coupling fluid channels would allow for direct calculation of the heat

flux along the length of the component, and would considerably decrease experimental uncertainties. If further precision is required, subsequent test sections can be electrically heated to provide more accurate heat duty measurements.

Additionally, the facility should be configured to allow accurate evaluation of the vapor generation rate. While temperatures and pressures - and thereby concentrations - can be readily determined for all points with the existing instrumentation, the flowrates characterizing the desorber performance are more difficult to determine. Liquid flowrates for both the concentrated and dilute solution are readily available, but the flowrate of the generated vapor stream is currently not measured. It was intended to calculate the vapor flowrate from the two measured liquid flowrates and a mass balance on the desorber, but the large volume of the pressure vessel precludes the required steady state operation. To accurately measure the vapor flowrate, the refrigerant should be condensed before measurement in a liquid flowmeter. While the components for this measurement were not included in the original facility design, they would provide useful information for future desorber design evaluation.

APPENDIX A: UNCERTAINTY ANALYSIS

Uncertainties in the heat transfer coefficients obtained in this study were estimated using an error propagation approach implemented in Engineering Equation Solver Software (Klein, 2009). To illustrate the propagation of uncertainties, sample calculations are presented here. Uncertainties are denoted by a U with the appropriate subscript; for example, the uncertainty in the experimental pool-boiling heat transfer coefficient is labeled $U_{h_{PB,Experimental}}$. The sample calculations reported below are for the data point from 3:51 PM on December 22, which was also used as the basis for the discussion of the data analysis procedure in Chapter 5. The

Table A.1: Sample Point Measurements

Measurand	Value	Units	Measurand	Value	Units
$T_{Coupling\ Fluid,\ Inlet}$	136.9	°C	$V_{Coupling\ Fluid}$	398.2	mL/min
$T_{Coupling\ Fluid,\ Outlet}$	89.3	°C	$m_{Solution}$	292.6	g/min
$T_{solution,\ Inlet}$	38.9	°C	P_{High}	846	kPa
$T_{Solution,\ Boiling,\ Average}$	88.2	°C	$L_{Boiling}$	97	mm
22 December, 3:51			$Width_{Falling\ Film}$	12	mm

Table A.2: Measurement Uncertainties

Measurand	Manufacturer	Model #	Uncertainty
$T_{Coupling\ Fluid,\ Inlet}$	Omega	Type-T TC	0.5°C
$T_{Coupling\ Fluid,\ Outlet}$	Omega	Type-T TC	0.5°C
$T_{solution,\ Inlet}$	Omega	Type-T TC	0.5°C
$T_{Solution,\ Boiling,\ Average}$	Omega	Type-T TC	0.5°C
$V_{Coupling\ Fluid}$	AW-Lake	JVS-20KG	0.5% of Reading
$m_{Solution}$	Rheonik	RHM 015	0.15% of Reading
P_{High}	Wika	A-10	1% of Range

Correlations		
Microchannel Heat Transfer	Sparrow and Haji-Sheikh (1965)	25%
Falling Film Heat Transfer	Chun and Seban (1971)	25%

measured values from this data point are presented again, in Table A.1, while the uncertainties in these measurements are reported again in Table A.2.

Chapter 5 details the data analysis procedure used to calculate the experimental heat transfer coefficient from the measured quantities. This procedure uses a resistance network analysis between the average coupling fluid temperature in the boiling region, and the average solution temperature in the boiling region to determine the pool-boiling heat transfer coefficient. The amount of heat transferred through the boiling region, $Q_{PoolBoiling}$, is calculated from the closed model. The uncertainty in this heat duty, $U_{Q_{PoolBoiling}}$, is a function of the measured parameters listed in Table A.2. This uncertainty is calculated using Equation A.1.

$$\begin{aligned}\left(U_{Q_{PoolBoiling}}\right)^2 = &\left(U_{\alpha_{CF}}\frac{\partial Q_{PoolBoiling}}{\partial \alpha_{CF,FF}}\right)^2 + \left(U_{\alpha_{FallingFilm}}\frac{\partial Q_{PoolBoiling}}{\partial \alpha_{CF,PB}}\right)^2 + \left(U_{Height}\frac{\partial Q_{PoolBoiling}}{\partial Height}\right)^2 \\ &+ \left(U_{L_{Boiling}}\frac{\partial Q_{PoolBoiling}}{\partial L_{Boiling}}\right)^2 + \left(U_{T_{CF,Inlet}}\frac{\partial Q_{PoolBoiling}}{\partial T_{CF,Inlet}}\right)^2 + \left(U_{T_{CF,Outlet}}\frac{\partial Q_{PoolBoiling}}{\partial T_{CF,Outlet}}\right)^2 \\ &+ \left(U_{T_{Solution,Inlet}}\frac{\partial Q_{PoolBoiling}}{\partial T_{Solution,Inlet}}\right)^2 + \left(U_{V_{CF}}\frac{\partial Q_{PoolBoiling}}{\partial \dot{V}_{CF}}\right)^2\end{aligned} \quad \text{(A.1)}$$

For the sample point considered, values for the parameter uncertainties and partial derivatives are presented in Table A.3. For this point, $U_{Q_{PoolBoiling}} = \pm 91.22$ W or $\pm 41.5\%$.

Table A.3: Parameter Uncertainties and Partial Derivatives for $UQ_{Pool\ Boiling}$ Calculation

$\frac{dQ_{PoolBoiling}}{d\alpha_{CF}}$	0.0001115	$\frac{dQ_{PoolBoiling}}{dHeight}$	0.07018	$\frac{dQ_{PoolBoiling}}{dT_{CF,Inlet}}$	0.007269	$\frac{dQ_{PoolBoiling}}{dT_{Solution,Inlet}}$	0.004419
$U\alpha_{CF}$	236.6	$UHeight$	0.1054	$UT_{CF,Inlet}$	0.9	$UT_{Solution,Inlet}$	0.9
$\frac{dQ_{PoolBoiling}}{d\alpha_{Falling\ Film}}$	0.00008465	$\frac{dQ_{PoolBoiling}}{dL_{Boiling}}$	0.07018	$\frac{dQ_{PoolBoiling}}{dT_{CF,Outlet}}$	0.0109	$\frac{dQ_{PoolBoiling}}{dV_{CF}}$	0.001756
$U\alpha_{Falling\ Film}$	1016	$UL_{Boiling}$	0.038	$UT_{CF,Outlet}$	0.9	UV_{CF}	1.991

Similarly, the average temperature of the coupling fluid in the boiling region, $T_{CF,Ave,PB}$, is calculated from the closed model. The uncertainty in this temperature, $U_{T_{CF,Ave,PB}}$, is also a function of the measured parameters listed in Table A.2, and is calculated using Equation A.2.

$$\begin{aligned}\left(U_{T_{CF,Ave,PB}}\right)^2 = &\left(U_{\alpha_{CF}}\frac{\partial T_{CF,Ave,PB}}{\partial \alpha_{CF,FF}}\right)^2 + \left(U_{\alpha_{FallingFilm}}\frac{\partial T_{CF,Ave,PB}}{\partial \alpha_{CF,PB}}\right)^2 + \left(U_{Height}\frac{\partial T_{CF,Ave,PB}}{\partial Height}\right)^2 \\ &+ \left(U_{L_{Boiling}}\frac{\partial T_{CF,Ave,PB}}{\partial L_{Boiling}}\right)^2 + \left(U_{T_{CF,Inlet}}\frac{\partial T_{CF,Ave,PB}}{\partial T_{CF,Inlet}}\right)^2 + \left(U_{T_{CF,Outlet}}\frac{\partial T_{CF,Ave,PB}}{\partial T_{CF,Outlet}}\right)^2 \\ &+ \left(U_{T_{Solution,Inlet}}\frac{\partial T_{CF,Ave,PB}}{\partial T_{Solution,Inlet}}\right)^2 + \left(U_{V_{CF}}\frac{\partial T_{CF,Ave,PB}}{\partial \dot{V}_{CF}}\right)^2\end{aligned} \qquad \text{(A.2)}$$

For the sample point considered, values for the parameter uncertainties and partial derivatives are presented in Table A.4. For this point, $U_{T_{CF,Ave,PB}} = \pm 3.56^{\circ}\text{C}$

Table A.4: Parameter Uncertainties and Partial Derivatives for $U_{T_{CF,Ave,PB}}$ Calculation

$\frac{dT_{CF,Ave,PB}}{d\alpha_{CF}}$	0.004361	$\frac{dT_{CF,Ave,PB}}{dHeight}$	2.745	$\frac{dT_{CF,Ave,PB}}{dT_{CF,Inlet}}$	0.2778	$\frac{dT_{CF,Ave,PB}}{dT_{Solution,Inlet}}$	0.1729
$U_{\alpha_{CF}}$	236.6	U_{Height}	0.1054	$U_{T_{CF,Inlet}}$	0.9	$U_{T_{Solution,Inlet}}$	0.9
$\frac{dT_{CF,Ave,PB}}{d\alpha_{Falling\ Film}}$	0.003312	$\frac{dT_{CF,Ave,PB}}{dL_{Boiling}}$	2.746	$\frac{dT_{CF,Ave,PB}}{dT_{CF,Outlet}}$	0.4262	$\frac{dT_{CF,Ave,PB}}{d\dot{V}_{CF}}$	0.04713
$U_{\alpha_{Falling\ Film}}$	1016	$U_{L_{Boiling}}$	0.038	$U_{T_{CF,Outlet}}$	0.9	$U_{\dot{V}_{CF}}$	1.991

The total thermal resistance in the boiling region between the coupling fluid and the solution is calculated using Equation 5.18, as shown below.

$$Q_{\text{Pool Boiling}} = \left(T_{CF,Ave,PB} - T_{Solution,Ave,PB}\right) \cdot \frac{1}{R_{Total}} \qquad (5.18)$$

The uncertainty in this total thermal resistance is a function of $T_{CF,Ave,PB}$, $T_{Solution,Ave,PB}$, and $Q_{PoolBoiling}$, and is calculated using Equation A.3:

$$\left(U_{R_{Total}}\right)^2 = \left(U_{T_{CF,Ave,PB}} \frac{\partial R_{Total}}{\partial T_{CF,Ave,PB}}\right)^2 + \left(U_{T_{Solution,Ave,PB}} \frac{\partial R_{Total}}{\partial T_{Solution,Ave,PB}}\right)^2 + \left(U_{Q_{PoolBoiling}} \frac{\partial R_{Total}}{\partial Q_{PoolBoiling}}\right)^2 \quad \text{(A.3)}$$

Differentiating Equation 5.20 yields this formulation for $U_{R_{Total}}$:

$$\left(U_{R_{Total}}\right)^2 = \left(U_{T_{CF,Ave,PB}} \frac{1}{Q_{PoolBoiling}}\right)^2 + \left(U_{T_{Solution,Ave,PB}} \frac{1}{Q_{PoolBoiling}}\right)^2 + \left(U_{Q_{PoolBoiling}} \frac{R_{Total}}{Q_{PoolBoiling}}\right)^2$$

For the sample point considered, $Q_{PoolBoiling} = 219.5$ W and $R_{Total} = 0.1835$ K W^{-1}. The uncertainties $U_{T_{CF,Ave,PB}}$ and $U_{Q_{PoolBoiling}}$ were calculated above, and $U_{T_{Solution,Ave,PB}} = 0.5^{\circ}$C, as reported in Table A.2:

$$\left(U_{R_{Total}}\right)^2 = \left(\left(3.56^{\circ}C\right)\frac{1}{219.5\text{ W}}\right)^2 + \left(\left(0.5^{\circ}C\right)\frac{1}{219.5\text{ W}}\right)^2 + \left(\left(91.22\text{ W}\right)\frac{0.1835\text{ K W}^{-1}}{219.5\text{ W}}\right)^2$$

Thus, for the sample point considered, $U_{R_{Total}} = \pm 0.07799$ K W^{-1} or $\pm 42.5\%$.

The uncertainties in the microchannel convection and conduction resistances are also required to evaluate $U_{h_{PB,Exp}}$. The convection resistance within the coupling fluid microchannel is calculated from Equation 5.20, as shown:

$$R_{Convection} = \frac{1}{h_{CF,PB} A_{CF,PB} \eta_T} \quad (5.20)$$

The uncertainty in this thermal resistance is calculated from the uncertainty associated with the microchannel convection correlation, and $U_{L_{Boiling}}$, which influences the area term, as shown in Equation A.4.

$$\left(U_{R_{Convection}}\right)^2 = \left(U_{L_{Boiling}} \frac{\partial R_{Convection}}{\partial L_{Boiling}}\right)^2 + \left(U_{h_{CF,PB}} \frac{\partial R_{Convection}}{\partial h_{CF,PB}}\right)^2 \quad \text{(A.4)}$$

Differentiating Equation 5.23 yields this formulation for $U_{R_{Convection}}$:

$$\left(U_{R_{Convection}}\right)^2 = \left(U_{L_{Boiling}} \left(R_{Convection} \frac{1}{L_{Boiling}}\right)\right)^2 + \left(U_{h_{CF,PB}} \left(R_{Convection} \frac{1}{h_{CF,PB}}\right)\right)^2$$

$U_{L_{Boiling}}$ and $U_{h_{CF,PB}}$ are replaced with the relative uncertainties from Table A.2:

$$\left(U_{R_{Convection}}\right)^2 = \left((0.01) L_{Boiling} \left(R_{Convection} \frac{1}{L_{Boiling}}\right)\right)^2 + \left((0.25) h_{CF,PB} \left(R_{Convection} \frac{1}{h_{CF,PB}}\right)\right)^2$$

$$\left(U_{R_{Convection}}\right)^2 = \left((0.01) R_{Convection}\right)^2 + \left((0.25) R_{Convection}\right)^2$$

For the sample point considered, $R_{Convection} = 0.0651 \text{ K W}^{-1}$ and

$U_{R_{Convection}} = \pm 0.01628 \text{ K W}^{-1}$ or $\pm 25.0\%$.

The conduction resistance is calculated using Equation 5.22, as shown below:

$$R_{Conduction} = \frac{\delta_{Wall}}{k_{Wall} A_{Wall,Pool\ Boiling}} \quad \text{(5.22)}$$

The uncertainty in this resistance term is a function of the heat transfer area in the pool-boiling region, $A_{Wall,Pool\ Boiling}$, as shown below in Equation A.5:

$$\left(U_{R_{Conduction}}\right)^2 = \left(U_{A_{Wall,PoolBoiling}} \frac{\partial R_{Conduction}}{\partial A_{Wall,PoolBoiling}}\right)^2 \quad \text{(A.5)}$$

The uncertainty in the heat transfer area term, $A_{Wall,Pool\ Boiling}$, is a function of the measured solution level, and is calculated using Equation A.6:

$$\left(U_{A_{Wall,PoolBoiling}}\right)^2 = \left(U_{L_{Boiling}} \frac{\partial A_{Wall,PoolBoiling}}{\partial L_{Boiling}}\right)^2 \tag{A.6}$$

Differentiating and applying the relative uncertainty from Table A.2 for $U_{L_{Boiling}}$ yields:

$$\left(U_{A_{Wall,PoolBoiling}}\right)^2 = \left((0.01)\, L_{Boiling} \bullet Width\right)^2$$

For the sample point considered, $L_{Boiling} = 0.09652$ m and $Width = 0.1143$ m. Thus, $\left(U_{A_{Wall,PoolBoiling}}\right)^2 = \left((0.01)(0.09652\text{ m})(0.1143\text{ m})\right)^2$, and $U_{A_{Wall,PoolBoiling}} = \pm 0.0001103\text{ m}^2$. This uncertainty is used in Equation A.5. Differentiating Equation 5.23, Equation A.5 is simplified:

$$\left(U_{R_{Conduction}}\right)^2 = \left(\left(0.0001103\text{ m}^2\right)\left(\frac{R_{Conduction}}{A_{Wall,PoolBoiling}}\right)\right)^2$$

For the sample point considered, $R_{Conduction} = 0.001583\text{ K W}^{-1}$ and $A_{Wall,PoolBoiling} = 0.01103\text{ m}^2$. Thus, $U_{R_{Conduction}} = \pm 0.00001583\text{ K W}^{-1}$ or $\pm 1\%$.

$$\left(U_{R_{Conduction}}\right)^2 = \left(\left(0.0001103\text{ m}^2\right)\left(\frac{0.001583\text{ K W}^{-1}}{0.01103\text{ m}^2}\right)\right)^2$$

With the uncertainty in the total thermal resistance between the coupling fluid and solution in the pool-boiling region, as well as the uncertainties in the microchannel convection and conduction resistances, determined, the uncertainty in the pool-boiling resistance can be calculated. Equation 5.19 is used to calculate the pool-boiling thermal resistance.

$$R_{Pool\ Boiling} = R_{Total} - R_{Convection} - R_{Conduction} \tag{5.19}$$

The uncertainty in the pool-boiling resistance, $\boldsymbol{U}_{\boldsymbol{R}_{\boldsymbol{PoolBoiling}}}$, is calculated using Equation A.7:

$$\left(\boldsymbol{U}_{\boldsymbol{R}_{\boldsymbol{PoolBoiling}}}\right)^2 = \left(\boldsymbol{U}_{\boldsymbol{R}_{\boldsymbol{Total}}} \frac{\partial \boldsymbol{R}_{\boldsymbol{PoolBoiling}}}{\partial \boldsymbol{R}_{\boldsymbol{Total}}}\right)^2 + \left(\boldsymbol{U}_{\boldsymbol{R}_{\boldsymbol{Convection}}} \frac{\partial \boldsymbol{R}_{\boldsymbol{PoolBoiling}}}{\partial \boldsymbol{R}_{\boldsymbol{Convection}}}\right)^2 + \left(\boldsymbol{U}_{\boldsymbol{R}_{\boldsymbol{Conduction}}} \frac{\partial \boldsymbol{R}_{\boldsymbol{PoolBoiling}}}{\partial \boldsymbol{R}_{\boldsymbol{Conduction}}}\right)^2 \quad \text{(A.7)}$$

Differentiating Equation 5.21 yields:

$$\left(\boldsymbol{U}_{\boldsymbol{R}_{\boldsymbol{PoolBoiling}}}\right)^2 = \left(\boldsymbol{U}_{\boldsymbol{R}_{\boldsymbol{Total}}}\right)^2 + \left(\boldsymbol{U}_{\boldsymbol{R}_{\boldsymbol{Convection}}}\right)^2 + \left(\boldsymbol{U}_{\boldsymbol{R}_{\boldsymbol{Conduction}}}\right)^2$$

The previously calculated resistance uncertainties are applied. For the sample point considered, $\boldsymbol{U}_{\boldsymbol{R}_{\boldsymbol{PoolBoiling}}} = \pm 0.07967 \text{ K W}^{-1}$ or $\pm 68.2\%$.

$$\left(\boldsymbol{U}_{\boldsymbol{R}_{\boldsymbol{PoolBoiling}}}\right)^2 = \left(0.07799 \text{ K W}^{-1}\right)^2 + \left(0.01628 \text{ K W}^{-1}\right)^2 + \left(0.00001583 \text{ K W}^{-1}\right)^2$$

Having determined the uncertainty in the pool-boiling resistance, the uncertainty in the pool-boiling heat transfer coefficient can be determined. The heat transfer coefficient is calculated from the resistance and the heat transfer area using Equation 5.24.

$$\mathrm{R}_{\text{Pool Boiling}} = \frac{1}{\mathrm{h}_{\text{PB,Experimental}} \mathrm{A}_{\text{Wall,PB}}} \quad (5.24)$$

The uncertainty in the experimental heat transfer coefficient, $\boldsymbol{h}_{\boldsymbol{PB,Exp}}$, is calculated using Equation A.8.

$$\left(\boldsymbol{U}_{\boldsymbol{h}_{\boldsymbol{PB,Exp}}}\right)^2 = \left(\boldsymbol{U}_{\boldsymbol{R}_{\boldsymbol{PoolBoiling}}} \frac{\partial \boldsymbol{h}_{\boldsymbol{PB,Exp}}}{\partial \boldsymbol{R}_{\boldsymbol{PoolBoiling}}}\right)^2 + \left(\boldsymbol{U}_{\boldsymbol{A}_{\boldsymbol{Wall,PoolBoiling}}} \frac{\partial \boldsymbol{h}_{\boldsymbol{PB,Exp}}}{\partial \boldsymbol{A}_{\boldsymbol{Wall,PoolBoiling}}}\right)^2 \quad \text{(A.8)}$$

Differentiating Equation 5.27 yields:

$$\left(U_{h_{PB,Exp}}\right)^2 = \left(U_{R_{PoolBoiling}} \frac{1}{R_{PoolBoiling}{}^2 A_{Wall,PoolBoiling}}\right)^2 + \left(U_{A_{Wall,PoolBoiling}} \frac{1}{A_{Wall,PoolBoiling}{}^2 R_{PoolBoiling}}\right)^2$$

For the data point considered, $R_{PoolBoiling} = 0.1168 \pm 0.07967 \text{ K W}^{-1}$ and

$A_{Wall,PoolBoiling} = 0.01103 \pm 0.0001103 \text{ m}^2$. Thus, $U_{h_{PB,Exp}} = \pm 529.5 \text{ W m}^{-2}\text{K}^{-1}$ or $\pm 68.25\%$.

$$\left(U_{h_{PB,Exp}}\right)^2 = \left(0.07967 \text{ K W}^{-1} \frac{1}{\left(0.1168 \text{ K W}^{-1}\right)^2 0.01103 \text{ m}^2}\right)^2 + \left(0.0001103 \text{ m}^2 \frac{1}{\left(0.01103 \text{ m}^2\right)^2 0.1168 \text{ K W}^{-1}}\right)^2$$

For the data point considered, $h_{PB,Exp.} = 775.8 \pm 529.5 \text{ W m}^{-2}\text{K}^{-1}$

or $775.8 \pm 68.2\% \text{ W m}^{-2}\text{K}^{-1}$.

The uncertainties in the experimental pool-boiling heat transfer coefficients from this study ranged from 29% to 686% of the calculated values, with an average uncertainty of 270 %.

The uncertainty analysis conducted using Engineering Equation Solver (Klein, 2009) identifies the two heat transfer coefficients as the largest sources of uncertainty. For the sample point considered, the falling-film heat transfer coefficient is responsible for 78.1% of the calculated uncertainty, while the microchannel convection heat transfer correlation causes an additional 19.9%. The uncertainties from all of the remaining measurements combine for the remaining 2%.

APPENDIX B: FIN EFFICIENCY CALCULATIONS

The heat and mass transfer model presented in Chapter 3 and the data reduction procedure presented in Chapter 5 both employ resistance network calculations to model the thermal pathway between the coupling fluid and the solution. The calculations for the convection resistance within the coupling fluid microchannels account for temperature gradients within the microchannel shim by introducing an array efficiency, η_T. To determine this efficiency, the microchannel shim is modeled as an array of fins. The total efficiency of the array is related to the efficiency of the individual fin by Equation B.1, where r_{Curve} is the channel radius of curvature, as shown in Figure B.1.

$$\eta_T = 1 - \frac{A_F}{A_T}\left(1-\eta_F\right) \qquad \text{where} \quad \frac{A_F}{A_T} \propto \frac{\pi \bullet r_{Curve}}{\pi \bullet r_{Curve} + 2 \bullet r_{Curve}} \tag{B.1}$$

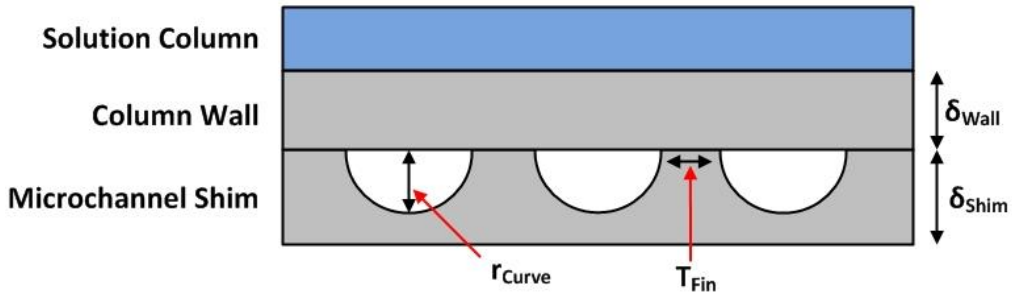

Figure B.1: Microchannel Geometry Schematic

If the individual fin is modeled as a fin with an insulated end, Equation B.2 provides the individual fin efficiency, η_F, where k_{Wall} is the thermal conductivity of the shim material, t_{Fin} is the fin thickness, and L_{Fin} is the fin length.

$$\eta_F = \frac{\mathrm{Tanh}\left(mL_{Fin}\right)}{mL_{Fin}}$$
$$\text{where} \quad m = \sqrt{\frac{k \bullet L_{Fin} t_{Fin}}{h_{CF}\left(\pi \bullet r_{Curve} + 2 \bullet r_{Curve}\right)}} \tag{B.2}$$

For the sample point considered in the data reduction procedure in Chapter 5, $L_{Fin} = \left(\text{Height-}L_{Boiling}\right) = \left(0.2677\ \text{m} - 0.09652\ \text{m}\right) = 0.17118\ \text{m}$, $k = 16\ \text{W m}^{-1}\text{K}^{-1}$, $h_{CF} = 946.2\ \text{W m}^{-2}\text{K}^{-1}$, $t_{Fin} = 6.35 \bullet 10^{-4}\ \text{m}$ and $r_{Curve} = 3.56 \bullet 10^{-4}\ \text{m}$. From Equation B.2, $m = 0.03169$, $mL_{Fin} = 0.005425$ and $\eta_F = 0.9999$. Thus, from Equation B.1, $\eta_T \approx 1$.

Similarly, for the sample point considered in the heat and mass transfer model in Chapter 3, $L_{Fin} = L_{Segment} = 5.97 \bullet 10^{-3}\ \text{m}$, $k = 17.02\ \text{W m}^{-1}\text{K}^{-1}$, $h_{CF} = 899\ \text{W m}^{-2}\text{K}^{-1}$, $t_{Fin} = 5.0 \bullet 10^{-4}\ \text{m}$ and $r_{Curve} = 3.50 \bullet 10^{-4}\ \text{m}$. From Equation B.2, $m = 0.005604$, $mL_{Fin} = 3.3 \bullet 10^{-5}$ and $\eta_F = 0.9999$. Thus, from Equation B.1, $\eta_T \approx 1$.

Because the total fin array efficiencies approach unity, all of the wetted area in the coupling fluid microchannels can be approximated as prime area; these calculations show that conduction through the shim material does not inhibit the thermal pathway. The large shim thermal conductivity and the geometric dimensions of the fin contribute to this efficiency.

REFERENCES

Adcock, P. W. (1995). *From Fire to Ice.* Society of Women's Engineers National Meeting. Boston, MA.

Arh, S. and B. Gaspersic (1989), "Development and Comparison of Different Advanced Absorption Cycles," *International Journal of Refrigeration* Vol. 13(1) pp. 41-50.

Arima, H., M. Monde and Y. Mitsutake (2003), "Heat Transfer in Pool Boiling of Ammonia/Water Mixture," *International Journal of Heat Transfer* Vol. 39 pp. 535-543.

Burgett, L. W., M. D. Byars and K. Schultz (1999). *Absorption Systems: The Future, More Than a Niche?* International Sorption Heat Pump Conference. Munich, Germany pp. 13-24.

Calus, W. and P. Rice (1972), "Pool Boiling - Binary Liquid Mixtures," *Chemical Engineering Science* Vol. 27 pp. 1687-1697.

Chapman, S. and T. Cowling (1970). *The Mathematical Theory of Non-Uniform Gases: An Account of the Kinetic Theory of Viscosity, Thermal Conduction and Diffusion in Gases,* Cambridge University Press.

Chun, K. R. and R. A. Seban (1971), "Heat Transfer to Evaporating Liquid Films," *Journal of Heat Transfer* Vol. 93 pp. 391-396.

Colburn, A. P. and T. B. Drew (1937), "Condensation of Mixed Vapors," *American Institute of Chemical Engineers -- Transactions* Vol. 33 pp. 197-212.

Cooper, M. (1984), "Saturation Nucleate Pool Boiling - a Simple Correlation," *IChemE Symposium Series* Vol. 86 pp. 786 - 793.

Cullen, W. (1756), "Of the Cold Produced by Evaporating Fluids and of Some Other Means of Producing Cold," *Essays and Observations Physical and Literary Read before a Society in Edinburg and Published by Them, II.* .

Determan, M. and S. Garimella (2011), "Ammonia-Water Desorption Heat and Mass Transfer in Microchannel Devices," *International Journal of Refrigeration* Vol. 34 pp. 1197-1208.

Fernandez-Seara, J., J. Sieres and Vazquez (2002), "Simultaneous Heat and Mass Transfer of a Packed Distillation Column for Ammonia-Water Absorption Refrigeration Systems," *International Journal of Thermal Sciences* Vol. 41 pp. 927-935.

Fernandez-Seara, J., J. Sieres and Vazquez (2006), "The Importance of the Ammonia Purification Process in Ammonia-Water Absorption Systems," *Energy Conservation and Management* Vol. 47 pp. 1975-1987.

Fernandez-Seara, J., F. Uhia and J. Sieres (2007), "Analysis of an Air Cooled Ammonia-Water Vertical Tubular Absorber," *International Journal of Thermal Sciences* Vol. 46 pp. 93-103.

Garimella, S. (2004), "Method and Means for Miniaturization of Binary-Fluid Heat and Mass Exchangers " United States 7,066,241,

Garimella, S., R. Christensen and D. Lacy (1996), "Performance Evaluation of a Generator – Absorber Heat Exchange Heat Pump," *Applied Thermal Engineering* Vol. 16(7) pp. 591-604.

Garimella, S., D. Lacy and R. Stout (1997), "Space-Conditioning Using Triple-Effect Absorption Heat Pumps," *Applied Thermal Engineering,* Vol. 17(12) pp. 1183-1197.

Gorenflo, D. (1997). VDI-Waermeatlas, VDI - Verlag. Duesseldorf,.

Granryd, E. and P. Palm (2005). *Refrigerating Engineering*, Stockholm Royal Institute of Technology.

Grossman, G. and A. Zaltash (2001), "Absim – Modular Simulation of Advanced Absorption Systems," *International Journal of Refrigeration* Vol. 24 pp. 531-543.

Hempstead, C. and W. Worthington (2004). *Absorption Refrigeration* Encyclopedia of 20th Century Technology, Volume 2. New York, NY, Routledge.

Hewitt, Shires and Bott (1993). *Process Heat Transfer*, CRC Press.

Idogawa, K., K. Ikeda, T. Fukuda and S. Morooka (1987), "Effect of Gas and Liquid Properties on the Behavior of Bubbles in a Column under High Pressure," *Int. Chem. Eng.* Vol. 27 pp. 93-99.

Inoue, T., M. Monde, Y. Teruya and H. Ikeda (2002), "Pool Boiling Heat Transfer in Binary Mixtures of Ammonia/Water: Effects of Heat of Dilution and Dissolution on Heat Transfer Coefficient," *Heat Transfer – Asian Research* Vol. 31(4) pp. 272-283.

Kakac, S., R. K. Shah and W. Aung (1987). *Handbook of Single-Phase Convective Heat Transfer*. New York., Wiley.

Kendoush (2007), "Heat, Mass, and Momentum Transfer to a Rising Ellipsoidal Bubble," *Ind. Eng. Chem. Res.* Vol. 46(26) pp. 9232–9237.

Khir, T., A. Ben Brahim and R. K. Jassim (2005), "Boiling by Forced Convection of Water-Ammonia Mixtures in a Vertical Tube," *Canadian Journal of Chemical Engineering* Vol. 83(3) pp. 466–476.

Klein, S. A. (2009). *Engineering Equation Solver*, F-Chart Software.

Meacham, J. M. and S. Garimella (2004), "Ammonia-Water Absorption Heat and Mass Transfer in Microchannel Absorbers with Visual Confirmation," *ASHRAE Trans* Vol. 110(1) pp. 525–532.

Mendes, L., M. Collares and F. Ziegler (2007), "A Rich Solution Spray as a Refining Method in a Small Capacity, Single Effect, Solar Assisted Absorption Machine with the Pair Nh3/H2o: Experimental Results," *Energy Conversion and Management* Vol. 48 pp. 2996-3000.

Mostinski, I. L. (1963), "Application of the Rule of Corresponding States for Calculation of Heat Transfer and Critical Heat Flux," *Teploenergetika* Vol. 4 p. 66.

Nagavarapu, A. and S. Garimella (2011), "Design of Microscale Heat and Mass Exchangers for Absorption Space Conditioning Applications," *Journal of Thermal Science and Engineering Applications* Vol. 3(2) pp. 1 - 9.

Nahra, Z. and E. Naess (2009), "Heat Transfer in Pool Boiling of Binary and Ternary Non-Azeotropic Mixtures," *Heat Mass Transfer* Vol. 45 pp. 951–958.

Nishikawa and Y. Fujita (1977), "On the Pressure Factor in Nucleate Boiling Heat Transfer," *Memories of the faculty of Engineering Kyushu Univ.* Vol. 36(4).

Rattner, A. S. and S. Garimella (2011), "Energy Harvesting, Reuse and Upgrade to Reduce Primary Energy Usage in the USA," *Energy* Vol. 36(10) pp. 6172–6183.

Rohsenow, W., J. Hartnett and Y. Cho (1998). *Handbook of Heat Transfer* 3Ed., McGraw-Hill Professional.

Schlichting, H. (1955). *Boundary Layer Theory*. New York, McGraw-Hill.

Schlunder, E. (1983), "Heat Transfer in Nucleate Boiling of Mixtures," *Int Chem Eng* Vol. 23(4) pp. 589–599.

Shachtman, T. (1999). *Absolute Zero and the Conquest of Cold*. New York, New York, Houghton Mifflin Company.

Sieres, J. and J. Fernandez-Seara (2006), "Evaluation of the Column Components Size on the Vapor Enrichment and System Performance in Small Power Nh3-H2o Absorption Refrigeration Machines," *International Journal of Refrigeration* Vol. 29 pp. 579-588.

Sparrow, E. M. and A. Haji-Sheikh (1965), "Laminar Heat Transfer and Pressure Drop in Isosceles Triangular, Right Triangular, and Circular Sector Ducts," *ASME J. Heat Transfer* Vol. 87 pp. 426 - 427.

Spindler, K. (2010), "Overview and Discussion on Pool Boiling Heat Transfer and Correlations of Ammonia," *International Journal of Refrigeration* Vol. 33 pp. 1292-1306.

Stephan, K. (1982), "Absorption Heat Pumps and Working Pair Developments in Europe until 1974," *Workshop on New Working Pairs for Absorption Processes*, Berlin, Germany

Stephan, K. and Abdelsalam (1980), "Heat-Transfer Correlations for Natural Convection Boiling," *International Journal of Heat and Mass Transfer*(23) pp. 73–87.

Stephan, K. and M. Korner (1969), "Calculation of Heat Transfer in Evaporating Binary Liquid Mixtures," *Chemie-ingr-tech* Vol. 41(7) pp. 409–417.

Stephan, K. and P. Preuber (1979), "Warmeubergang Und Maximale Warmestromdichte Beim Behaltersieden Binarer Und Ternarer Flussigkeitsgemische," *Chem.-Ing. Techn* Vol. 51(37) pp. 649-679.

Taboas, F., M. Valles, M. Bourouis and A. Coronas (2007), "Pool Boiling of Ammonia/Water and Its Pure Components: Comparison of Experimental Data in the Literature with the Predictions of Standard Correlations," *International Journal of Refrigeration* Vol. 30 pp. 778-788.

Taboas, F., M. Valles, M. Bourouis and A. Coronas (2010), "Flow Boiling Heat Transfer of Ammonia/Water Mixture in a Plate Heat Exchanger," *International Journal of Refrigeration* Vol. 33 pp. 695-705.

Thome, J. R. and S. Shakir (1987), "A New Correlation for Nucleate Boiling of Binary Mixtures," *AIChE Symposium Series* Vol. 83 pp. 46-51.

U.S. Energy Information Administration (2000). *Trends in Residential Air-Conditioning Usage from 1978 to 1997*.

U.S. Energy Information Administration (2001). *Residential Energy Consumption Survey*.

U.S. Energy Information Administration (2002). *Analysis of Efficiency Standards for Air Conditioners, Heat Pumps, and Other Products*.

U.S. Energy Information Administration (2005). *Residential Energy Consumption Survey*.

U.S. Energy Information Administration (2010). *Annual Energy Review: 2010*.

Winterton (2004), "A Simple Method for Determining Bubble Size within Vertical Columns," *Chemical Engineering and Processing* Vol. 33 pp. 1-5.

Zheng, X., M. C. Chyu and Z. H. Ayub (1995), "Evaporation Heat Transfer Performance of Nozzle E Sprayed Ammonia on a Horizontal Tube," *ASHRAE Transactions* pp. 136-149.

Ziegler, F., R. Kahn, F. Summerer and G. Alefeld (1993), "Multi-Effect Absorption Chillers," *International Journal of Refrigeration* Vol. 16(5) pp. 301-311.